THE STUDY ON HIGH PERFORMANCE INORGANIC-ORGANIC HYBRID PEROVSKITE SOLAR CELLS

TANG GUANQI

PhD

The Hong Kong Polytechnic University

2020

The Hong Kong Polytechnic University

Department of Applied Physics

The Study on High Performance Inorganic-organic Hybrid Perovskite Solar Cells

TANG Guanqi

A thesis submitted in partial fulfillment of the requirements for

the degree of Doctor of Philosophy

August 2019

CERTIFICATE OF ORIGINALITY

I hereby declare that this thesis is my own work and that, to the best of my knowledge and belief, it reproduces no material previously published or written, nor material that has been accepted for the award of any other degree or diploma, except where due acknowledgement has been made in the text.

____   _____ (Signed)

_____ TANG Guanqi _____ (Name of student)

Abstract

Photovoltaic devices (solar cells), as a promising renewable alternative to fossil fuels, can directly convert solar energy into electricity, meet the increasing demand of global energy consumption and then alleviate the environmental pollution. Perovskite solar cells (PSCs), as a star among the photovoltaic family, have attracted tremendous attentions from both academic and industrial fields. The highest certified efficiency so far is boosted to 25.2%, which surpasses the top efficiency of commercial CdTe and CIGS devices. This excellent performance is mainly due to the intriguing optoelectronic properties of perovskite materials, such as high light absorption coefficient, desirable bandgap, long charge diffusion length and high defect tolerance. Thus, the crystal quality of perovskite films is the key issue for the photovoltaic performance of PSCs. Nowadays, the main fabrication method of perovskite thin films is solution-processing (spin-coating) method due to its easy-operation and low cost which enables high potential for commercialization. While the defects in the solution-processed perovskite films prevent the efficiency from reaching the limit value.

In this thesis, two works focus on improving the crystallinity of perovskite films by controlling the crystallization process. The employment of lead acetate ($PbAc_2$) as an additive in the perovskite precursor to retard the crystallization process of perovskite films, which could lead to the enlargement of grain size and low defect density. In another work, the MoS_2 flakes are introduced as an epitaxial growth template to control the crystal orientation of perovskite film. The obtained highly oriented perovskite films demonstrate low defect density and efficient charge transport. At last, van der Waals interaction is introduced into the grain boundaries of $MAPbI_3$ perovskite by adding 2D PEA_2PbI_4 to enhance the bendability. The 2D/3D perovskite

films demonstrate robust mechanical property and high bending durability since the strain is released by the van der Waals interaction.

Retarding the crystallization process of perovskite film is a useful strategy to enlarge the grain size and decrease the grain boundaries, which would lead to the reduction of defect density. We find that $PbAc_2$ can act as a crosslinking agent to make the perovskite intermediate phase more stable by forming strong hydrogen bonding. This stable intermediate phase significantly retards the crystallization process of perovskite films. The SEM characterization illustrates that the grain size is enlarged from 250 nm to 500 nm in average by introducing 3% $PbAc_2$ (molar ratio with respect to PbI_2). The defect density of 3% $PbAc_2$ modified perovskite film is lower than the control one by nearly one order of magnitude. Due to the enhanced quality of perovskite films, the efficiency of PSC is increased from 17.25% to 19.07% and the devices stability is improved significantly.

Besides, perovskite films with preferential orientation is highly critical to the high-performance PSCs due to the lower defect density and ideally efficient charge transport crossing the films. However, controlling the crystal orientation is challenging for the solution processing method. Epitaxial growth is a prevalent technology to prepare highly oriented semiconductors, especially two-dimensional materials. Thus, MoS_2 is selected as epitaxial growth template for $MAPbI_3$ due to the suitable lattice structure and energy band level. Under transmission electron microscopy (TEM), in-plane coupling between the perovskite and the MoS_2 crystal lattices is observed, leading to perovskite films with large grain size, lower trap density and preferential growth orientation along (110) normal to the MoS_2 surface. Based on the highly orientated perovskite films, the power conversion efficiency (PCE) of PSCs is boosted from 18.12% to 20.55%.

At last, the mechanical property of perovskite films is important for the bendability of FPSCs. It is prevalent that the cracks usually appear along the grain boundaries in the perovskite films to release the strains during bending operation, which leads to the severe degradation of the photovoltaic performance. 2D perovskites with different layers are combined by the van der Waals interaction. Due to the absence of dangling bonds among different layers, the external stress could be release by the slippage between neighboring layers, which enables 2D perovskite materials superior flexibility and deformability. Thus, 2D perovskite can be introduced into the grain boundaries of $MAPbI_3$ layer to release the strains which are normally relaxed by the formation of cracks along the grain boundaries. In our work, 2D PEA_2PbI_4 is introduced into $MAPbI_3$ films. The TEM characterization confirms that the 2D perovskites mainly distributed at the grain boundaries of $MAPbI_3$ films. The flexible perovskite solar cells (FPSCs) based on $MAPbI_3$ demonstrate PCE of 15.12%. The PCE of FPSCs based on 2D/3D perovskite is boosted to 19.27%. Due to the enhanced mechanical property of perovskite films, the FPSCs based on 2D/3D hybrid perovskite could maintain 94 % of initial PCE after 1000 bending cycles at curvature radius of 3.0 mm. In contrast, the FPSCs base on 3D perovskite retain only 70 % of original PCE. Thus, it is promising and feasible by introducing 2D perovskite at the grain boundaries to enhance the mechanical property of perovskite films.

In summary, $PbAc_2$ is employed as an additive to retard the crystallization process of perovskite films to enlarge the grain size and enhance the crystallinity. MoS_2 flakes are used as an epitaxial growth template to prepare the perovskite film with highly preferential orientation. These two strategies are successfully used to enhance the photovoltaic performance of PSCs. 2D PEA_2PbI_4 perovskite is introduced into the grain boundaries of $MAPbI_3$ film to improve the bendability by releasing the strain via van der Waals interaction. The mechanical property of perovskite films and devices

are substantially enhanced. These three works pave a way for preparing high performance PSCs based on glass and flexible substrates.

List of Publications

(1)   **Tang, G.**; You, P.; Tai, Q.; Wu, W.; Yan, F. Performance enhancement of perovskite solar cells induced by lead acetate as an additive. *Sol. RRL* **2018**, *2*, 1800066.

(2)   **Tang, G.**; You, P.; Tai, Q.; Yang, A.; Cao, J; Zheng, F.; Zhou, Z.; Zhao, J.; Chan, P.; Yan, F. Solution-phase epitaxial growth of perovskite films on 2D material flakes for high-performance solar cells. *Adv. Mater.* **2019**, *31*, 1807689.

(3)   **Tang, G.**; Yan, F. Intrinsically flexible hybrid perovskites for high-performance solar cells by introducing van der Waals interaction at grain boundaries. In perparation.

(4)   Liu, Z.; You, P.; Xie, C.; **Tang, G.**; Yan, F. Ultrathin and flexible perovskite solar cells with graphene transparent electrodes. *Nano Energy* **2016**, *28*, 151-157.

(5)   Tai, Q.; Guo, X.; **Tang, G.**; You, P.;Ng, T.; Shen, D.; Cao, J., Liu, C.; Wang, N.; Zhu, Y.; Lee, C.; Yan, F. Antioxidant grain passivation for air-stable tin-based perovskite solar cells. *Angew. Chem. Int. Ed.* **2019**, *58*, 806-810.

(6)   You, P.; **Tang, G.**; Yan, F. Two-dimensional materails in perovskite solar cells. *Mater. Today Energy* **2019**, *11*, 128-158.

(7)   Liu, C.; Tai, Q.; Wang, N.; **Tang, G.**; Loi, H.; Yan, F. Sn-based perovskite for highly sensitive photodetectors. *Adv. Science.* **2019**, 1900751.

(8)   Zhou, X.; Li, Y.; **Tang, G.**; Yan, F. Schottky barrier-controlled black phosphorous/perovskite phototransistors with ultrahigh sensitivity and fast response. Small. **2019**, *15*, 1901004.

Acknowledgements

This thesis describes the works I carried out as a PhD student in Department of Applied Physics of the Hong Kong Polytechnic University, Prof. YAN Feng's group. The successful completion of these works highly depends on the help from many people, such as my supervisor, group members, family members and so on. Here, I will express my grateful gratitude and best wishes to them.

First, I will give my great thanks to my supervisor, Prof. YAN Feng. In 2016, Prof. YAN gave me the offer which allows me to conduct Ph.D study in PolyU. In the three years of study and research, Prof. YAN always gives me the most effective guidance and encouragement when I am in confusion and feel disappointed. Prof. YAN teaches me how to design experiments and analyze results logically and effectively. He always has enough patience to teach me how to express your findings and how to write a professional academic paper. Prof. YAN's rich knowledge and sharp mind deeply shock me. He is really a good supervisor. I express my grateful respect and best wishes to my supervisor, Prof. YAN Feng.

The completion of my Ph.D study also depends on the supports from my colleagues in the department. I would like to thank Dr. Liu Zhike, Dr. Tai Qidong, Dr. Liu Shenghua, Dr. You Peng, Dr. Fu Ying, Dr. Zou Xuming, Dr. Wu Runsheng, Dr. Xie Chao, Dr. Wang Naixiang, Dr. Lin Haifeng, Dr. Yu Ji, Dr. Fan Xi and Dr. Wang Meng. They have given me value suggestions and guidance during me study period. I also want to thank my colleagues: Dr. Lin Peng, Dr. Li Jinhua, Dr. Sun Zhenhua, Mr. Yang Anneng, Mr. Cao Jiupeng, Mr. Song Jiajun, Mr. Tang Kai-Chi, Mr. Liu chunki, Mr. Loi Hok-Leung, Mrs. Wang Tianyue, Mrs. Li Sihua, and Mrs. Yin Guannan. I also thank my classmates: Mr. Zeng Longhui, Mrs. Wang Yunfeng and

Mrs. Wang Ting. And I also give me great thanks to all my friends, who always encourage me and accompany me during my study period.

In the last, I want to deeply thank my father, my mother and my brother. They always accompany and encourage me. I also thank my girlfriend. She always understands me and supports me. Based on their support and understanding, I can focus on my Ph.D study and complete the research works. Thanks a lot.

.

Table of Contents

List of Figures

Chapter 1   Introduction

1.1   Background

In the long history of human beings, the electricity plays a vital role in accelerating the development of human society. Generally, the main sources of electricity generation are from the combustion of fossil fuels, such as coal, oil and gas. Due to the global economic growth and industrial demand, a large amount of fossil fuels are used to meet the global need for electricity. This leads to serious environmental issues, such as global warming crisis, acid rains, Nino phenomenon and air pollution. In addition, the fossil fuels are non-renewable sources. Energy crisis is inevitable if the electricity generation is based on fossil fuels. Thus, renewable and clean sources for electricity generation are necessary and urgent for the sustainable development of human society. Nowadays, many renewable sources, such as wind energy, tide energy, and solar energy are employed as clean energy to generate electricity. The solar energy is prior to other renewable sources due to the easy conversion to electricity. Photovoltaic technology could directly convert sun light into electricity, which is a promising strategy to solve the energy crisis in the future.

Since the first discovery of the photovoltaic effect by French scientist Edmund Becquerel in 1839, various photovoltaic materials and solar cell configurations are invented to increase the power conversion efficiency (PCE). The developments of record efficiencies for different solar cells are listed in **Figure 1.1**, which is recorded by the national renewable energy laboratory (NERL) in USA. It can be observed that the highest efficiency of single junction cells can reach 29.1% by GaAs solar cells. For the silicon solar cells, the efficiency of 26.1% is obtained based on single silicon

crystal and 22.3% for multi-crystalline silicon. CIGS solar cells could reach 23.4% as the thin-film technology. Although the high efficiencies can be achieved for the single-junction GaAs, crystalline silicon solar cells and thin-films technologies, the high fabrication cost hinders the wide practical applications. The high cost is a main factor limiting the large-scale utilization of commercial silicon solar cells. Therefore, new photovoltaic technologies are investigated to fabricate solar cells with high efficiency and low cost. As shown in **Figure 1.1**, the emerging PV technologies, such as dye-sensitized cells, perovskite cells and organic cells, have fast efficiency development in last decade. Among them, perovskite solar cell is a star due to the high efficiency of 24.2% and easy fabrication.

In 2009, Miyasaka *et al.* first introduced perovskite materials into solar cells and prepared solar cells with efficiency of 3.8%. From then on, the efficiency is improved to 25.2% in one decade, which suggests the excellent optoelectronic properties of perovskite as light absorber. Besides, the efforts in morphology control, devices configuration and physics study also have major contribution to the development. Due to the deeper understanding of physical mechanisms in perovskites, further improvement of efficiency to theoretical limit of 30% can be expected in the future. However, there are some issues hindering the commercialization. Lead compounds in perovskites are very toxic and harmful to the environment. The large-scale use of perovskite solar cells would lead to the harm for human health. Moreover, perovskite materials would degrade quickly in humid air and light illumination. Efforts are needed to prepare high-quality perovskite films which could pass the stability test, such as long-term light soaking tests (1000 h in full sunlight) and heat tests (1000 h at 85% humidity and 85°C). The solution of these issues could accelerate the commercialization of perovskite solar cells.
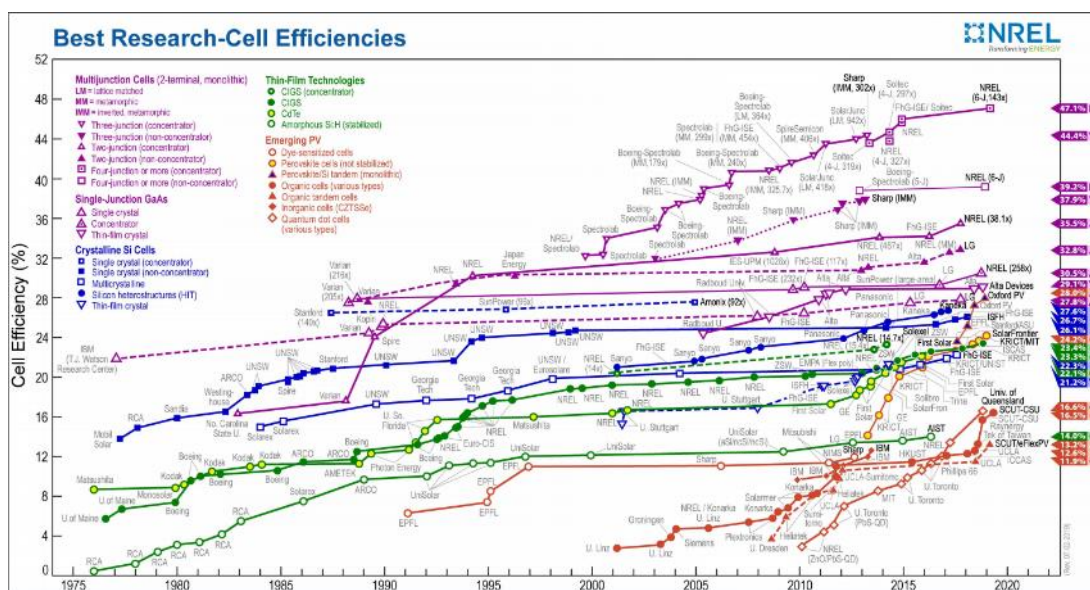
Figure 1.1. The best research-cell efficiencies.

1.2   Objectives of Research

Currently, the presence of defects in perovskite films is the main factor limiting the further improvement on the photovoltaic performances. Reducing the defects in perovskite films is challenging for the solution processing fabrication method. Thus, it is urgent to find novel and efficient ways to enhance the crystallinity and decrease the defects of perovskite films. In addition, flexible perovskite solar cells (FPSCs) are supposed to be the foremost commercialization option due to the facile mass-production by the roll to roll printing process, which can further decrease the cost substantially. The bending stability of perovskite films is critical for the practical application. Nowadays, there are rare investigations to explore strategies to enhance the bendability of polycrystalline perovskite films. Thus, we have demonstrated two strategies to enhance the crystallinity and decrease the defects of perovskite film and one strategy to enhance the bendability of perovskite films.

In the first strategy, we have introduced $PbAc_2$ into the perovskite precursor to retard

the crystallization process of perovskite films. We find that $PbAc_2$ can act as a crosslinking agent to make perovskite intermediate phase more stable by forming strong hydrogen bonding. The stable intermediate phase can retard the crystallization process and lead to better morphology and larger grains of perovskite films. Moreover, the $PbAc_2$ additive can generate PbI_2 in the perovskite films, which will passivate defects at grain boundaries. Consequently, the carrier lifetimes in the PSCs are prolonged significantly and the densities of trap states are reduced by one order of magnitude due to the addition of $PbAc_2$ for only 3 % (molar ratio with respect to PbI_2). We find that the device efficiency is relatively improved for about 10% and the device stability is greatly enhanced as well.

In the second strategy, we employed MoS_2 flakes as the growth template for perovskite films with preferred orientation and high crystallinity. We find for the first time the vdW epitaxial growth of $MAPbI_3$ perovskite on MoS_2 flakes, leading to highly oriented perovskite films with large grain sizes and low defect densities. TEM images demonstrate that (008) plane of $MAPbI_3$ and (110) plane of MoS_2 can match perfectly, which facilities the out-of-plane growth of perovskite films with preferential orientation along (110). Then MoS_2 flakes are modified on hole transport layers in inverted PSCs to improve the quality of the perovskite active layers. The power conversion efficiency (PCE) is boosted from 18.12% to 20.55% due to the significant increases of fill factor (FF), short current density (J_{sc}), and open circuit voltage (V_{oc}). This work provides a novel approach for preparing epitaxial perovskite films based on 2D material templates.

Finally, 2D perovskite PEA_2PbI_4 is introduced into grain boundaries of $MAPbI_3$ perovskite to inherently improve the bendability of perovskite films. The stress applied on the films could be successfully released by the more bendable and deformable 2D perovskite. Due to the enhanced mechanical property of perovskite

films, the FPSCs based on 2D perovskite modified MAPbI$_3$ could maintain 94 % of initial PCE after 1000 bending cycles at curvature radius of 3.0 mm. In contrast, the FPSCs base on MAPbI$_3$ retain only 69 % of original PCE.

1.3   Outline of Thesis

The organization of this thesis is shown as follows:

Chapter 1: Introduction. In this part, the history of photovoltaic technology, the emergence and evolution of perovskite solar cells are introduced. Then, the objectives of research and outline of this thesis are presented.

Chapter 2: Literature review. In this part, a brief introduction of the history of perovskite solar cells is first presented to show the current research status. Then, the fundamental properties, such as crystal structure and optoelectronic properties, are summarized and the corresponding reasons are also demonstrated to understand superior properties as the excellent optoelectronic materials. Third, the reported fabrication approaches of perovskite single crystals and thin films are illustrated. Fourth, four kinds of device configurations and corresponding working mechanisms are reviewed. Fifth, PCE developments of perovskite solar cell based on rigid and flexible substrates are summarized respectively. Finally, the current challenges, such as long-term stability, current-voltage hysteresis and toxicity of raw materials, are discussed and the perspectives for the further development are presented.

Chapter 3: Performance enhancement of perovskite solar cells induced by lead acetate as an additive. In this chapter, we demonstrate the fabrication of high-efficiency PSCs by employing lead acetate (PbAc$_2$) as an additive in the perovskite precursor for the first time. By adding a few percent of PbAc$_2$ (molar ratio

with respect to PbI_2) into the precursors, the perovskite crystallization process is significantly retarded, leading to pinhole-free perovskite films with large grains and low defect densities. As result, the power conversion efficiencies and stability of the PSCs are substantially improved. This work provides a convenient and unique approach for preparing high-quality perovskite films that can be used in photovoltaics as well as other optoelectronic devices.

Chapter 4: Solution-phase epitaxial growth of perovskite films on 2D material flakes for high-performance solar cells. In this part, we report solution-phase van der Waals epitaxy growth of $MAPbI_3$ perovskite films on MoS_2 flakes for the first time. Under transmission electron microscopy, in-plane coupling between perovskite and MoS_2 crystal lattices is observed, leading to perovskite films with larger grain size, lower trap density and preferential growth orientation along (110) normal to the MoS_2 surface. In perovskite solar cells, when perovskite active layers are grown on MoS_2 flakes coated on hole transport layers, the power conversion efficiency is substantially enhanced for 15 % relatively due to the increased crystallinity of the perovskite layer and the improved hole extraction and transfer rate at the interface. This work paves a way for preparing high-performance perovskite solar cells and other optoelectronic devices by introducing two-dimensional materials as interfacial layers.

Chapter 5: Intrinsically flexible hybrid perovskites for high-performance solar cells by introducing van der Waals interaction at grain boundaries. Flexible perovskite solar cells (FPSCs) are highly desirable due to the facile mass-production and diverse wearable applications. As the light absorber, the bending stability of perovskite films under operation is critical for the photovoltaic performance. However, the polycrystalline perovskite films have a mass of defects at the grain boundaries, which serve as stress concentrators that promote propagation of cracks under bending operation, leading to degradation. In this part, we report that van der Waals

interactions are introduced into the grain boundaries of MAPbI$_3$ films to release strains by incorporating 2D perovskite (PEA$_2$PbI$_4$). The applied strain under operation could be released by the recoverable sliding or rotating between interlayers of 2D perovskite. The intrinsic bendability and deformability of perovskite films are significantly improved. Besides, due to the defect passivation, the efficiencies of perovskite solar cells based on flexible and glass substrates are boosted to 19.55% and 20.97%, respectively. This work provides a new research direction to fabricate flexible perovskite solar cells with high bendability and efficiency.

Chapter 6. Conclusions and perspectives. In this chapter, the summary of works in this thesis is presented and future challenges and opportunities are proposed.

Chapter 2   Literature Review

2.1   Introduction

Solar cells, as one of promising renewable alternatives to fossil fuels, can alleviate the shortage of energy sources and the environmental pollution. A recent forecast states that the photovoltaics will contribute about a third of new electricity generation worldwide capacity between now and 2030 [1]. Silicon solar cells, as the mainstream photovoltaic technology, dominate the photovoltaic market due to the high-power conversion efficiency (PCE) and operation stability. However, the high fabrication cost hinders the further large-scale use of silicon solar cells. The photovoltaic technology with high PCE and low processing cost is highly desirable in the current photovoltaic market. Perovskite solar cells (PSCs), as a star among the photovoltaic family, have attracted tremendous attentions from both academic and industrial fields due to the high efficiency and low cost. The highest certified efficiency so far is boosted to 25.2%, which surpasses the top efficiency of commercial cadmium telluride (CdTe, 22.1%) and copper indium gallium selenide (CIGS, 22.6%) devices, and is very close to that of monocrystalline silicon solar cells (22.3%) [2]. The low cost of raw materials and fabrication process enable the PSCs high potential for large-scale production and commercialization. In addition, the solution process allows the perovskite to be deposited on flexible substrates, which can fulfill the highly diverse applications, such as wearable and portable electronics, unmanned systems, smart buildings and aerospace applications [3-5]. Thus, it is necessary to review the development of perovskite solar cells to guide the direction to further improve the photovoltaic performance.

In this chapter, we will first review the perovskite structure and its superior optoelectronic properties, such as high absorption efficiency, tunable bandgap, long carrier lifetime and diffusion length. The possible explanations are also included. Second, the fabrication approaches of perovskite films are summarized. The quality of perovskite films is sensitive to the fabrication process, which would determine the photovoltaic performance of the devices. The preferred fabrication process and morphology of perovskite films would be highlighted. Third, the PSCs with different device structures and corresponding working mechanisms are presented. Fourth, we will demonstrate the efficiency development of perovskite solar cells based on glass and flexible substrates. Fifth, we will show the current challenges for the commercialization of PSCs, such as long-term stability and toxicity of the raw materials (Pb), and the possible reasons and the solutions reported in the literatures. Last, we will summary this chapter and give the outlook on the further improvement of PSCs.

2.2   Fundamental properties of hybrid perovskite

2.2.1   Crystal structure

The organic-inorganic hybrid perovskites are materials described with the formula of ABX_3 (where A cation is MA or FA, MA= $CH_3NH_3^+$, FA=$CH_3(NH_2)_2^+$; B cation represents Pb^{2+} or Sn^{2+}; X anion refers to Cl^-, Br^- or I^-). The crystal structure is depicted in **Figure 1a**. To maintain the structural stability of perovskite, the corresponding geometric tolerance factor (t) should be close to 1 or between 0.813 and 1.107. The t is defined as $\frac{R_A+R_B}{\sqrt{2}(R_X+R_B)}$, where R_A, R_B, and R_X are the ionic radii of the corresponding ions [6]. For the lying in the range between 0.89 and 1.0, the structure of perovskite is prone to be cubic. The crystal with lower t values could tend to be less

symmetric tetragonal or orthorhombic structures [1, 7]. In the perovskite of $APbX_3$, A cation with radii between 1.60 and 2.50 could form the stable perovskite structure. The tolerance factors for the most used lead and tin based perovskite are shown in **Figure 1b**. In addition, the temperature is another factor to affect the crystal structure of perovskites [8]. Perovskites could demonstrate different crystal structure under different temperatures. For example, the $MAPbI_3$ perovskite has a revisable phase transition from cubic to tetragonal structure at 56 ℃. This phase transition could partially explain the thermal stability of perovskite and the related optoelectronic devices. For the $FAPbI_3$, the temperature for the phase transition is much higher, which enables higher thermal stability.
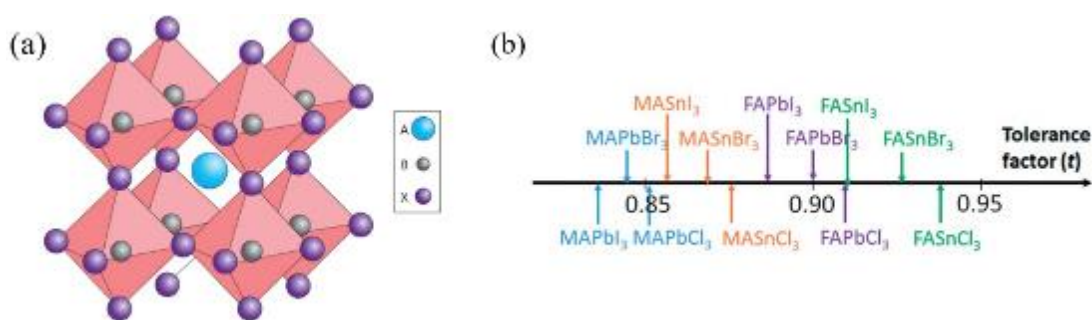
Figure 2.1 a) Perovskite crystal structure.[1] b) Tolerance factors of a series of halide perovskites.[9]

2.2.2 Optoelectronic properties of perovskite

As a light absorber, the perovskite materials have several excellent optoelectronic properties, such as high light absorption efficiency, tunable bandgap, long carrier lifetime and diffusion length. Park *et al.* estimated the absorption efficiency of $MAPbI_3$ by coating $MAPbI_3$ on the nanocrystalline TiO_2 film. The absorption coefficient was estimated to be 10^4 cm^{-1} at wavelength of 550 nm. [7] Therefore, the perovskite film with thickness of 400 nm is enough to absorb most of the light. The thin perovskite film could decease the defect density and materials cost. Yan *et al.*

contributed the high optical absorption of $MAPbI_3$ to the higher density of states derived from the Pb p orbital in the lower conduction by theoretical calculation. [10]

The theoretical calculation has revealed that the electronic structure of perovskite ($APbX_3$) is concerned with the p orbital of X anion and the p orbital of Pb.[11] Thus, the bandgap of perovskite can be tuned by changing the X component. Noh *et al.* first realized the bandgap tunability by varying the ratio of I and Br in the $MAPbX_3$.[12] The bandgap of $MAPb(I_{1-x}Br_x)_3$ could be tuned from 1.58 to 2.28 eV. The bandgap tunability of perovskite could enable the fabrication of colorful solar cells.

The length of carrier diffusion is important for the charge collection efficiency of solar cells. The long diffusion length could enable the generated holes and electrons to be collected by the electrodes efficiently. Moreover, that could allow thick perovskite films to absorb more light. Xing *et al.* obtained the electron-hole diffusion lengths of at least 100 nm for the solution-processed $MAPbI_3$ film by using femtosecond transient optical spectroscopy. [13] Snaith *et al.* found that the diffusion lengths are greater than 1 micrometer in $MAPbI_{3-x}Cl_x$, which is an order of magnitude larger than the absorption depth. [14] This result explains the success of high efficiency planar heterojunction perovskite solar cells. Huang *et al.* demonstrated that the diffusion length in the solution-grown $MAPbI_3$ single crystal could be large than 175 micrometers under 1 sun (100 mW cm^{-2}) due to the larger carrier mobility, longer lifetime and much lower trap density. [15]   These properties enable perovskite materials excellent optoelectronic semiconductor.

2.3 The fabrication approaches of perovskite crystal

Defect-free perovskite is highly desirable to study the fundamental properties and intrinsic characteristics. Thus, the synthesis of defect-free single crystal is very significant for materials physics for the perovskite. Dang *et al.* reported for the first time the growth of single crystals of tetragonal MAPbI$_3$ with dimensions of 10 mm × 10 mm × 8 mm by a temperature-lowing method in HI solution as shown in **Figure 2.2a**.[16] First, the methyl-ammonium iodide (CH$_3$NH$_3$I) and Pb (CH$_3$COOH)$_2$·3H$_2$O were dissolved in the aqueous HI. Then the temperature of solution was decreased from 65 to 40 ℃ to induce the saturation of the solute. The MAPbI$_3$ single crystals would be grown at the bottom of the flask. This process needs about several days. The bandgap of the single crystal is approximately 1.48 eV, which is smaller than that of polycrystalline thin film.

In order to grow the single crystal efficiently, seed-induced process is employed to shorten the growing time. Liu *et al.* prepared big single crystal with dimension of 71 mm × 54 mm × 39 mm.[17] The precursor was prepared by dissolving MAI and PbI$_2$ in gamma-butyrolactone (GBA). Then a seed crystal with diameter of 2 mm was placed in 20 mL of the prepared precursor which is kept at 100 ℃ for 48 h. The seed grew into bigger crystal with diameter of 7 mm. The process could be repeated to grow larger one as shown in **Figure 2.2b**. The authors found that the growth rate is proportional to the total surface area of the seed crystal. Thus, this seed-induced method could grow large single crystal in a short time. Shi et al. report a strategy using antisolvent vapor-assisted crystallization (AVC) as shown in **Figure 2.2c**. The antisolvent dichloromethane (DMC) would slowly diffuse into the perovskite precursor to induce the growth of single crystal.[18]
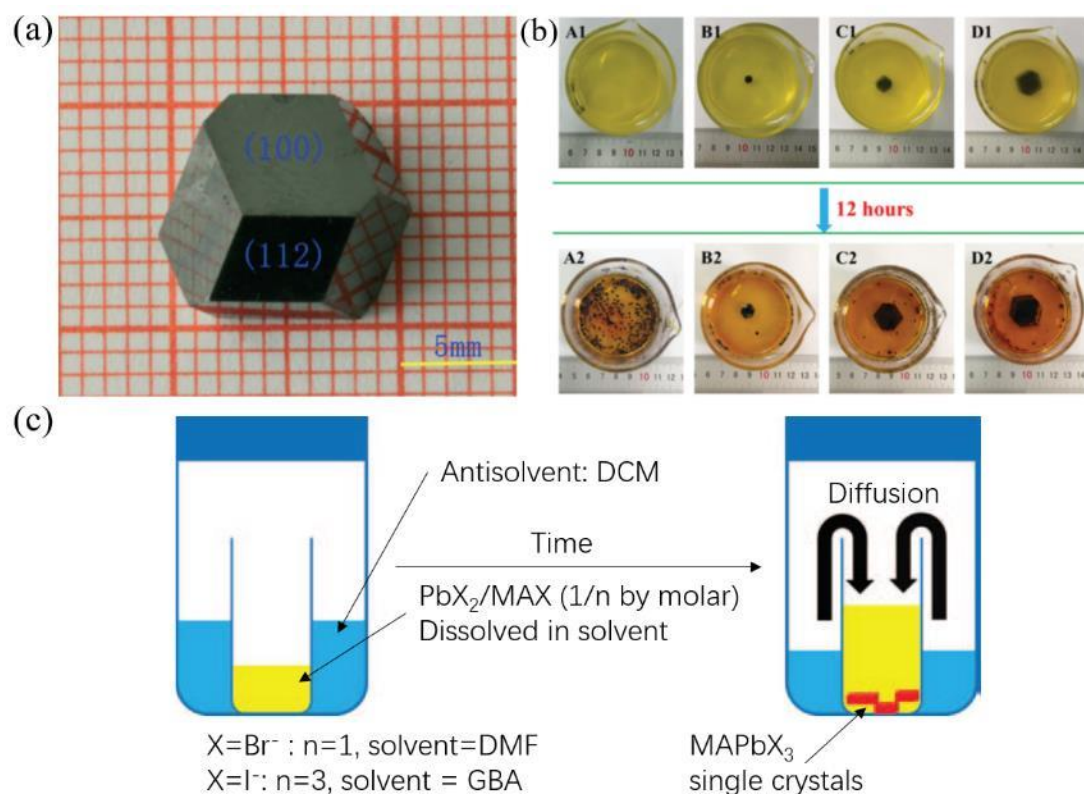
Figure 2.2. a) Image of $CH_3NH_3PbI_3$ oriented to exhibit its natural facets (100) and (112).[16] b) Photograph of the crystal growth for 12 h.[19] c) Schematic diagram of the crystallization process.[18]

In summary, the key point of growing perovskite single crystal by solution process is to oversaturate the precursor in order to precipitate the solute. After a certain of time, the solute would form into the single crystals.

2.4   Deposition of perovskite thin films

The quality of perovskite film is sensitive to the fabrication process. In general, pin-hole free perovskite films with large grain size are desirable for the high photovoltaic performance. Many strategies are invented to satisfy the requirements, such as solution process, vapor-base deposition, and vapor-assisted deposition methods.

2.4.1 Solution process methods

One-step solution process method. Solution process method is the most popular due to easy of processing and low fabrication cost. Generally, organic halides (methylammonium iodide (MAI)) and lead halides (PbX_2, X=I, Br, or Cl) are dissolved in gramma-butyrolactone (GBL), dimethylformamide (DMF), or dimethyl sulfoxide (DMSO) to prepare the precursor solution. The perovskite films are fabricated by spin-coating the precursor on the substrates followed by a thermal annealing. The fabrication process is shown in **Figure 2.3a**. The perovskite films fabricated by this method usually have pin-holes, low crystallinity and weak light absorption. That is because that the slow nucleation rate, which results from the high boiling point of solvent (such as DMF, 153 ℃), leads to the perovskite films with holes and low crystallinity.[20]

One-step antisolvent solution process method. In order to improve the quality of perovskite films, an anti-solvent is employed in the one-step solution process.[21] This simple approach involves the spin-coating of a DMF solution of $CH_3NH_3PbI_3$ (or other perovskite materials) on a substrate, followed immediately by exposure of the wet film to a second solvent, such as chlorobenzene, to induce crystallization as shown in **Figure 2.3b**. The role of the second solvent is to rapidly reduce the solubility of $CH_3NH_3PbI_3$ in the solvent (DMF) and thereby promoting fast nucleation and growth of the crystals in the film. The perovskite films can be fabricated with full-coverage, high crystallinity and uniformity. Due to the high reproducibility and efficiency, this method is the most popular in the labs.
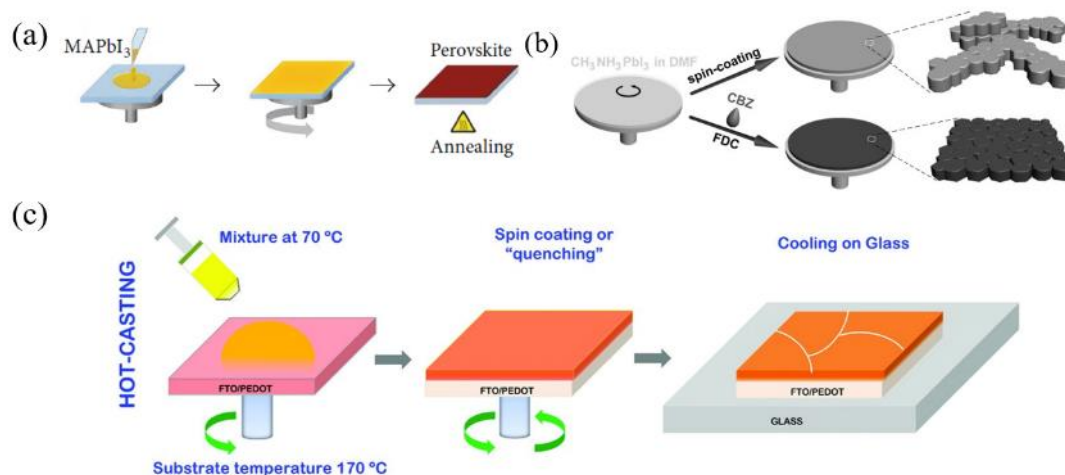
Figure 2.1. a) One step solution process. b) one-step antisolvent solution process.[20] c) Hot-casting scheme for large-area crystal growth.[22]

Hot-casting method. This approach involves casting a hot (about 70 °C) mixture of lead iodide (PbI$_2$) and methylamine hydrochloride (MACl) solution onto a substrate maintained at a temperature of up to 180 °C and subsequently spin-coated to obtain a uniform film with millimeter-scale crystalline grains.[22] The process is shown in **Figure 2.3c**. The growth of large grains is attributed to the presence of solvent when heating the substrate. This allows for the prolonged growth of the perovskite crystals, yielding large crystalline grains. The large grains lead to reduced bulk defects and improved charge carrier mobility, which significantly enhances the photovoltaic performance of the solar cells.

Two-step sequential dipping method This approach involves two steps in the deposition of perovskite films as shown in **Figure 2.4a**. First, PbI$_2$ is spin-coated on the substrate. Second, the PbI$_2$ substrate is transformed into the perovskite by dipping it to a solution of CH$_3$NH$_3$I. The dipping time and solution concentration are important for the ultimate photovoltaic performance of devices.[23]

Two-step interdiffusion method This approach involves two steps in the deposition of perovskite films as shown in **Figure 2.4b**. First, PbI$_2$ dissolved in DMF is

spin-coated on the substrate. Second, MAI dissolved in IPA is spin-coated on the PbI$_2$ substrate. The supersaturated hot solution of PbI$_2$ is used for quick drying to obtain a pin-hole free and conformal PbI$_2$ layer. Since PbI$_2$ has relatively low solubility in 2-propanol, the spin-coating of MAI could not wash off the PbI$_2$. The bilayer films are then annealed at a temperature of 100 °C for varied durations.[24]

2.4.2 Vapor-base deposition method

Dural-source vapor deposition method This approach involves two sources of vapor, organic source (such as MAI) and inorganic source (such as PbI$_2$) as shown in **Figure 2.4c**. This dual-source vapor deposition results in superior uniformity of the coated perovskite films over a range of length scales, which subsequently results in substantially improved solar cell performance.[25] This method has great potential for large-scale production.
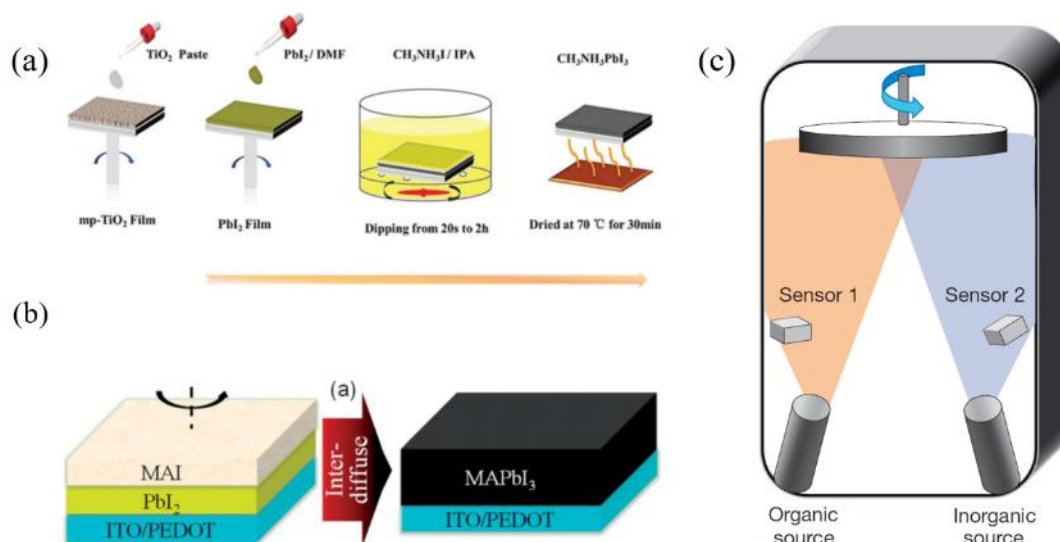
Figure 2.4. a) Two-step sequential deposition procedure.[26] b) Two-step interdiffusion process.[24]. c) Dural-source vapor deposition method.[25]

Soft-cover deposition method The precursor is achieved by mixing the amine complex, CH$_3$NH$_3$I$_3$·CH$_3$NH$_2$ and PbI$_2$·CH$_3$NH$_2$, in a molar ratio of 1:1. The mixed

amine complex precursors are loaded on the center of a substrate, and then a smooth and flat polyimide (PI) film is applied onto the precursors as shown in **Figure 2.5a**. Pressure is applied via a pneumatically driven squeezing board, which spread the liquid precursor under the PI film. The pressure is held for 60 s and then unloaded. The assembly is put on a hotplate at 50 °C for 2 min. After peeling off the PI film at a speed of 50 mm s^{-1}, a dense and uniform perovskite film is formed in air at room temperature when the film released CH_3NH_2 gas owing to the weak molecular interactions.[27]

2.4.3 Vapor-assisted deposition method

This approach involves two steps in the deposition of perovskite films as shown in **Figure 2.5b**. First, PbI_2 dissolved in DMF is spin-coated on the substrate. Second, PbI_2 substrate is annealed at 150 °C in MAI vapor in N_2 atmosphere for 2 h to form the perovskite films. This method takes advantage of the kinetic reactivity of MAI and thermodynamic stability of perovskite during the in-situ growth process and provides films with well-defined grain structure with grain sizes up to microscale, full surface coverage, and small surface roughness, suitable for PV applications.[28]
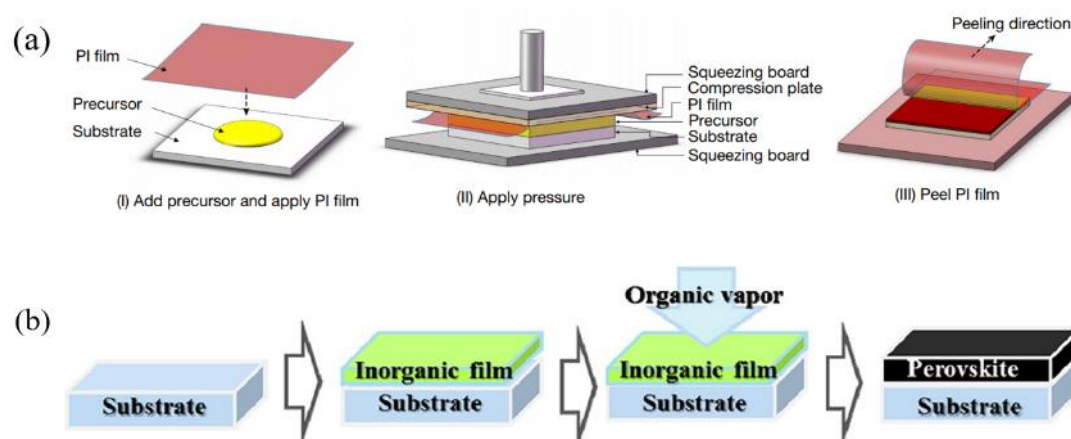
Figure 2.5. a) Schematic diagram of soft-cover deposition method.[27] b) Vapor-assisted deposition method.[28]

2.5   Working   mechanisms   and   device configurations of perovskite solar cells

In perovskite solar cells, the incident photons are absorbed by the perovskite layer to generate excitons which then separate into holes and electrons easily because of low binding energy. Holes and electrons are selectively extracted by corresponding transport layer and subsequently collected by the electrodes with the assistance of build-in electric field. The balanced and long hole-electron diffusion length property enables different device configuration.

By the several years of development, there are mainly four kinds of device configuration developed for perovskite solar cells as shown in **Figure 2.6**. Since the perovskite was first used as dye-sensitizer in dye sensitized solar cells (DSSCs) by Miyasaka, device with mesoscopic structure is first employed.[29] It is divided into formal (n-i-p) and inverted (p-i-n) structures based on the deposition sequence of hole and electron transporting layers. The mesoscopic structures are composed of substrate/transparent conductive oxide/compact layer/ mesoscopic electron transporting layer (ETL)/perovskite/ hole transporting layer (HTL)/ electrode for formal structure (n-i-p) and substrate/transparent conductive oxide/compact layer/ mesoscopic HTL/perovskite/ ETL/ electrode. Snaith *et al.* first fabricated perovskite solar cells with planar configuration.[25] Compared with mesoscopic structure, no mesoscopic layer is included. Triple mesoscopic PSCs are invented to enhance the long-term stability of PSCs by removing the organic HTL and metal electrodes.[30] The perovskite solar cells serve as top cells to fabricate tandem solar cells with other mature photovoltaic technologies, such as silicon solar cells, CIGS and low bandgap perovskite.[31-33] This combination not only enhances the PCE beyond the Shockley-Queisser limit of single junction solar cells but provides a path to

commercialization for PSCs.
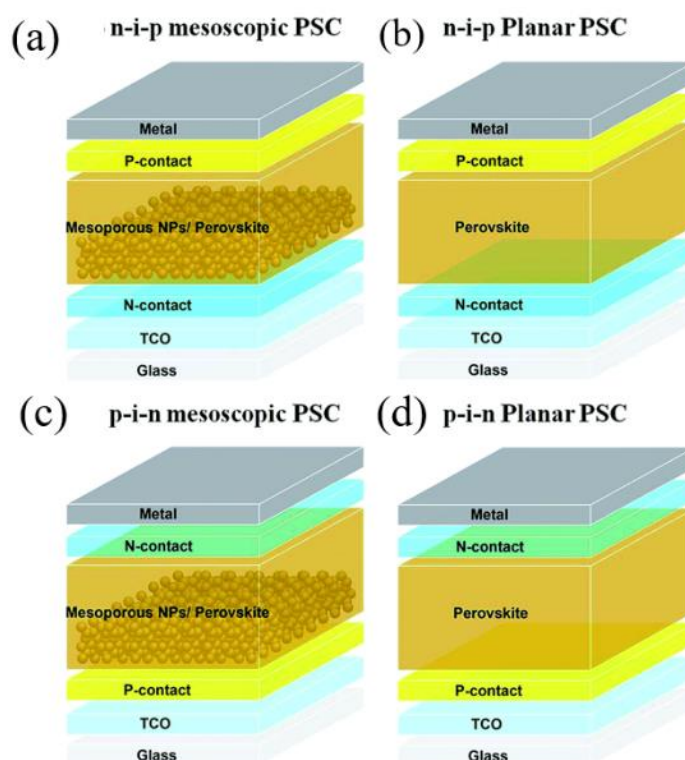
Figure 2.6. Different kinds of device configurations for perovskite solar cells.

2.6   The efficiency development of perovskite solar cells based on rigid and flexible substrates

2.6.1 The efficiency milestones for rigid perovskite solar cells

The efficiency of PSCs has been increased quickly due to the efforts from all researchers. The main PCE achievements are summarized in **Figure 2.7**. In 2009, Miyasaka *et al.* reported the employment of MAPbI$_3$ nanocrystalline particles self-organized on TiO$_2$ as n-type semiconductors in the dye-sensitized mesoscopic

solar cell.[29] The cell was constructed by using $CH_3NH_3PbI_3/TiO_2$ as the anode and a Pt-coated FTO glass as the cathode with insertion of a 50 μm thick separator film. Under the TiO_2 with thickness of 8 μm, the $MAPbI_3$ device could obtain the PCE of 3.81% with V_{oc} of 0.61 V, J_{sc} of 11.0 mA/cm^2 and FF of 0.57. This is the first report of perovskite based photovoltaic. The solar cells are unstable due to the liquid electrolyte. In order to solve the issue of the dissolution of perovskite in the electrolyte, in 2012, Park *et al.* employed solid-state spiro-MeOTAD as a hole transporting layer to prepare the solar cells with configuration of FTO/TiO_2/mesoscopic TiO_2/perovskite/ spiro-MeOTAD/Au.[34] The efficiency was boosted to 9.7% with V_{oc} of 0.89 V, J_{sc} of 17.6 mA/cm^2 and FF of 0.62. The long-term stability of devices was significantly enhanced due to the solid-state hole transporting layer. In the same year, Snaith et al. used mesoporous Al_2O_3 to replace the mesoporous TiO_2 as the electron transporting layer to enhance the PCE to 10.9%.[35] It was observed that electron transport through the perovskite layer was much faster than the TiO_2 layer. In 2013, Seok et al. reported that the efficiency of PSCs was boosted to 12.0% with V_{oc} of 0.997 V, J_{sc} of 16.5 mA/cm2 and FF of 72.7% by employing poly-triarylamine (PTAA) as the hole transporting layer.[36]
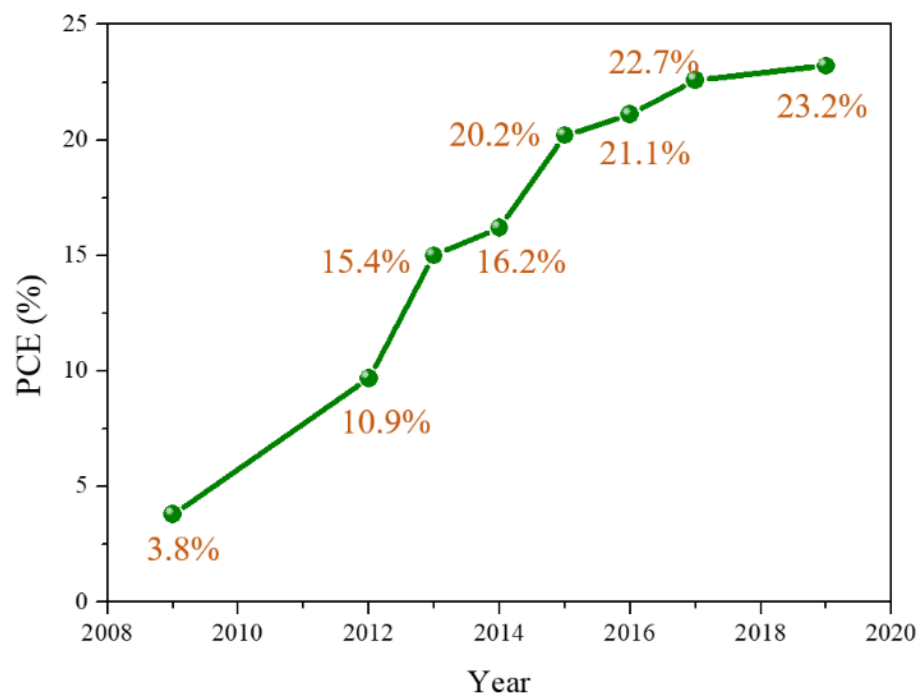
Figure 2.7. The development of best efficiency of perovskite solar cells.

Since the low quality of perovskite film significantly limits the photovoltaic performance of PSCs, Gratzel *et al*. used a sequential deposition route to prepare high-quality perovskite films and the PCE was enhanced to 15.0% with V_{oc} of 0.993 V, J_{sc} of 20.0 mA/cm^2 and FF of 0.73.[23] The PbI$_2$ is first deposited on the mesoporous TiO$_2$ layer. Then the TiO$_2$/PbI$_2$ composite film is dipped into a solution of MAI in 2-propanol. The colour of the film immediately changes from yellow to dark brown when the two components come to contact, indicating the formation of MAPbI$_3$. The concentration of MAI and dipping time could affect the quality of the resultant perovskite films. This work highlights the importance of the quality of perovskite films for the photovoltaic performance. Snaith *et al.* demonstrated the fabrication of planar heterojunction perovskite solar cells by using dual-source vapour deposition to prepare the perovskite (CH$_3$NH$_3$PbI$_{3-x}$Cl$_x$) films. The PCE is boosted to 15.4% with V_{oc} of 1.07 V, J_{sc} of 21.5 mA/cm^2 and FF of 0.68.[25] This work suggests that the mesostructured is not essential for the high-performance PSCs, which can simplify the

configuration of devices and low the fabrication cost.

In 2014, Seok *et al.* used solvent engineering method to improve the quality of perovskite films.[21] The mixed solvent consists of γ-butyrolactone and dimethylsulphoxide (DMSO) with volume ratio of 7:3. During the spin-coating of perovskite film, toluene is dropped onto the film to form a MAI-PbI$_2$-DMSO intermediate phase to retard the crystallization process. Based on this method, pin-hole free perovskite films with high crystallinity and low defect density are successfully prepared. By incorporating about 10% Br into MAPbI$_3$, the efficiency is boosted to a certified value of 16.2% with V$_{oc}$ of 1.09 V, J$_{sc}$ of 19.50 mA/cm^2 and FF of 0.76 and no hysteresis is observed. Lately, Yang et al. increased the efficiency to 19.3% by employing interface engineering technology.[37] Poly-ethyleneimine ethoxylated (PEIE) was used modify the ITO to reduce the work function from 4.6 eV to 4.0 eV, which could facilitate the electron transferring from ETL to ITO. Yttrium-doped TiO$_2$ (Y-TiO$_2$) was used to enhance electron extraction and transport. Based on these interface modifications, the efficiency of planar perovskite solar cells was boosted to 19.3% with V$_{oc}$ of 1.13 V, J$_{sc}$ of 22.75 mA/cm^2 and FF of 75.01%.

In 2015, Seok *et al.* used formamidinium lead iodide (FAPbI$_3$) with 15% of MAPbBr$_3$ as the light-harvesting unit to fabricate PSC with maximum efficiency of 18.4% with Voc of 1.11 V, Jsc of 22.5 mA/cm^2 and FF of 73.2%. It is found that the incorporation of MAPbBr$_3$ could stabilize the perovskite phase of FAPbI$_3$. This work is a pioneering strategy of using mix-cation perovskite which is most popular for the high-performance perovskite solar cells.[38] Later, Seok's group further enhanced the efficiency to 20.2% by intramolecular exchange of dimethylsulfoxide (DMSO) molecules intercalated with PbI$_2$ in the fabrication process of perovskite films.[39] This is the first efficiency reported above 20%. First, the PbI$_2$(DMSO) complex is precipitated by pouring toluene into 1.0 M PbI$_2$ solution dissolved in DMSO. Then the

PbI_2(DMSO) complex is annealed at 60 ℃ for 24 hours in a vacuum. The PbI_2(DMSO) complex powder dissolved in DMF is spin-coated to form dense PbI_2 film. Then FAI dissolved in isopropyl alcohol is spin-coated on the PbI_2 film followed by annealing to form $FAPbI_3$ perovskite. The PSCs based on this high quality $FAPbI_3$ perovskite show the maximum PCE of 20.2% with V_{oc} of 1.06 V, J_{sc} of 24.7 mA/cm^2 and FF of 77.5%.

In 2016, Saliba *et al.* reported that introduction of 5% Cs cation into FA/MA perovskite could significantly suppress the yellow phase impurities in the perovskite films due to the smaller iron radius of Cs. This strategy could substantially improve the efficiency and reproducibility of PSCs. The stabilized power output under maximum power point tracking reached 21.1%.[40]

In 2017, Seok *et al.* demonstrated that the incorporation of small amount of iodide ions into the perovskite solution could decrease the iodide vacancies, which serve as non-radiative recombination centers. The resultant PSCs shown the maximum efficiency of 22.7% with V_{oc} of 1.11 V, J_{sc} of 25.0 mA/cm^2 and FF of 0.817.[41] In 2019, You *et al.* used PEAI to passivate the defects locating at the surface and grain boundaries of perovskite films. The efficiency is enhanced to 23.56% with V_{oc} of 1.16 V, J_{sc} of 24.9 mA/cm^2 and FF of 81.4%. The device shows a quasi-steady output of 23.2%. This is the record efficiency reported in the literatures so far.[42]

In the short time of only seven years, the efficiency of perovskite solar cells has been increased from 3.8% to 23.2% with the efforts in optimizations of device configuration, charge transporting layers and crystal process of perovskite films. Fundamentally, the unique optoelectronic properties are the most important factor for the high-performance of perovskite solar cells.

2.6.2 The efficiency development for flexible perovskite solar cells

Flexible perovskite solar cells (FPSCs) are supposed to be the foremost commercialization option due to the facile mass-production by the roll to roll printing process, which can further decrease the cost substantially. Furthermore, the development of FPSCs can fulfill the highly diverse applications, such as wearable and portable electronics, unmanned systems, smart buildings and aerospace applications.[3-5] Thus, the fabrication of lightweight FPSCs with high efficiency and mechanical robustness is of great significance for the development and commercialization of perovskite photovoltaic technology. To date, many efforts are dedicated to fabricating novel FPSCs with high efficiency and superior bending durability, such as tailoring the precursor composition, optimizing transporting layers, and introduction of additives in the perovskite precursors.[19, 43-45] The maximum efficiency of flexible perovskite solar cells is boosted to 19.38% so far.[46] We will summary the key achievements on the improvement of flexible perovskite solar cells along the development.

The fabrication of mesoporous TiO_2 needs about high temperature ($\sim 500℃$), which is detrimental for the flexible substrates. Thus, low temperature fabrication techniques are needed to prepare flexible perovskite solar cells. In 2013, Kumar *et al.* grew ZnO nanorods by chemical bath deposition (CBD) on electrodeposited ZnO compact layer, which was prepared on the PTE substrate.[47] The fabrication process of ZnO layer needs the temperature lower than 100 ℃. The prepared flexible perovskite solar cells show the efficiency of 2.62%. Snaith *et al.* used all low temperature processing to prepare flexible perovskite solar cells with the inverted structure of PET/ITO/PEDOT:PSS/$CH_3NH_3PbI_{3-x}Cl_x$/PCBM/TiO_x/Al.[48]   The   maximum

efficiency could reach 6.3% with V_{oc} of 0.9 V, J_{sc} of 14 mA/cm^2 and FF of 0.47. The low FF was due to the low quality and surface coverage of perovskite films. Liu et al. employed low temperature processed ZnO nanoparticles as electron transporting layer to prepare flexible perovskite solar cells.[49] Due to the high electron mobility of ZnO, the efficiency reached 10.2% with V_{oc} of 1.03 V, J_{sc} of 13.4 mA/cm^2 and FF of 73.9%.

In 2015, Seok *et al.* reported a new route to synthesize highly dispersible Zn_2SnO_4 nanoparticles at low temperature to serve as electron transporting layer for the high-performance flexible perovskite solar cells.[50] Due to the high mobility and light transmittance of Zn_2SnO_4 film, the PCE could reach 15.3%, with V_{oc} of 1.05 V, J_{sc} of 21.6 mA/cm^2 and FF of 0.67. In 2016, Yang et al. used solid-state ionic-liquids (ss-IL), 1-benzyl-3-methylimidazolium chloride, as the electron transporting layer to prepare flexible perovskite solar cells.[51] Due to the suitable band energy level alignment between ss-IL and perovskite, the maximum PCE is enhanced to 16.09% with V_{oc} of 1.07 V, J_{sc} of 22.72 mA/cm^2 and FF of 66.2%. Yoon et al. demonstrated that CVD-grown graphene was used as bottom transparent electrode to fabricate flexible perovskite solar cells with device configuration of PEN/Graphene/MoO_3/PEDOT:PSS/$MAPbI_3$/C60/BCP/LiF/Al.[52] The device performance reached 16.8% with V_{oc} of 1.0 V, J_{sc} of 21.7 mA/cm^2 and FF of 0.78. The flexible device based on ITO electrode demonstrate the efficiency of 17.3% with V_{oc} of 0.97 V, J_{sc} of 21.5 mA/cm^2 and FF of 0.83. The flexible devices could maintain more than 90% of original efficiency after 1000 bending cycles and 85% after 5000 bending cycles with a bending radius of 2 mm. In 2017, Bi *et al.* reported that it is found the perovskite films deposited on glass and flexible substrates with same perovskite precursor show different morphology and crystallinity.[43] Thus, the composition of perovskite precursor for the flexible devices is tailored properly and the resultant flexible perovskite solar cells show the efficiency of 18.1% with V_{oc} of

1.06 V, J_{sc} of 22.8 mA/cm^2 and FF of 74.6%.

Feng *et al.* reported that a novel dimethyl sulfide was used an additive to reach with Pb^{2+} to form a chelated intermediate, which could slow down the crystallization process and lead to the enlargement of grain size.[19] The prepared flexible devices demonstrate a high efficiency of 18.40% with V_{oc} of 1.103 V, J_{sc} of 22.48 mA/cm^2 and FF of 0.742. Wu et al. presented a record efficiency of flexible perovskite solar cells so far by ligand and additive synergetic process.[46] The perovskite films are prepared by using FAI·PbI$_2$·NMP+x%MACl as the precursor. Based on the perovskite films with high crystallinity and low trap density, the flexible devices demonstrate a record PCE of 19.38% with V_{oc} of 1.07 V, J_{sc} of 23.45 mA/cm^2 and FF of 77.23.

2.7   Current challenges for perovskite solar cells

2.7.1 Long-term stability

Operation stability of perovskite solar cells is critical for the future commercialization. The stability of PSCs is significantly enhanced by the efforts in devices configuration, materials modification and encapsulation techniques in these years. The lifetime is improved from several minutes to thousand hours. Most of the stability test is under the condition where only one of conditions is applied, such as heating, moisture or light illumination. Thus, many efforts are needed to further improve the stability of PSCs under more harsh and practical conditions.[30]

The causes of instability of PSCs are mainly from the instability of chemical materials of the device components under the harsh conditions. For the perovskite active layer, when the perovskite films (for example, MAPbI$_3$) are exposed to moisture, the MAPbI$_3$ degraded to MAI, PbI$_2$ and HI. HI would further degrade to I$_2$ and H$_2$ by a

redox reaction in the presence of oxygen.[53-55] For the electron transporting layer, TiO_2 could extract electrons from I^- to generate I_2 under the light, specially the ultraviolet (UV) light, due to the photocatalyst function of TiO_2.[56-57] This could lead to the degradations of perovskite films and interface between perovskite and electron transporting layer. Many UV-stable electrons transporting layers, such as BaSnO3, are explored to replace the TiO_2 to enhance the light stability of perovskite solar cells.[58] Interfacial modification is also investigated to improve the stability, such as CsBr, Sb_2S_3.[57, 59] The most used hole transporting layers, such as spiro-oMeTAD, PTAA, also have moisture or thermal instability due to the dopants. The metal electrodes such as Ag and Al suffer from corrosion due to the ion immigration in the perovskite films, which could degrade the stability and efficiency of devices significantly.[60-61] Interfacial modifiers, such as Cr and reduced graphene oxide have been deposited before thermal evaporation of metal electrodes to prevent the metal diffusion.[62-63] The stability could be improved apparently. Although the long-term stability of PSCs has been improved intensively, it can be realized to simultaneously hold the high efficiency (more than 22%) and good operation stability for PSCs currently. Thus, more efforts should be focused on clarifying degradation mechanism and exploring new chemically stable materials.

2.7.2   J-V curve hysteresis

Current-voltage characterization of perovskite solar cells is the main method to determine the power conversion efficiency of the devices. However, there is hysteresis between the J-V curves under different sweeping direction and scanning rate. This phenomenon leads to the inaccurate determination of efficiency for PSCs according to the J-V characterization.[64] Many efforts are devoted to finding the mechanism of hysteresis and solving this issue. However, the origin of this phenomenon is still under

controversy. Some theories are proposed to try to clarify the origins of J-V hysteresis.

Tress *et al.* show that the hysteresis in current-voltage scans should be related to the charge carrier collection efficiencies which depend on the build-in potential, which is strongly affected by the ions accumulated at the interfaces of the electrodes.[65-66] Ion migration is prohibited to mitigate the hysteresis phenomenon. Meloni *et al.* supported that the migration of halide ion causes the hysteresis in the J-V characterization by a combined experimental and computational approach.[66] Huang *et al.* demonstrated that the trap states on the surface and grain boundaries of perovskite films are the origin of current-voltage hysteresis.[67] It is found that the deposition of fullerene layers onto the perovskite films could effectively passivate the defects and eliminate the hysteresis.

2.7.3 Toxicity of materials

The toxicity of raw materials and solvents during fabrication process is a major issue retarding the commercialization. The lead contained in PSCs would be released to the environment and lead to the hazard to human health. Thus, lead-free perovskites are considered as a solution for this issue. Theoretically, the Pb site can be replaced by tin (Sn), germanium (Ge), bismuth (Bi) and antimony (Sb).[68] Due to the suitable bandgap and high light absorption coefficient, the tin-based perovskites are promising to substitute the lead to fabricate highly efficient and environment-friendly PSCs. The maximum PCE of tin-based perovskite solar cell is 9.6%, which is much lower than the lead-based devices.[69] That is attributed to that Sn^{2+} could be easily oxidized to Sn^{4+}, which could dope the perovskites and increase the concentration of holes. This could result in severe non-radiative recombination of charge carriers. In order to solve this issue and further improve the efficiency of tin-based perovskite solar cells, many kinds of additives, such as two-dimensional perovskites,[70] antioxidants and reducing

agents,[71] to prevent the oxidization of Sn^{2+}.

The solvents, such as DMF and chlorobenzene, are toxic for human. The mass production of PSCs would lead to the pollution to the environment. Thus, green solvents are investigated to replace the toxic ones.[72] In addition, the solvent-free fabrication technologies are also invented to avoid the used of toxic solvents.[27]

Although many technologies are used to solve the issue of toxicity of the materials and solvents, the PCEs of PSCs based on these technologies are far lower than those of PSCs based on lead and toxic solvents. Thus, this issue should be further solved to fabricate high efficiency perovskite with non-toxic materials and solvents, which could accelerate the commercialization of PSCs.

2.8   Summary and Perspectives

Recently, perovskite solar cells, as the star of photovoltaic family, attract tremendous attentions from all over the world due to the high photovoltaic performances. In this chapter, we have reviewed the fundamental properties of perovskite materials, such as crystal structure, optoelectronic properties, fabrication approaches of single crystal and thin films, efficiency development of rigid and flexible devices and the current challenges. The main problems and solutions are summarized. It can be sure that perovskite solar cells are promising alternatives to silicon solar cells in the future. Before the commercialization, the toxicity issue of raw materials and solvents should be solved properly. The long-term operation stability should be improved to reach the commercial requirements. With the development of fabrication techniques, the up-scaling production would be realized and accelerate the commercialization of PSCs.

Chapter 3   Performance enhancement of perovskite solar cells induced by lead acetate as an additive

The crystallinity of organic-inorganic hybrid lead halide perovskite active layers is critical to the performance of perovskite solar cells (PSCs). However, it is a challenge to control the crystallization process of perovskite films by solution process. Here, we demonstrate the fabrication of high-efficiency PSCs by employing lead acetate ($PbAc_2$) as an additive in the perovskite precursor for the first time. By adding a few percent of $PbAc_2$ (molar ratio with respect to PbI_2) into the precursors, the perovskite crystallization process is significantly retarded, leading to pinhole-free perovskite films with large grains and low defect densities. As result, the power conversion efficiencies and stability of the PSCs are substantially improved. This work provides a convenient and unique approach for preparing high-quality perovskite films that can be used in photovoltaics as well as other optoelectronic devices.

3.1   Introduction

Perovskite solar cells (PSCs) based on organic-inorganic hybrid lead halide perovskite materials have attracted much attention in recent years due to their rapidly improved efficiencies and potential for low-cost manufacturing. Perovskites are materials with the formula ABX_3, where A and B are cations of different sizes (A being larger than B) and X is an anion. Organic-inorganic hybrid lead halide perovskites have demonstrated many unique properties, including tunable bandgap, high absorption coefficient, broad absorption spectrum, high carrier mobility and long carrier diffusion

lengths, which enable the rapid improvement of the power conversion efficiency (PCE) of PSCs from 3.8% to 22.1% [73-79]. In general, there are two types of architectures for the PSCs, including n-i-p (regular) and p-i-n (inverted) structures dependent on the bottom charge transport layers [80]. For the n-i-p regular structure, high efficiency PSCs can be realized using n-type inorganic semiconductor like TiO_2 and SnO_2 as the electronic transport layer on the bottom [81-87]. The p-i-n architecture called inverted structure is more suitable for flexible solar cells and large-scale low-cost production because organic electron and hole transport layers can be used in the devices. However, the perovskite films growing from organic hole transport layers such as Poly[bis(4-phenyl)(2,4,6-trimethylphenyl)amine]   (PTAA)   and Poly(3,4-ethylenedioxythiophene):polystyrene sulfonate (PEDOT:PSS) normally show small grain size and high density grain boundaries [88-89]. The low crystallinity of the perovskite films in the inverted PSCs may lead to low PCEs as well as poor device stability [90-95]. Therefore, preparing perovskite thin films with high crystallinity is critical to the performance of inverted PSCs.

To date, various techniques, such as solvent annealing [96], hot casting [97], vacuum-flash treatment [98], and Ostwald ripening process [99], have been developed to improve the crystallinity of perovskite films. Incorporating additives or dopants into perovskite precursors to optimize the crystallizing process are also useful approaches. For example, Snaith's group improved the crystal quality and reduced the non-radiative recombination rate by introducing aluminum acetylacetonate to the perovskite precursor solution [100]. Grätzel's group exhibited the highest FF of 0.85 by adding a small amount of H_2O into the precursor solution to get high quality perovskite thin films [101]. Sargent's group showed that by adding phenyl-C61-butyric acid methyl ester (PCBM) directly into the perovskite precursor solution, PCBM could be distributed at the grain boundaries of the perovskite films,

leading to the passivation of the trap states and suppression of hysteresis [89].

Although the reported approaches are promising, the quality of the perovskite films should be further improved by novel methods to alleviate trap-assisted carrier recombination in PSCs. The most convenient way is to control the growth of the perovskite films with a view to obtaining better crystallinity of the films. We find that $PbAc_2$ can act as a crosslinking agent to make perovskite intermediate phase more stable by forming strong hydrogen bonding. The stable intermediate phase can retard the crystallization process and lead to better morphology and larger grains of perovskite films. Moreover, the $PbAc_2$ additive can generate PbI_2 in the perovskite films, which will passivate defects at grain boundaries. Consequently, the carrier lifetimes in the PSCs are prolonged significantly and the densities of trap states are reduced by one order of magnitude due to the addition of $PbAc_2$ for only 3 % (molar ratio with respect to PbI_2). We find that the device efficiency is relatively improved for about 10% and the device stability is greatly enhanced as well. Although $PbAc_2$ has been used as a lead source to fabricate pin-hole free and ultra-smooth perovskite films,[102-107] the utilization of it as an additive for enhancing the crystallization of perovskite films has never been reported before. Therefore, this work provides a novel and cost-effective approach to improving the performance of PSCs.

3.2   Devices fabrication and characterization

Materials: CH_3NH_3I was purchased from Dyesol Ltd. PbI_2, bathocuproine (BCP), dimethylformamide (DMF), Poly[bis(4-phenyl)(2,4,6-trimethylphenyl)amine] (PTAA) and dimethyl sulfoxide (DMSO) were purchased from Sigma-Aldrich Co. LLC. Lead acetate trihydrate ($PbAc_2 \cdot 3H_2O$) was purchased from Aladdin Ltd. Phenyl-C71-butyric acid methyl ester (PCBM) was purchased from Nano-C Ltd..

Preparation of PSCs: ITO/glass substrates were sequentially washed with distilled water, acetone and isopropanol (IPA). Then, PTAA dissolved in toluene (2.0 mg/mL) was spin-coated on the ITO/glass substrates at a spin rate of 5000 rpm for 40 s. The films were subsequently annealed on a hotplate at 100 ℃ for 10 min. The perovskite films without $PbAc_2$ in the precursor were prepared by spin-coating the perovskite precursor solution (CH_3NH_3I: 159 mg, PbI_2: 461 mg, DMF: 600 mg, DMSO: 78 mg) at 4000 rpm for 30 s. During the spin coating process, 0.5 ml of diethyl ether was slowly dripped on the rotating substrate in 10 secs after starting. To introduce $PbAc_2$ as an additive in the precursor solution, $PbAc_2 \cdot 3H_2O$ was heated to 100 ℃ to lose the crystal water and then added into the perovskite precursor with different ratios. All perovskite films were annealed at 65 ℃ for 1 min and then at 100 ℃ for 10 min. Next, electron transport layers (ETLs) were prepared by spin coating a solution of PCBM in chlorobenzene (20 mg/ml) at 3000 rpm for 40 s, followed by thermal annealing at 90 ℃ for 20 min to crystalize PCBM. BCP dissolved in methanol (0.5 mg/ml) was spin-coated on the PCBM films at 4000 rpm for 30 s. Finally, devices were completed with the evaporation of Ag top electrodes through a shadow mask. The area of the PSC is designed to be 6 mm^2.

Material and device characterization: Scanning electron microscopy (SEM) images of perovskite thin films were obtained under a Hitachi S-4300 microscope. The absorption spectra of perovskite films were measured by using a UV-Vis spectro-photometer (UV-2550, Shimadzu, Japan). X-ray diffraction (XRD) measurement was performed using a Rigaku SmartLab X-ray Diffractometer operating at room temperature. Time-resolved photoluminescence (PL) measurements of the samples were carried out by using an Edinburgh FLSP920 fluorescence spectrophotometer. A 485-nm laser was used as an excitation light source. The current density versus voltage (J-V) characteristics of the PSCs were measured

by using a Keithley 2400 source meter under the illumination of a AM 1.5 solar simulator with a light intensity of 100 mW/cm^2 (Newport 91160, 300W) and a scan rate of 30 mV/s. The light intensity was calibrated with a standard silicon solar cell. The external quantum efficiencies (EQEs) of the PSCs were measured with a standard test system, including a xenon lamp (Oriel 66,02, 300W), a Si detector (Oriel 76175_71580), a monochromator (Newport 66902) and a dual channel power meter (Newport 2931_C).

3.3   Results and discussion

Planar PSCs with the inverted device architecture of glass/ITO/PTAA/perovskite/PCBM/BCP/Ag, as shown in **Figure 3.1a,** are prepared by solution process in a glovebox filled with high-purity nitrogen gas. Different amount of PbAc$_2$ is added in perovskite precursor solutions to investigate its effect on the photovoltaic performance of the devices. **Figure 3.1b** shows the photocurrent–voltage (*J-V*) curves of representative PSCs with and without 3% PbAc$_2$ (molar ratio with respect to PbI$_2$) added in the perovskite precursor in device fabrication. It can be found that the PCEs of the devices are substantially enhanced by the PbAc$_2$ additive. The photovoltaic characteristics of all PSCs with different amount of PbAc$_2$ are shown in **Figure 3.2** and **Table 3.1**. It is notable that 3% PbAc$_2$ additive can lead to the maximum enhancement of PCE.
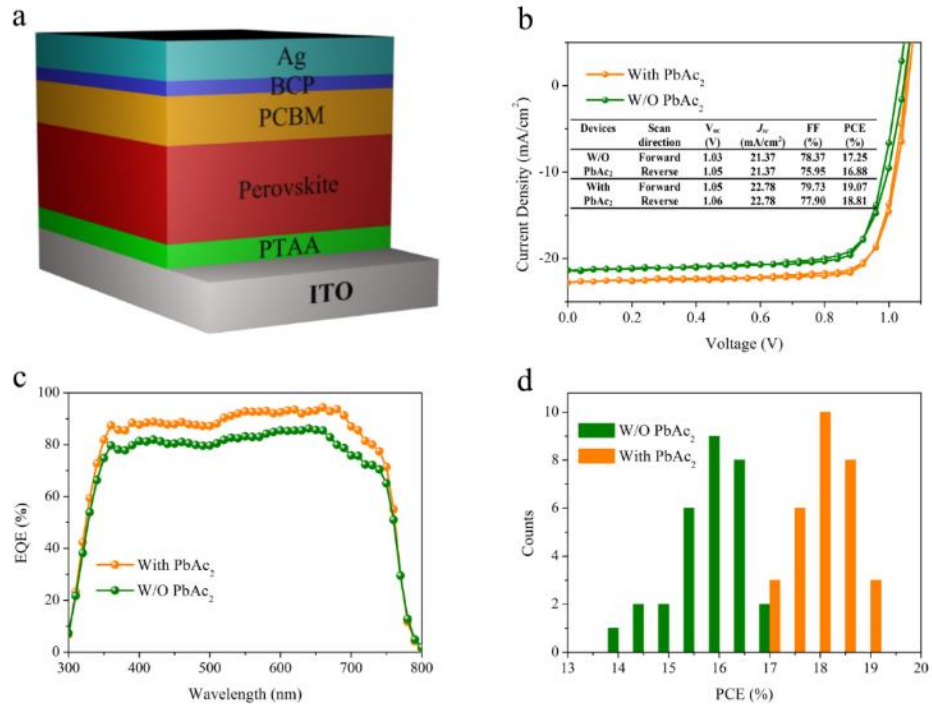
Figure 3.1. a) Schematic diagram of an inverted planar perovskite solar cell. b) *J-V* curves and c) EQE curves of PSCs with or without the $PbAc_2$ additive in device fabrication. d) PCE distribution for devices with or without $PbAc_2$ in perovskite precursor solutions.
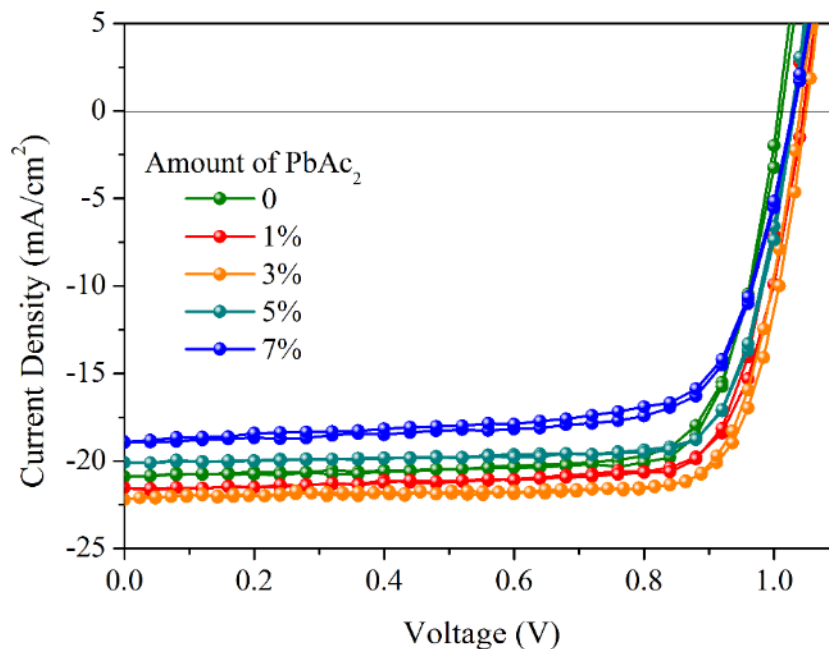
Figure 3.2. J-V curves of PSCs with various amount of $PbAc_2$ (molar ratio with respect to PbI_2) in the perovskite precursor solution.

Table 3.1. Photovoltaic parameters of PSCs with different amount of $PbAc_2$ (molar ratio with respect to PbI_2) in the perovskite precursor solution (average values of 6 devices).

Amount of $PbAc_2$ (%)	V_{oc} (V) (Forward)	J_{sc} (mA/cm^2) (Forward)	FF (%) (Forward)	PCE (%) (Forward)
0	1.01 (1.00)	20.89 (20.89)	79.56 (76.54)	16.15 (16.62)
1	1.04 (1.03)	21.53 (21.53)	77.66 (78.87)	17.39 (17.49)
3	1.05 (1.04)	22.20 (22.20)	79.06 (79.57)	18.43 (18.37)
5	1.03 (1.03)	20.08 (20.08)	79.87 (79.83)	16.52 (16.51)
7	1.03 (1.03)	18.94 (18.94)	73.46 (71.92)	14.33 (14.00)

As shown in **Figure 3.1b**, the control device without $PbAc_2$ additive demonstrates a PCE of 17.25 (16.88) %, an open circuit voltage (V_{oc}) of 1.03 (1.05) V, a short-circuit current density (J_{sc}) of 21.37 (21.37) mA/cm^2 and a fill factor (FF) of 78.37 (75.96) % measured under forward (reverse) voltage scan. The performance is comparable with the results reported in literature [108]. The device with 3% $PbAc_2$ exhibits a PCE of 19.07 (18.81) %, an V_{oc} of 1.05 (1.06) V, a J_{sc} of 22.78 (22.78) mA/cm^2 and a FF of 79.73 (77.90) % measured under forward (reverse) voltage scan, demonstrating overall enhancement on photovoltaic performance. The stable output PCEs for the two devices with and without $PbAc_2$ are 18.50 % and 16.13 %, respectively as shown in **Figure 3.3**. **Figure 3.1c** shows the external quantum efficiency (EQE) spectra of the devices with or without $PbAc_2$. The corresponding integrated current densities are 21.78 mA/cm^2 and 20.86 mA/cm^2, respectively. However, we find that there is no obvious enhancement in the light absorbance of the films after the introduction of $PbAc_2$ as shown in **Figure 3.4**, indicating that the film thickness was not changed. It is also confirmed by the SEM images of the perovskite films with or without $PbAc_2$ shown in **Figure 3.5**. The two films have the same thickness of about 400 nm. Therefore, the increase of EQE induced by $PbAc_2$ additive is mainly due to the improved quality of perovskite films. The statistics of PCE distribution shown in **Figure 3.1d** demonstrates the average PCEs increased from 15.87±0.65 % to 18.03±0.57 % by $PbAc_2$ and the PCE enhancement is 13.6%.
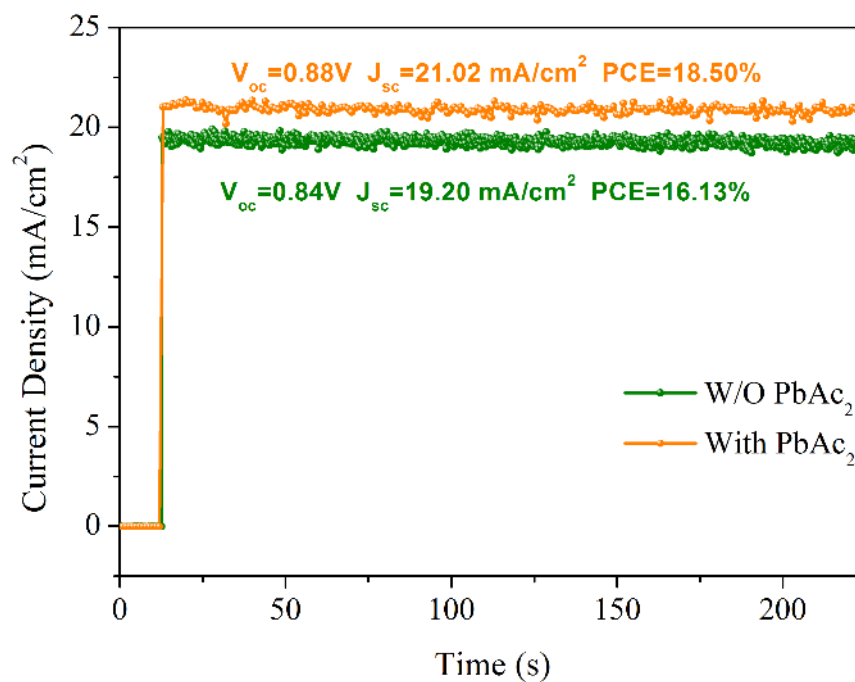
Figure 3.3. Stabilized photocurrent density of the PSCs with or without PbAc$_2$ additive.
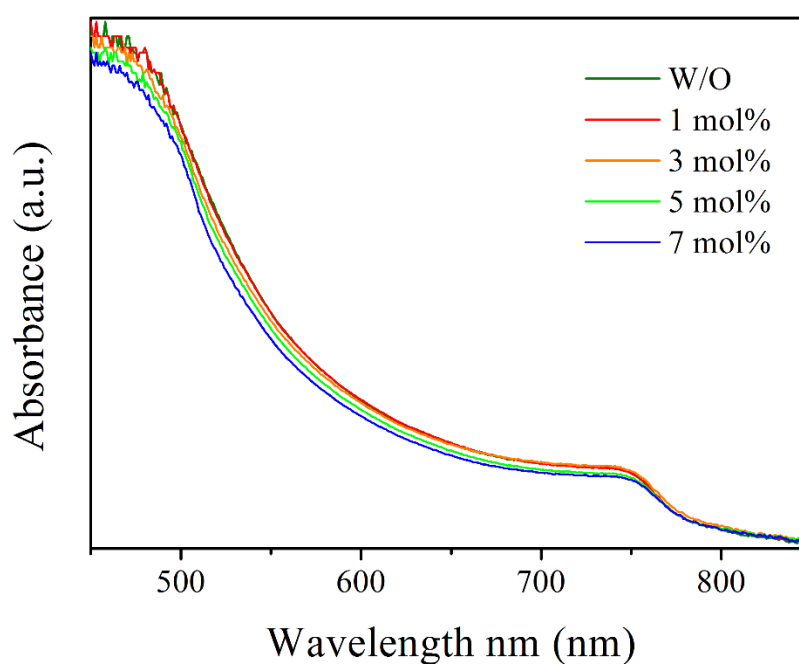
Figure 3.4. Absorbance spectra of MAPbI$_3$ films with various amount of PbAc$_2$ additives (molar ratio with respect to PbI$_2$) in the precursors.
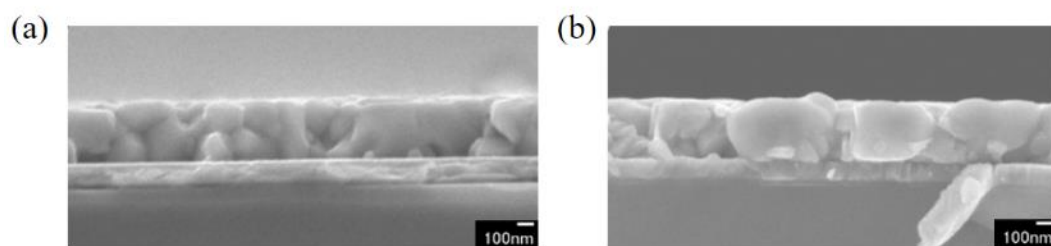
Figure 3.5. The cross-section SEM pictures of perovskite films without (a) and with (b) $PbAc_2$ in the precursor.

To explore the underling mechanism for the performance enhancement, we observed the morphology of the perovskite films with or without $PbAc_2$. **Figure 3.6a and b** show the top-view scanning electron microscopy (SEM) images of perovskite films deposited on PTAA films without and with 3 % $PbAc_2$ in perovskite precursors with DMF as solvent, respectively. We can find that there are many pinholes in the perovskite film without the $PbAc_2$ additive and the average grain size is around 200 nm. In comparison, the $PbAc_2$ -added film demonstrates much larger grains with the average size of 350 nm. This result indicates that the addition of $PbAc_2$ could improve the morphology of perovskite film significantly. **Figure 3.6c** and **d** shows the perovskite films based on the mixed solvent of DMF/DMSO without and with the addition of $PbAc_2$, respectively. It is interesting to note that the introduction of DMSO makes the effect of $PbAc_2$ more obvious. The grain size of the perovskite control sample shows in **Figure 3.6c** is about 250 nm. In contrast, the perovskite film with 3 % $PbAc_2$ additive in **Figure 3.6d** exhibits a larger average grain size of about 500 nm. It can be observed that DMSO only could make the perovskite film smoother by comparing the SEM images shown in **Figure 3.6a** and **3.6c**, while the grains are hardly enlarged without the addition of $PbAc_2$.
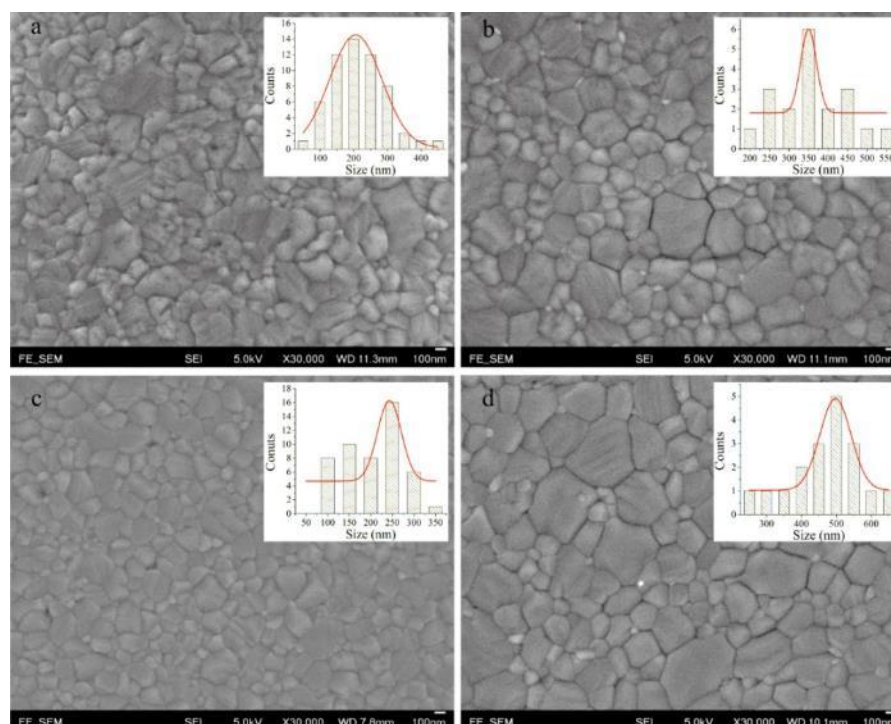
Figure 3.6. Top-view scanning electron microscopy (SEM) images of MAPbI$_3$ films deposited on PTAA substrates with the perovskite precursor of a) MAI and PbI$_2$ in DMF, b) MAI, PbI$_2$ and 3% PbAc$_2$ in DMF, c) MAI and PbI$_2$ in DMF/DMSO, d) MAI, PbI$_2$ and 3% PbAc$_2$ in DMF/DMSO. The scale bar is 100 nm.

For the perovskite films with different amount of PbAc2, the average grain size increases with the increase of PbAc2 percentage when the addition amount is less than 3 % and then decreases with the increase of addition level as shown in **Figure 3.7** for SEM images. Therefore, the incorporation of PbAc2 with a suitable amount is favorable for the growth of perovskite crystals. The decreased number of grain boundaries in perovskite films could lead to the reduction of carrier recombination and the improvement of J_{sc}, V_{oc} and *FF*, which are consistent with the J-V performance of our devices. However, excess PbI$_2$ can be observed on the surface of films when the addition level is higher than 5%, which is unfavorable to the performance of PSCs due to the low conductivity and large bandgap of PbI$_2$. [109-110] The excess of PbI$_2$ in the films can also be confirmed by X-ray diffraction (XRD) patterns of the films shown in **Figure 3.8**, where the diffraction peak of PbI$_2$ increases with the increase of PbAc2

addition level.
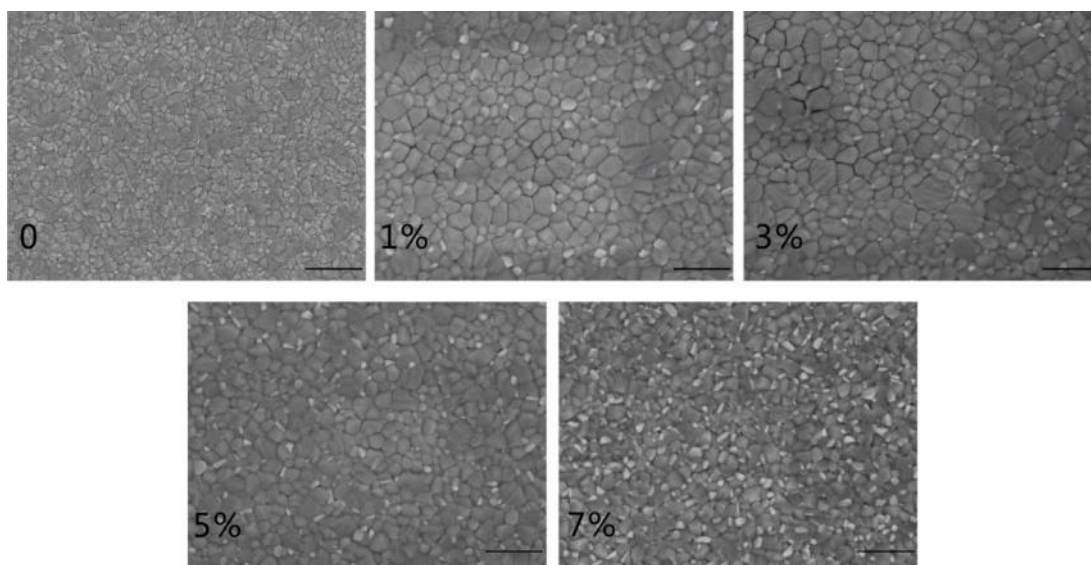
Figure 3.7. Top-view scanning electron microscopy (SEM) images of MAPbI$_3$ films with different amount of PbAc$_2$ in the precursor solutions deposited on PTAA substrates. The scale bar is 1μm.
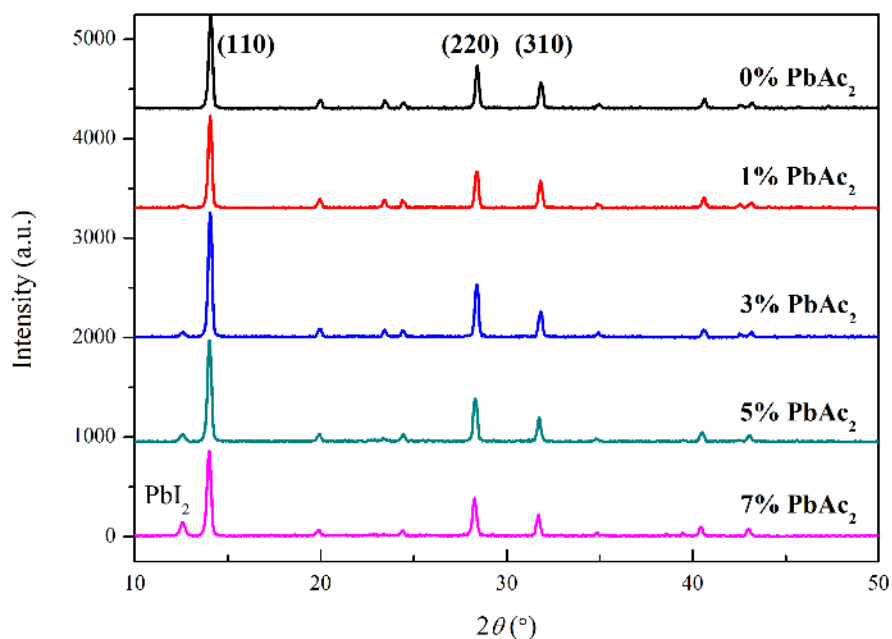
Figure 3.8. XRD patterns for perovskite films with different amount of PbAc$_2$ in the precursor.

In our experiments, we observed that the addition of PbAc$_2$ in precursor solutions could dramatically retard the formation and crystallization of perovskite films. As

shown in **Figure 3.9a**, the perovskite film without $PbAc_2$ demonstrates brown color immediately after spin-coating. In contrast, the perovskite film with $PbAc_2$ in the precursor appears transparent in several minutes after spin-coating, as shown in **Figure 3.9b**. When more $PbAc_2$ is incorporated in a precursor, longer time is needed for the resulting perovskite film to be brown, as shown in **Figure 3.9c**. The perovskite films are fabricated by precursors using DMF/DMSO mixed solvents. The retarded reaction/crystallization process is also observed when using DMF solvent only as shown in **Figure 3.10**, indicating that DMSO is not essential to this effect. In order to explore how $PbAc_2$ retards the perovskite reaction/crystallization process, XRD measurements are conducted on the perovskite films before and after thermal annealing. As shown in **Figure 3.9d**, for the precursor without $PbAc_2$, the XRD spectra of the resulted perovskite films before and after a thermal annealing at 100 °C are quite similar, which suggests that the crystallization process is almost completed before annealing. **Figure 3e** shows the XRD patterns for $PbAc_2$ -contained perovskite films before and after annealing. For the perovskite film before annealing, MAI·PbI_2·DMF intermediate phase is detected.[111-112] The intermediate phase induced by $PbAc_2$ can also be observed under SEM, as shown in **Figure 3.11.** After annealing, the intermediate phase disappears and the PbI_2 phase can be detected. These results indicate that the introduction of $PbAc_2$ could lead to the more stable intermediate phase that retards the crystallization of perovskite films.
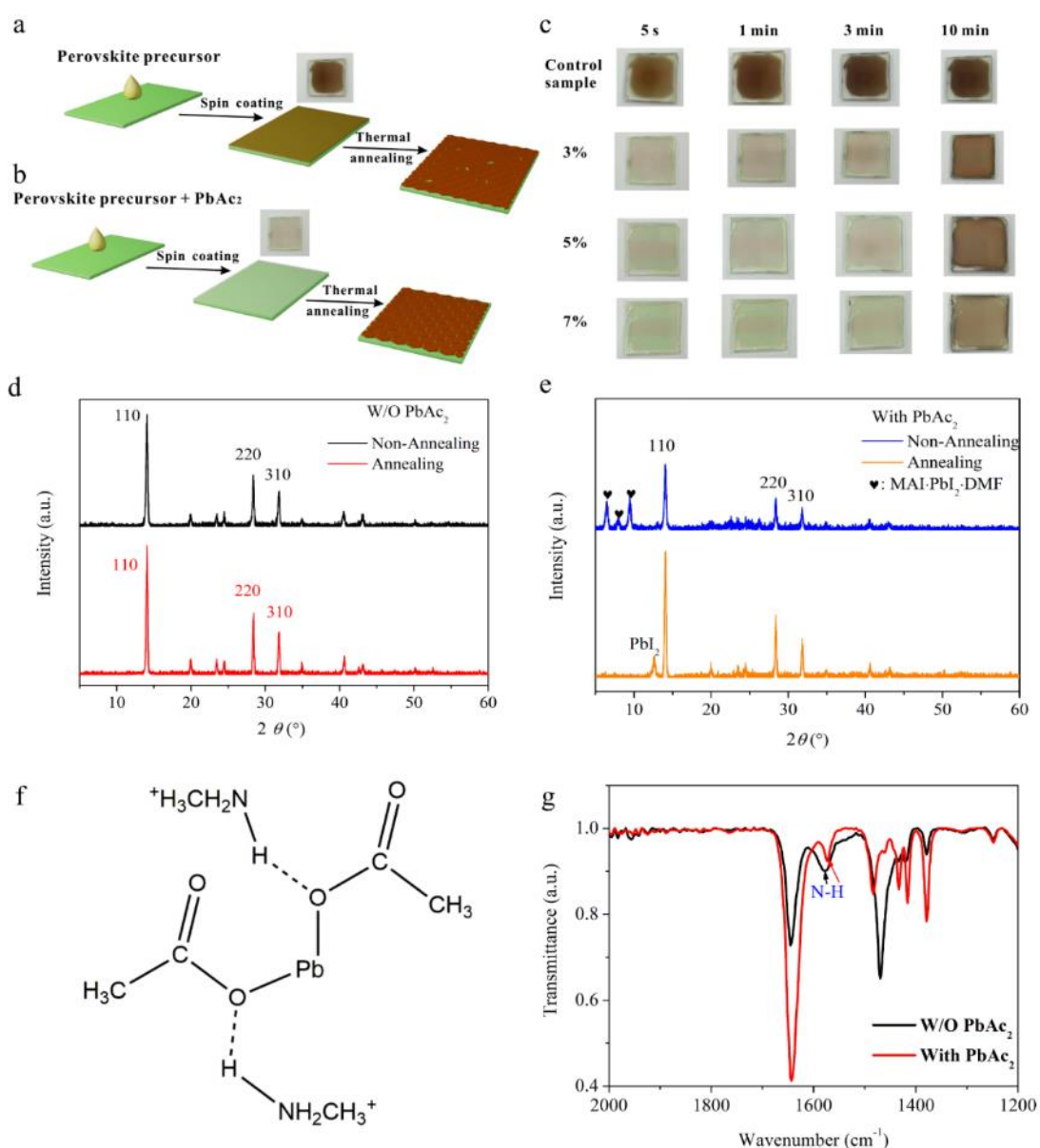
Figure 3.9. Schematics of perovskite film preparation a) without and b) with PbAc$_2$ in the precursor solution. c) Morphology evolution of perovskite films at room temperature after the coating of precursor solutions with different amount of PbAc$_2$. d) X-ray diffraction (XRD) patterns of control perovskite films before and after a thermal annealing at 100 °C. e) XRD patterns of PbAc$_2$ -doped perovskite films before and after a thermal annealing at 100 °C. f) Schematic diagram of the hydrogen bonding formation between PbAc$_2$ and MAI. g) FTIR spectra of perovskite films without and with PbAc$_2$ in the precursors.

The retarded crystallization process can lead to a low nucleation rate of perovskite grains and more opportunities for the grains to grow bigger.[82, 93, 113-114] The perovskite

crystallization process consists of supersaturation, nucleation and crystal growth. When the film reaches supersaturation due to the evaporation of solvent, nuclei start to form and grow to bigger grains.[115] The nucleation density or rate is critical to the grain size and morphology of perovskite films. It has been reported that low nucleation density can lead to the formation of large grains while higher nucleation density or rate can result in continuous films with smaller grains.[20, 115-116] Therefore, this effect could be responsible for the increased average grain size of perovskite films with the $PbAc_2$ additive.
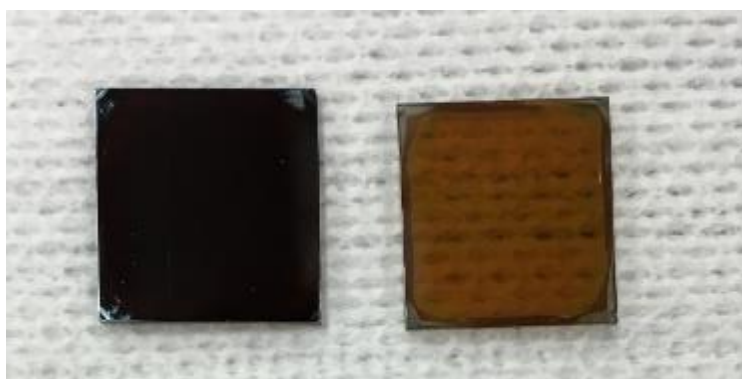
Figure 3.10. Photo of perovskite films (left) without and (right) with $PbAc_2$ (3%) after spin-coating.
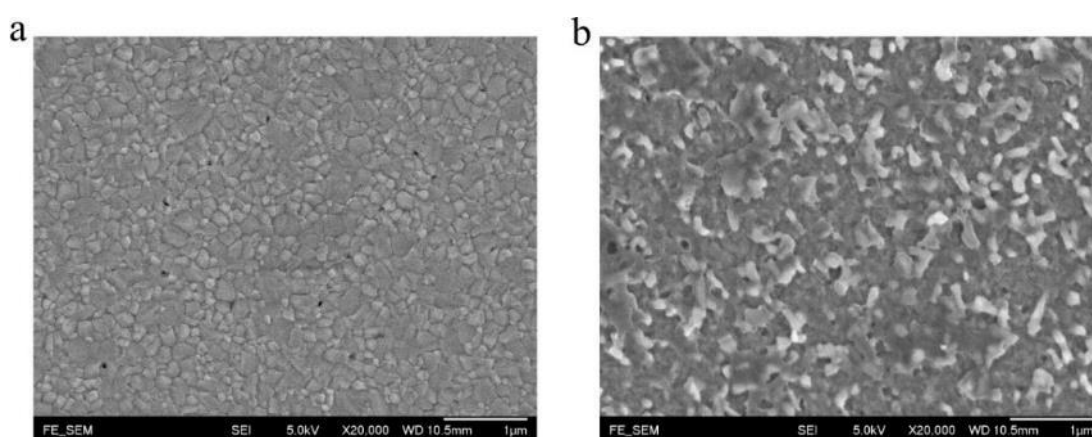
Figure 3.11. SEM pictures of non-annealed perovskite films without (a) and with (b) $PbAc_2$ (3%) in the precursor.

Regarding the mechanism of the formation of intermediate phase, we consider that strong hydrogen bonding is formed by introducing $PbAc_2$ into the precursor solution.

As presented in **Figure 3.9f**, the hydrogen bonding can be formed by the interaction between MA^+ and O in $PbAc_2$.[117-118] This hydrogen bonding makes $PbAc_2$ serve as crosslinking agent in the intermediate phase to improve its stability. This is similar with the case of introducing alkylphosphonic acid ω-ammonium chlorides into the perovskite precursor.[117] Fourier transform infrared spectroscopy (FTIR) transmission spectra of unannealed perovskite films without or with $PbAc_2$ (3%) in the precursor were characterized to verify the hydrogen bonding between MA^+ and $PbAc_2$. As shown in **Figure 3.9g**, the absorption peak at the wavenumber of 1580 cm^{-1} belongs to the N-H bond of the MA^+ group. For the perovskite film with 3% $PbAc_2$, the N-H bond has a red-shift to 1571 cm^{-1},[119] indicating that the hydrogen bonding affects the neighboring N-H bonds by decreasing their vibration frequency.[120] This more stable intermediate phase requires longer time and higher energy to convert to perovskite structure and can retard the crystallization process of the perovskite film. During thermal annealing process, the following reaction will occur in perovskite thin films :[121]

$$CH_3NH_3I + PbI_2 + xPb(CH_3CO_2)_2 \rightarrow (1-2x)CH_3NH_3PbI_3 + 2xCH_3NH_2 + 3xPbI_2 +$$

$$2xCH_3COOH \uparrow \ . \tag{1}$$
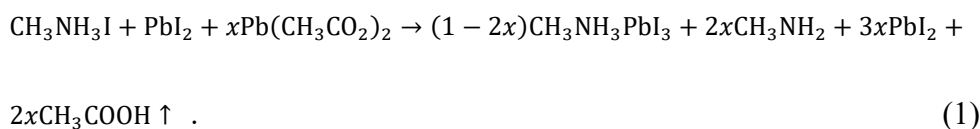
So the addition of 3% $PbAc_2$ can induce 9% excess PbI_2. We also noticed that the direct addition of 9% excess PbI_2 in a precursor cannot retard the reaction/crystallization of a perovskite film as shown in **Figure 3.12**. The generated PbI_2 mainly locates at the grain boundaries, as shown in **Figure 3.7**. It has been reported that suitable amount of PbI_2 could passivate the grain boundaries to reduce the density of the trap states in perovskite films,[109-110, 122] which will also be helpful for improving the device performance.
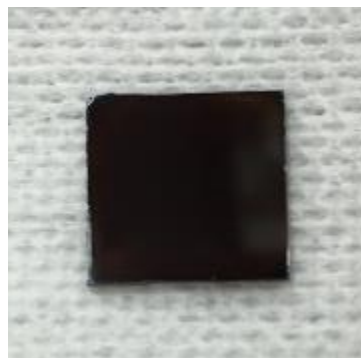
Figure 3.12. The photo of 9% excess PbI_2 perovskite film without annealing.

To gain insight into the photo-excited carrier recombination processes in the perovskite films, we conducted steady state and time-resolved photoluminescence (PL) measurements on the films with or without $PbAc_2$. **Figure 3.13a** shows the comparison of steady state PL spectra measured on the perovskite films with or without $PbAc_2$ in the precursor solution. The perovskite film added with $PbAc_2$ exhibits a higher PL intensity. Moreover, it has a blue-shifted PL peak from 769 to 764 nm, indicating the decreased density of traps states in the bandgap of the perovskite film [53]. Therefore, a small amount of $PbAc_2$ could significantly decrease trap density and suppress the non-radiative carrier recombination. Furthermore, the time-resolved PL spectra (**Figure 3.13b**) of the perovskite films were characterized. The PL decay is fitted by using a biexponential equation: $Y = A_1 exp(-t/\tau_1) + A_2 exp(-t/\tau_2)$.[79] It is notable that the carrier lifetimes in the perovskite film with $PbAc_2$ additive are efficiently prolonged. The carrier dynamics derived from the transient PL decay shows the information of carrier recombination related to defect densities. The short lifetime (τ_1) originates from the regions with high trap densities such as the film surface, and the long lifetime (τ_2) represents the carrier transportation in the region with less defects.[79, 123] Thus, the lifetimes (τ_1: 2.738 ns; τ_2: 16.089 ns) of $PbAc_2$ -added perovskite film longer than those of the normal perovskite film (τ_1: 1.948 ns; τ_2: 8.436 ns) imply lower defect densities in the former.
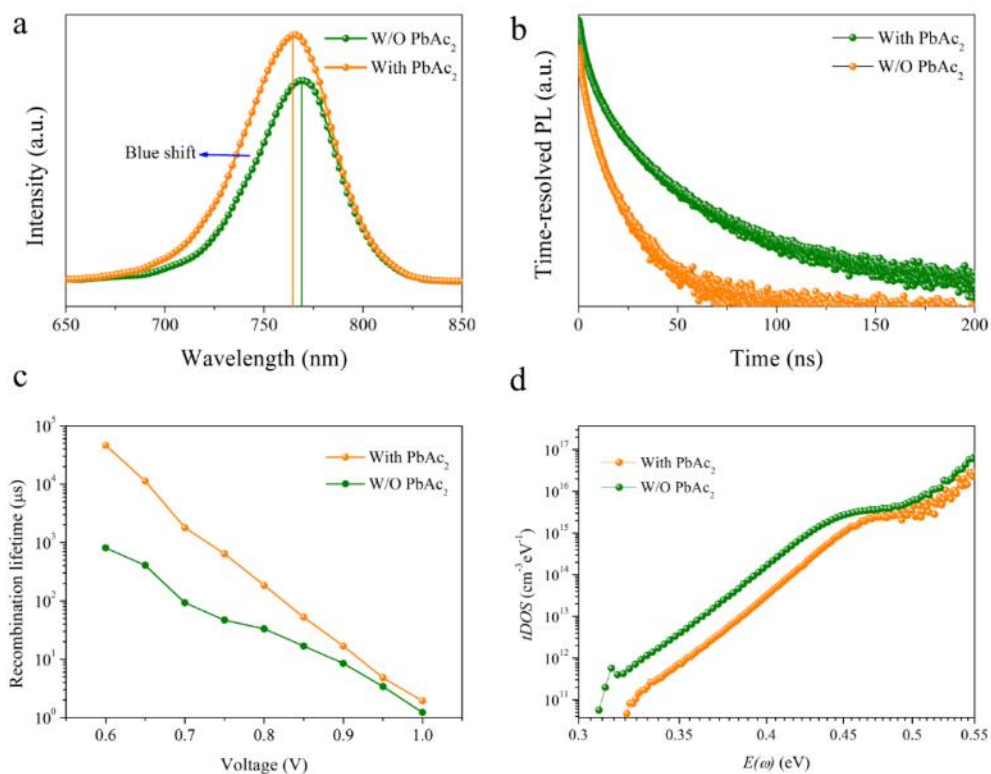
Figure 3.13. a) Steady state photoluminescence and b) time-resolved photoluminescence spectra of perovskite thin films deposited on glasses with and without $PbAc_2$ in the perovskite precursor. c) Carrier lifetimes at different bias obtained from impedance measurements on devices with or without $PbAc_2$. d) The trap density-of-states (tDOS) in PSCs with or without $PbAc_2$.
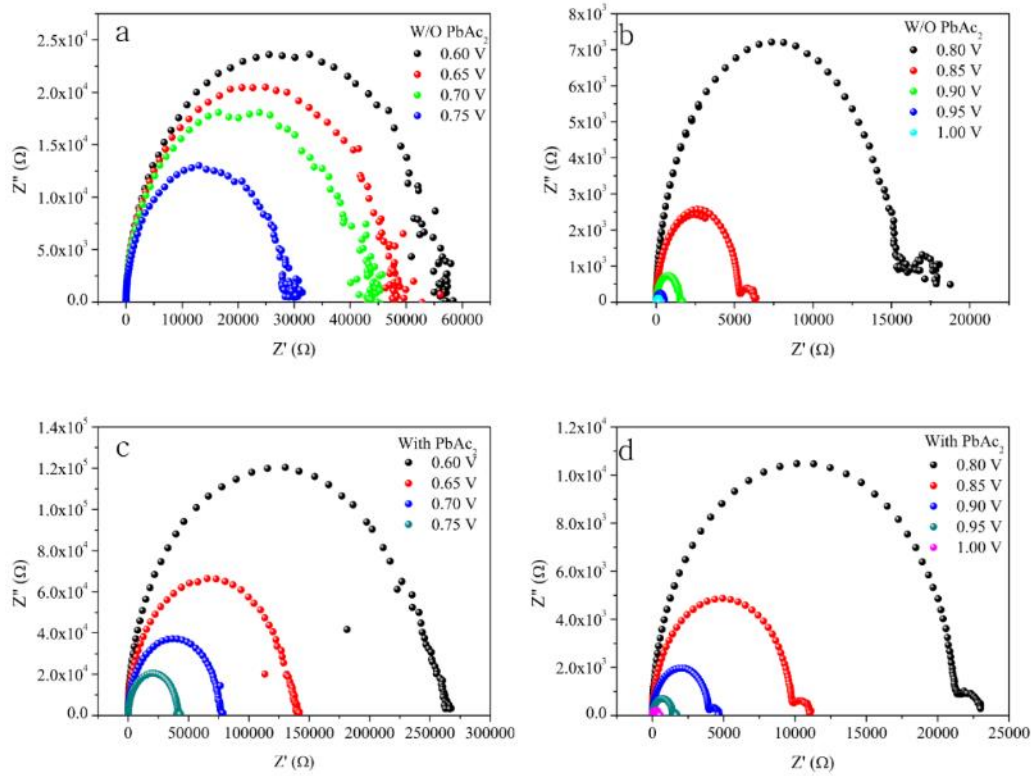
Figure 3.14. Impedance spectra of the devices with or without 3% PbAc$_2$ in the perovskite precursor solution.

Impedance analysis has been used as an effective approach for investigating the dynamics of charge carriers in PSCs. We have conducted impedance measurements on our devices to obtain further insight into the performance enhancement by PbAc$_2$. The typical impedance spectra (IS) of PSCs with or without PbAc$_2$ are shown in **Figure 3.14** in the supporting information. The carrier recombination lifetime in the PSCs can be extracted by fitting the IS data. **Figure 3.13c** demonstrates the recombination lifetimes of devices with or without the addition of PbAc$_2$. It can be observed that recombination lifetimes are significantly elongated by the addition of PbAc$_2$ due to the reduction of defects in the perovskite film. The density of trap states in the devices can directly be extracted from impedance spectra using the following equations.[67, 124-125]

$$C = -\frac{1}{\omega \times z^{''}} \qquad (1)$$

$$N_T = -\frac{V_{bi}}{qW}\frac{dC}{d\omega}\frac{\omega}{k_B T} \qquad (2)$$

$$E_\omega = k_B T ln(\frac{\omega_0}{\omega}) , \qquad (3)$$

where C is the capacitance of the device, ω the angular frequency, z'' the imaginary part of the the impedance, V_{bi} the build-in potential, W the depletion width, q the elementary charge, k_B the Boltzmann's constant, T is the temperature and ω_0 is the attempt-to-escape frequency ($\sim 10^{11}$/s). The relationship between capacitance (C) and frequency (f) is derived from the IS data (the applied bias voltage is 0.9 V) using equation (1). The defect density (N_T) at given temperature is proportional to $f \times dC/df$ according to the equation (2). The applied angular frequency ω defines an energetic demarcation by equation (3). As demonstrated in **Figure 3.13d**, the trap density-of-states (tDOS) with an energy level above 0.45 eV for the devices with and without PbAc$_2$ are very close. In comparison, for the energy levels below 0.45 eV, the tDOS of PbAc$_2$ -added device is lower than the control one by nearly one order of magnitude. These results indicate that the deep traps located at the surface of the perovskite films are almost unchanged due to the same passivation of PCBM. The densities of shallow traps inside the perovskite films induced by defects and grain boundaries are greatly decreased after the introduction of PbAc$_2$ due to the growth of larger grains.[67]

Furthermore, as shown in **Figure 3.15**, we investigated the stability of PSCs with or without PbAc$_2$ in precursors. The date was obtained from 10 devices for each condition and all devices were stored in N$_2$ gas without encapsulation. It is obvious that PSCs with the addition of PbAc$_2$ demonstrated much better stability than pristine ones. After stored for 20 days, PbAc$_2$ modified devices maintained about 95% of its initial average PCE, while the control devices retained only 80% of the original average efficiency. Besides, the efficiency deviation of reference devices increases greatly along with the degradation process. For the PSCs with the addition of PbAc$_2$,

there is smaller variation in the PCE deviation. It can be observed that the degradation of the reference ones mainly results from the rapid decrease of FF and J_{sc}, while the PSCs with $PbAc_2$ show much slower degradation rate. In the perovskite film, holes and grain boundaries are vulnerable to air due to their low crystallinity [57]. They are prone to absorb water in the air, which could accelerate the degradation process.   As shown in **Figure 3.6**, more holes and grain boundaries can be found in the control perovskite film than in the perovskite film with the addition of $PbAc_2$. Thus, the enhanced stability of PSCs induced by $PbAc_2$ are attributed to the pinhole-free perovskite films with larger grain sizes.
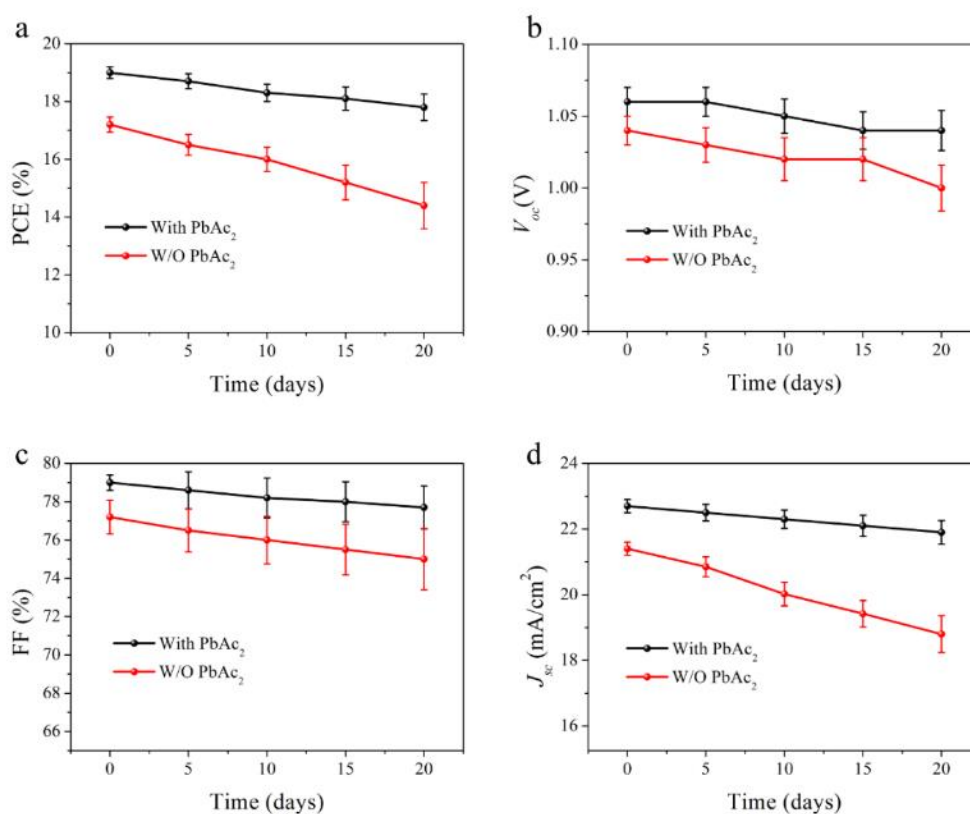
Figure 3.15. The comparison of the long-term stability of PSCs with 3% $PbAc_2$ additive in the precursor and control devices without $PbAc_2$. The photovoltaic parameters, including (a) *PCE*, (b) open circuit voltage (V_{oc}), (c) Fill factor (*FF*) and (d) short circuit current (J_{sc}) are characterized on ten devices for each condition.

3.4 Summary

In summary, we demonstrate the introduction of PbAc$_2$ into the perovskite precursor to control the perovskite crystallization process. The PbAc$_2$ additive serves as cross linking agent to form strong hydrogen bonding with MAI, leading to a more stable perovskite intermediate phase, and substantially retards the crystallization process of perovskite films. As a result, perovskite thin films with better morphology and larger grains are obtained by using this technique. Due to the high-quality perovskite films with low defect densities, the performance of PSCs is significantly improved in terms of the efficiency and stability. This work provides a novel approach for optimizing the performance of PSCs and other perovskite optoelectronic devices prepared by solution processes.

Chapter 4   Solution-phase   epitaxial growth of perovskite films on 2D material flakes for high-performance solar cells

The quality of perovskite films is critical to the performance of perovskite solar cells. However, it is challenging to control the crystallinity and orientation of solution-processed perovskite films. Here, we report solution-phase Van der Waals epitaxy growth of $MAPbI_3$ perovskite films on MoS_2 flakes for the first time. Under transmission electron microscopy, in-plane coupling between perovskite and MoS_2 crystal lattices is observed, leading to perovskite films with larger grain size, lower trap density and preferential growth orientation along (110) normal to the MoS_2 surface. In perovskite solar cells, when perovskite active layers are grown on MoS_2 flakes coated on hole transport layers, the power conversion efficiency is substantially enhanced for 15 % relatively due to the increased crystallinity of the perovskite layer and the improved hole extraction and transfer rate at the interface. This work paves a way for preparing high-performance perovskite solar cells and other optoelectronic devices by introducing two-dimensional materials as interfacial layers.

4.1   Introduction

Perovskite solar cells (PSCs) based on organic-inorganic halide perovskites have aroused much research interests for their great potential to be a new generation photovoltaic technology with low cost and high efficiency. Perovskite materials show superior optoelectronic properties, such as high light absorption coefficient, tunable bandgap, long carrier lifetime and diffusion length,[1, 6, 19, 34, 41, 71, 73, 76, 126-130] making them ideal candidate materials for not only solar cells but also light emission diodes

(LEDs), photodetectors and photocatalytic devices.[131-139] To achieve high-performance PSCs, high-quality perovskite films with large grain sizes and preferential orientations are needed. [140-142] Many strategies have been dedicated to improving the quality of perovskite films, such as solvent engineering, [143] employment of additives [144-146] and optimization of growing substrates. [147] Huang *et al*. demonstrated that substrates with non-wetting surface can enable the growth of perovskite films with large grain size and high crystallinity, which impressively suppresses the nonradiative recombination and improves the photovoltaic performance of PSCs. [147] Snaith *et al*. have used a self-assembled fullerene monolayer to grow high-quality perovskite films and passivate the defects on TiO_2 layers, leading to hysteresis-free PSCs with good photovoltaic performance. [148] Therefore, proper surface modification of substrates can decrease the density of nucleation sites and enlarge the grains of perovskite films. However, the orientation of the solution processed perovskite films cannot be conveniently controlled.

Van der Waals (vdW) epitaxy is a prevalent technique for preparing high-quality semiconductor films with preferential orientations on two-dimensional (2D) substrates with smooth and dangling-bond free surfaces. [149-152] The weak vdW interactions between the crystals and the substrates can enable epitaxial growth of the films with high crystallographic orientation and low defect states even in the presence of large lattice mismatch and symmetry misfit between them. [153-154] Recently, Duan et al. realized scalable solution-phase vdW epitaxial growth of cubic PbSe layer on 2D rhombohedral Bi_2Se_3 nanoplates. [155] Liu et al. also employed solution-phase vdW epitaxy strategy to fabricate ultra-thin graphdiyne film with high quality by using 2D graphene as a growing template. [156] Inspired by the intriguing effects, we consider that dangling-bond free 2D materials with proper lattice parameters can be utilized as growth templates for preparing high-quality perovskite films with a controllable

orientation.

Molybdenum disulfide (MoS_2) is a promising 2D material with high carrier mobilities and a suitable energy band structure for many optoelectronic applications. [157-159] Due to its dangling bond-free and clean surface, MoS_2 has been used as growth templates for preparing vdW epitaxial 2D materials. [160] In this chapter, solution processed large few-layer MoS_2 flakes have been employed as a growth template for perovskite films. We find for the first time the vdW epitaxial growth of $MAPbI_3$ perovskite on MoS_2 flakes, leading to highly oriented perovskite films with large grain sizes and low defect densities. TEM images demonstrate that (008) plane of $MAPbI_3$ and (110) plane of MoS_2 can match perfectly, which facilities the out-of-plane growth of perovskite films with preferential orientation along (110). Then MoS_2 flakes are modified on hole transport layers in inverted PSCs to improve the quality of the perovskite active layers. The power conversion efficiency (PCE) is boosted from 18.12% to 20.55% due to the significant increases of fill factor (FF), short current density (J_{sc}), and open circuit voltage (V_{oc}). This work provides a novel approach for preparing epitaxial perovskite films based on 2D material templates.

4.2   Devices fabrication and characterization

Liquid exfoliation of MoS_2 flakes: The MoS_2 flakes were prepared by the liquid exfoliation technique involving the ultrasound probe sonication of MoS_2 powder (Sigma) in IPA.[161-163] In detail, 100 mg of MoS_2 power was dispersed in 10 mL of IPA in a 20 mL centrifuge tube.   The dispersion was sonicated with a probe sonic tip (600 W) for 10 hours. The temperature of dispersion was kept around 278 K by immersing the tube in the ice bath. Then the dispersions were centrifuged at different rates to take the top two-thirds with different flake sizes.

Preparation of PSCs: ITO/glass substrates were sequentially washed with distilled water, acetone and isopropanol (IPA). Then, PTAA (Sigma) dissolved in toluene (2.0 mg/mL) was spin-coated on the ITO/glass substrates at a spin rate of 5000 rpm for 40 s. The films were subsequently annealed on a hotplate at 100 ℃ for 10 min. For the MoS_2 modified devices, the MoS_2 solution was spin-coated on the PTAA film and annealed at 100 ℃ for 10 min. The perovskite films were prepared by spin-coating the perovskite precursor solution containing CH_3NH_3I (Dyesol): 159 mg, PbI_2 (Alfa, 99.99%): 461 mg, DMF (Sigma, anhydrous, 99.9%): 600 mg, DMSO (Sigma, anhydrous, 99.9%): 78 mg, at 4000 rpm for 30 s. During the spin coating process, 0.5 ml of diethyl ether (Sigma, anhydrous, 99.7%) was slowly dripped on the rotating substrate in 10 secs after starting. All perovskite films were annealed at 100 ℃ for 20 min. Next, electron transport layers (ETLs) were prepared by spin coating a solution of PCBM (Nano-C) in chlorobenzene (20 mg/ml) at 3000 rpm for 40 s, followed by a thermal annealing at 90 ℃ for 20 min to crystalize PCBM. Bathocuproine (BCP, Sigma, 96%) dissolved in methanol (0.5 mg/ml) was spin-coated on the PCBM films at 4500 rpm for 30 s. Finally, devices were completed with the evaporation of silver (Ag) top electrodes through a shadow mask. The area of the PSC is designed to be 6 mm^2.

Material and device characterization: Scanning electron microscopy (SEM) images of MoS_2 and perovskite thin films were obtained under a Hitachi S-4300 microscope. The TEM images of MoS_2 and perovskite were conducted using JEOL JEM-2100F TEM/STEM operated at 200 kV. X-ray diffraction (XRD) measurement was performed using a Rigaku SmartLab X-ray Diffractometer operating at room temperature. Time-resolved photoluminescence (PL) measurements of the samples were carried out by using an Edinburgh FLSP920 fluorescence spectrophotometer. A 485-nm laser was used as an excitation light source.

The current density versus voltage (J-V) characteristics of the PSCs were measured by using a Keithley 2400 source meter under the illumination of an AM 1.5 solar simulator with a light intensity of 100 mW/cm^2 (Newport 91160, 300W). The light intensity was calibrated with a standard silicon solar cell. The external quantum efficiencies (EQEs) of the PSCs were measured with a standard test system, including a xenon lamp (Oriel 66,02, 300W), a Si detector (Oriel 76175_71580), a monochromator (Newport 66902) and a dual channel power meter (Newport 2931_C). The impedance characterization was performed by ZAHNER ENNIUM electrochemical workstation.

4.3   Results and discussion

MoS$_2$ flakes in isopropanol (IPA) were prepared by ultrasonicating bulk MoS$_2$ in IPA and separated by centrifuging the solution. [161] To study the growth of MAPbI$_3$ perovskite on MoS$_2$ surface, MoS$_2$ flakes were drop coated on a carbon-coated copper grid as shown in **Figure 4.1**. Then a precursor solution for MAPbI$_3$ was spin coated on the sample surfaces and solidified by an anti-solvent method, followed by thermal annealing at 100 °C for 20 min, which is similar to the preparation procedure of perovskite films in PSCs. [143] Next, the samples were characterized under transmission electron microscopy (TEM). **Figure 4.2a** shows the typical TEM image of the as synthesized heterostructure in which a MAPbI$_3$ perovskite film partially covers the surface of a MoS$_2$ flake. Figure 1b and c show the high-resolution TEM (HRTEM) images of MoS$_2$ and perovskite regions, respectively. The clear lattice fringes suggest the high quality of the MoS$_2$ flake and the perovskite grain. The plane with lattice distance of 1.58 Å is indexed to (110) plane for MoS$_2$. The plane with lattice distance of 3.16 Å is indexed to (004) plane for the perovskite grain. Figure 1d shows the selected-area electron diffraction (SAED) patterns of an overlapping area of

perovskite and MoS_2, which reveals the relative crystallographic orientation of the perovskite layer and MoS_2 crystal in the heterostructure. The SAED pattern gives two sets of diffraction spots with square (red) and hexagonal (yellow) symmetries, respectively. Each diffraction spot in the small and bigger hexagonal patterns corresponds to the (100) and (110) family planes of MoS_2 crystal, respectively. Each diffraction spot in the square pattern can be indexed to (004) family plane of the perovskite layer. It can be observed that the (008) plane overlaps the (110) plane of MoS_2, suggesting that the two planes have a perfect lattice match. Figure 1e and 1f show the SAED patterns of pure MoS_2 and perovskite for reference, respectively. This result clearly indicates the solution-phase vdW epitaxial growth of $MAPbI_3$ perovskite on the MoS_2 flake. This behavior has been observed on most of MoS_2 flakes on copper grid regardless of the sizes of perovskite grains as shown in **Figure 4.3**. This result also implies that $MAPbI_3$ crystals can nucleate with a higher possibility on MoS_2 surfaces than in the precursor presumably due to the relatively lower nucleation energy on MoS_2.
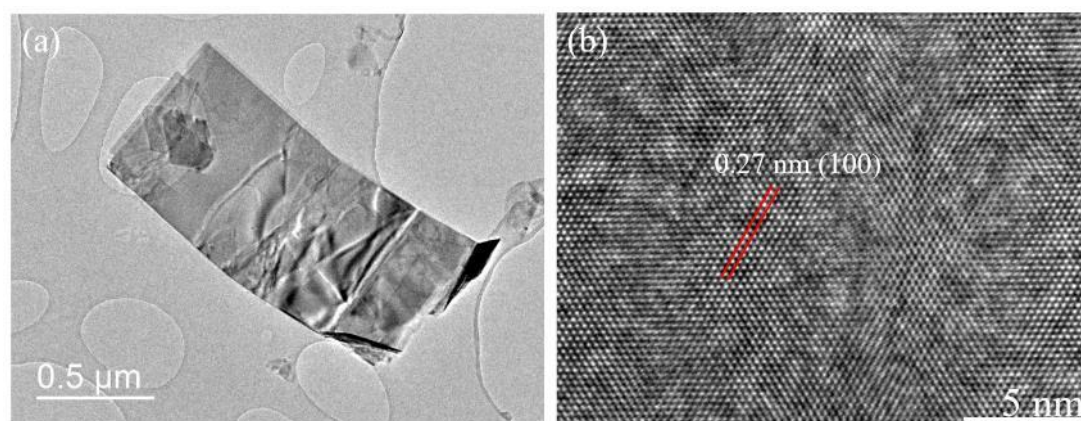
Figure 4.1. a) TEM image of a typical MoS_2 flake. b) The high resolution TEM image of a representative MoS_2 flake.
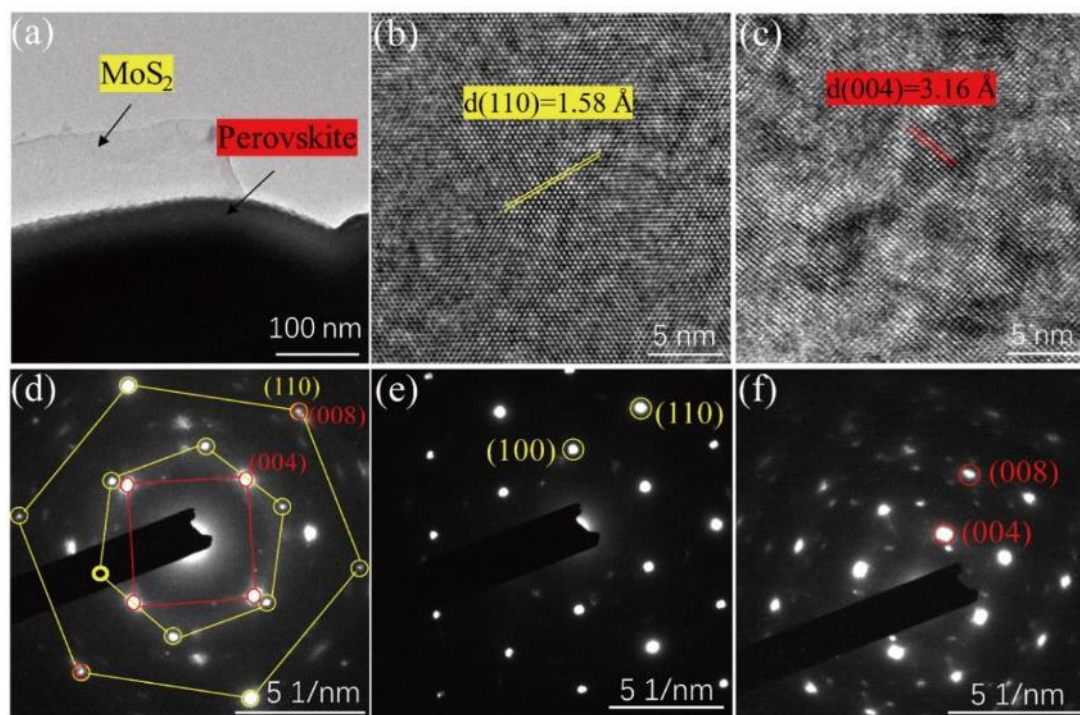
Figure 4.2. (a) Top-view TEM image of MoS_2 with a $MAPbI_3$ perovskite layer grown on its surface. (b-c) HRTEM images of MoS_2 and perovskite, respectively. (d) The SAED pattern of perovskite/MoS_2 region. Two separate diffraction spots are observed. The yellow one is for MoS_2. The red one is for perovskite. (e-f) The SAED patterns of MoS_2 and perovskite for reference, respectively.
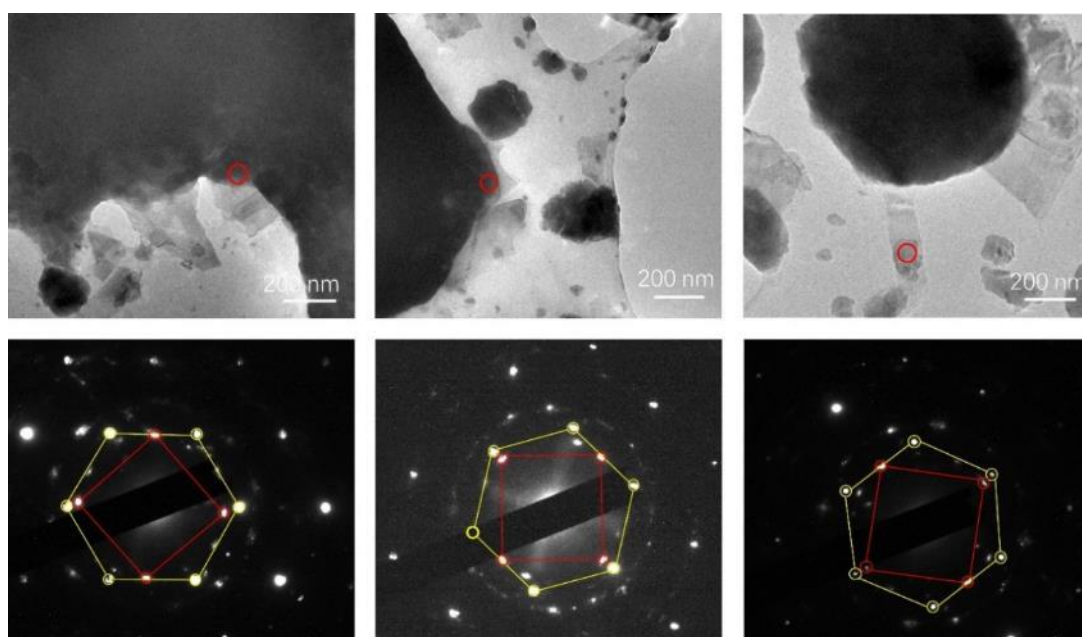
Figure 4.3. The SAED patterns of perovskite/MoS_2 region from three independent

samples. The upper are the TEM images of selected area of $MAPbI_3/MoS_2$ heterojunctions. The under are the corresponding SAED patterns.

Based on the electron diffraction analysis, the crystal structures of perovskite and MoS_2 as well as the relative orientation are illustrated in **Figure 4.4a-c.** Figure 4.3a shows the side view of the heterojunction of $MAPbI_3$ and MoS_2 along $(\bar{1}10)$ direction of $MAPbI_3$ and $(\bar{1}00)$ direction of MoS_2. **Figure 4.4b** and **c** demonstrate top views of MoS_2 along (001) direction and $MAPbI_3$ along (110) direction in the heterojunction, respectively. According to literature, [164] the interplane distances of $MAPbI_3$ (008) and MoS_2 (110) planes have an identical value of 1.58 Å, which are perfect for the epitaxial growth of $MAPbI_3$ on MoS_2. On the other hand, the dangling bond-free surface of MoS_2 flake is favorable for vdW epitaxial growth of the perovskite layer although the lattice symmetries of MoS_2 (hexagonal) and $MAPbI_3$ (tetragonal) are different. [155] So the in-plane coupling between MoS_2 and $MAPbI_3$ can enable the growth of $MAPbI_3$ grains on the surface of MoS_2 templates, leading to the out-of-plane orientation of the perovskite layers along (110). The growth process is schematically presented in **Figure 4.4d.** The dangling bond-free surface of MoS_2 can facilitate the migration of atoms and accelerate the growth of perovskite grains along lateral direction, leading to the enlargement of perovskite grain size. [165]
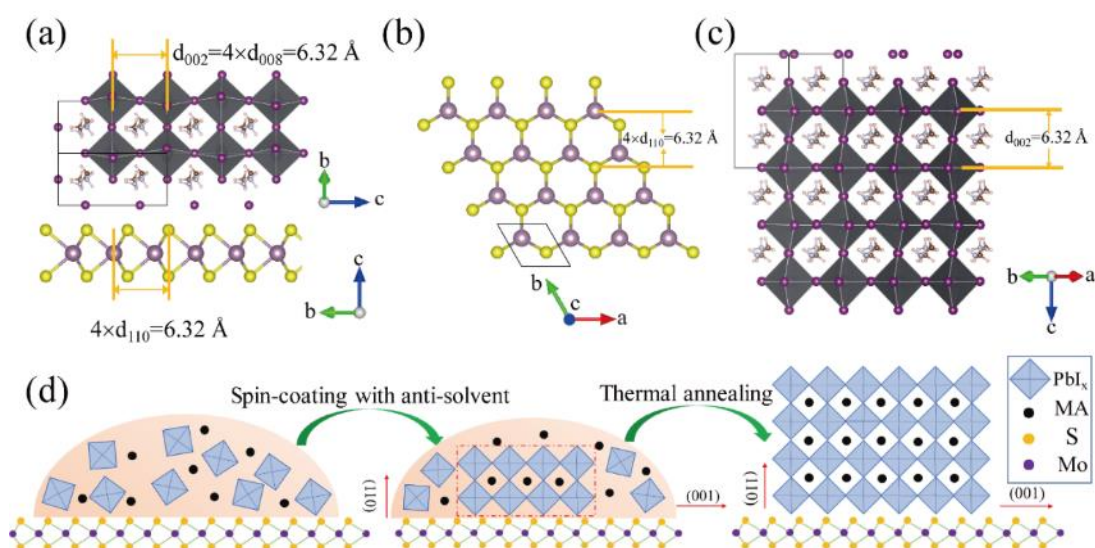
Figure 4.4. (a) The side view of atomic crystal heterojunction of MAPbI$_3$ and MoS$_2$. Atomic crystal structure of (b) (001) plane of MoS$_2$ and (c) (110) plane of perovskite. (d) Schematic diagram of the vdW epitaxial growth of a MAPbI$_3$ grain on a MoS$_2$ surface.

To use the MoS$_2$ flakes in PSCs, we coated them on the surface of hole transport material (HTM) poly[bis(4-phenyl)(2,4,6-trimethylphenyl)amine] (PTAA) by spin coating.[146] By adjusting the centrifugation rate during the preparation process, MoS$_2$ flakes with different average sizes can be obtained. As shown in **Figure 4.5a-d**, the PTAA and the modification of MoS$_2$ flakes were observed under scanning electron microscopy (SEM). The average sizes of MoS$_2$ flakes are 90, 250 and 500 nm at centrifugation rates of 8000, 4000, 2000 rpm, respectively as shown in **Figure 4.6**. Due to the limitation of liquid exfoliation method, the largest average size of MoS$_2$ flakes obtained by us is around 500 nm. [161]
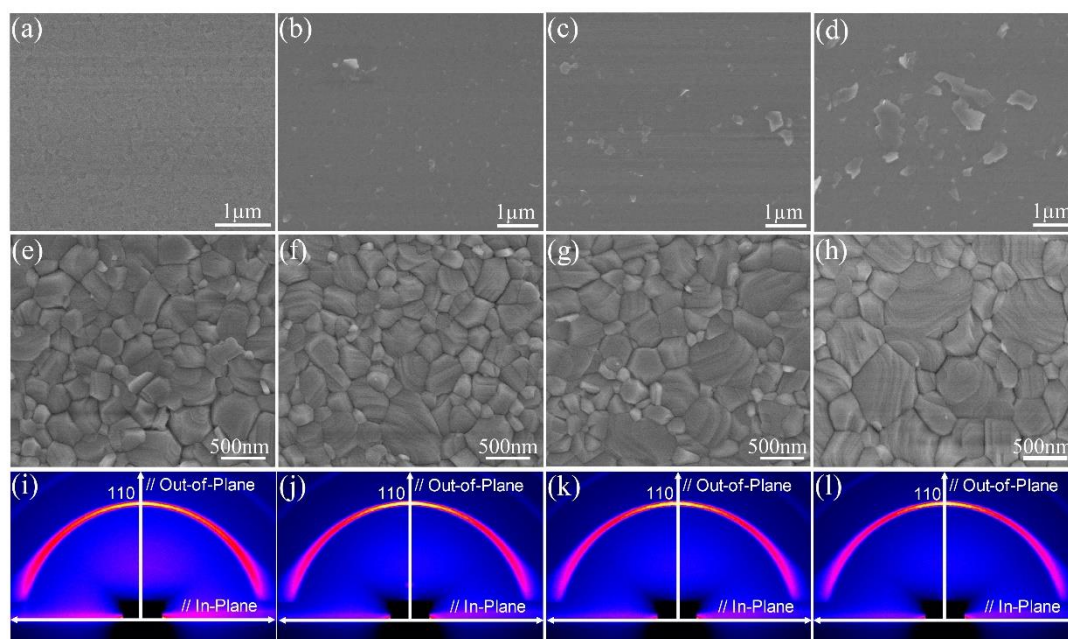
Figure 4.5. Top-view scanning electron microscopy (SEM) images of (a) PTAA film, and PTAA films modified with MoS$_2$ falkes processed with contrifugation rate of (b) 8000 r.p.m, (c) 4000 r.p.m and (d) 2000 r.p.m. SEM images of perovskite films deposited on (e) PTAA, and PTAA films modified with MoS$_2$ falkes processed with contrifugation rate of (f) 8000 r.p.m, (g) 4000 r.p.m and (h) 2000 r.p.m, respectively. (i-l) 2D GIWAXS patterns for the corresponding perovskite films shown in (e-h).
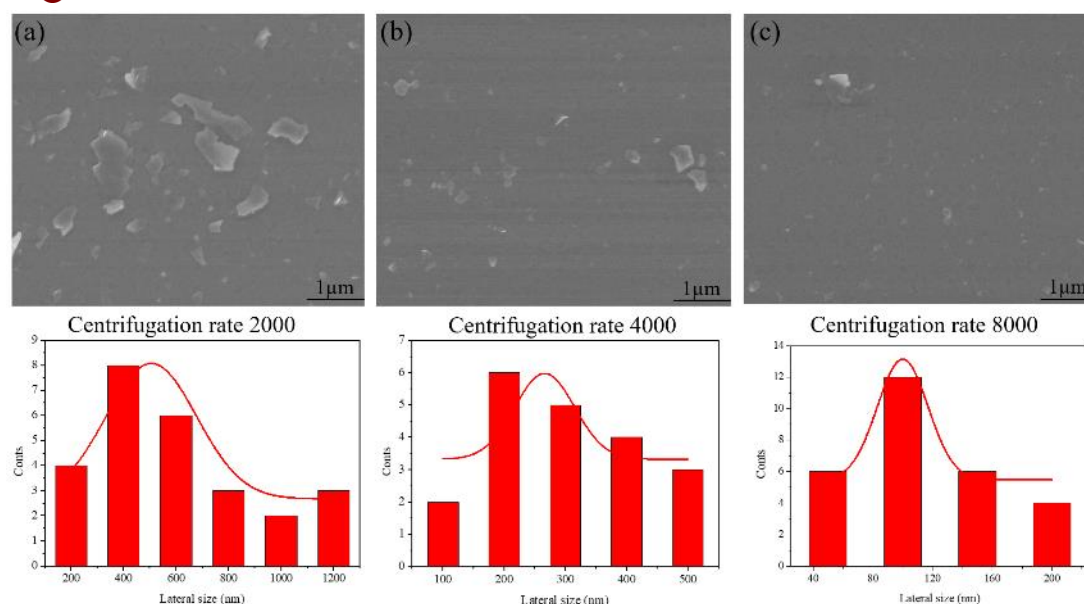
Figure 4.6. The SEM images of PTAA with MoS$_2$ processed with different centrifugation rate and the corresponding size distribution statistics.

Next, MAPbI$_3$ perovskite films were coated on the MoS$_2$-modified PTAA films by the standard antisolvent method. [143] As shown in **Figure 4.6e-h,** the average grain size of the perovskite films increases with the increase of MoS$_2$ flake size and the average size of 526 nm could be obtained when 500 nm MoS$_2$ flakes were introduced as shown in **Figure 4.7**. Grazing incidence wide angle X-ray scattering (GIWAXS) measurements were then conducted on the corresponding perovskite films to study the effect of MoS$_2$ flakes on the perovskite crystallinity. **Figure 4.5 i-l** show the 2D GIWAXS patterns of perovskite films, which demonstrate the scattering rings at $q=1$ Å^{-1}, indexed to the (110) plane of MAPbI$_3$ perovskite. The intensity distribution range around the azimuthal angle of 90° is narrower for bigger MoS$_2$ flakes, indicating an improved orientation of the resultant perovskite films as shown in **Figure 4.8**. X-ray diffraction (XRD) measurements were also employed to investigate the crystal structure of perovskite films. The ratio between the intensities of the (110) and (310) peaks increases with the increase of MoS$_2$ size as shown in **Figure 4.9**, which suggests the preferential orientation along (110) direction for the perovskite film on MoS$_2$ flakes. These results can be attributed to the vdW epitaxial growth of perovskite grains

on MoS_2 surface. Due to the limited sizes of MoS_2 templates, it is reasonable to find that bigger perovskite grains can be obtained on bigger MoS_2 flakes, which will be important for the performance of PSCs. [166-167] For the pure PTAA layer, the rough surface would restrict the lateral growth of perovskite grains. Therefore, the control samples show the smallest grain size.
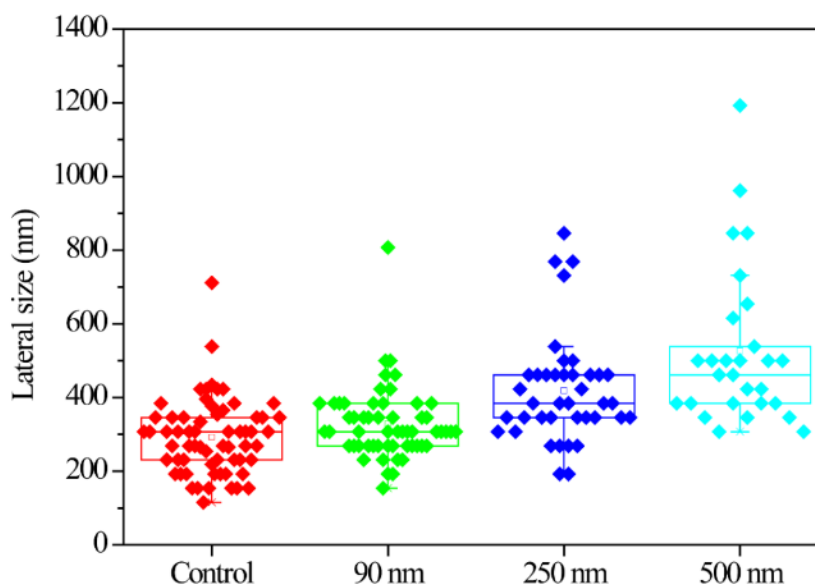
Figure 4.7. The grain size distribution of control perovskite film and perovskite films grown on MoS_2 with different sizes. For the control film, the average size is 290 nm. For the films grown on MoS_2 with size of 90, 250 and 500 nm, the corresponding average grain sizes are 328, 419 and 526 nm, respectively.
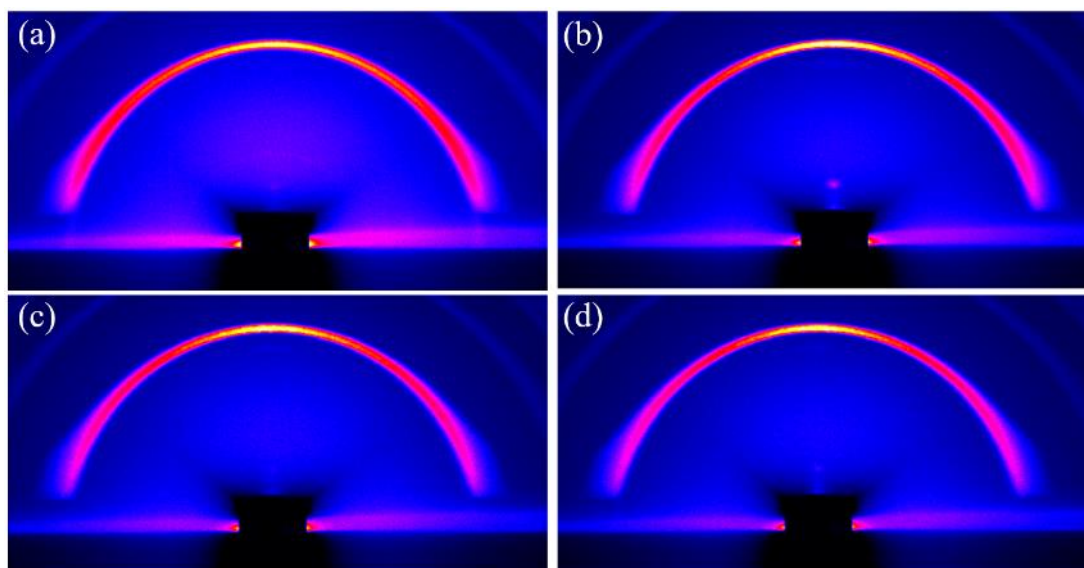
Figure. 4.8. The 2D GIWAXS patterns for the perovskite films deposited on a) PTAA and PTAA films modified with MoS_2 flakes processed with centrifugation rate of b) 8000 r.p.m, c) 4000 r.p.m and d) 2000 r.p.m, respectively.
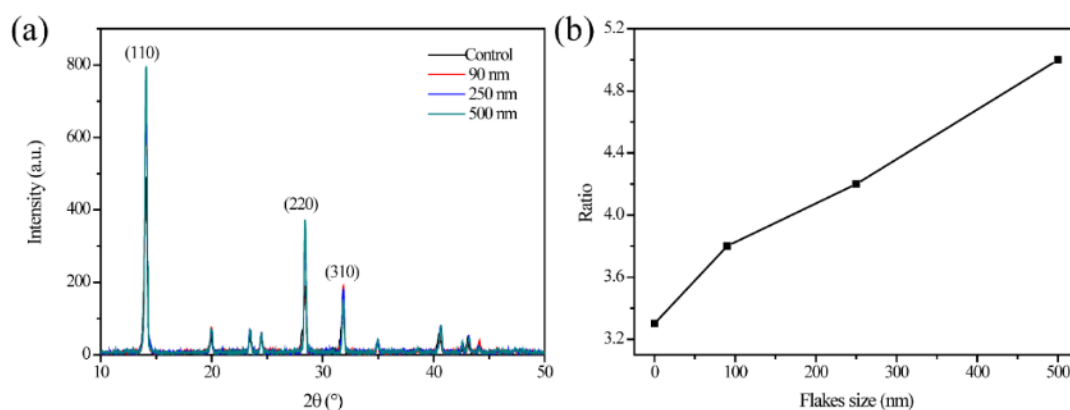
Figure 4.9. a) The X-ray diffraction patterns and b) the ratio between the intensities of (110) and (310) peaks of perovskite films deposited on MoS_2 flakes with different sizes.

To quantitatively assess the impact of MoS_2 on the density of defects in the grown perovskite films, hole-only devices with the structure of ITO/PTAA/MoS_2/Perovskite/Au are fabricated.[146] **Figure 4.10a** and **b** show the *J-V* curves of the devices with and without MoS_2, respectively. The trap-state density could be determined by the trap-filled limit voltage (V_{TFL}) according to the equation:

[15, 168-170]

$$N_{defects} = 2\varepsilon_r\varepsilon_0 V_{TFL}/eL^2 \qquad (1)$$

where L is the thickness of the perovskite film, ε_r and ε_0 are the relative dielectric constant of MAPbI$_3$ and the vacuum dielectric permittivity, respectively, and e is the elementary charge. The calculated defect densities ($N_{defects}$) are 1.17×10^{16} cm^{-3} and 2.59×10^{16} cm^{-3} for the devices with and without MoS$_2$, respectively. The lower defect density in the former could be attributed to the increased crystallinity and more consistent orientation of perovskite grains growing on MoS$_2$ flakes.
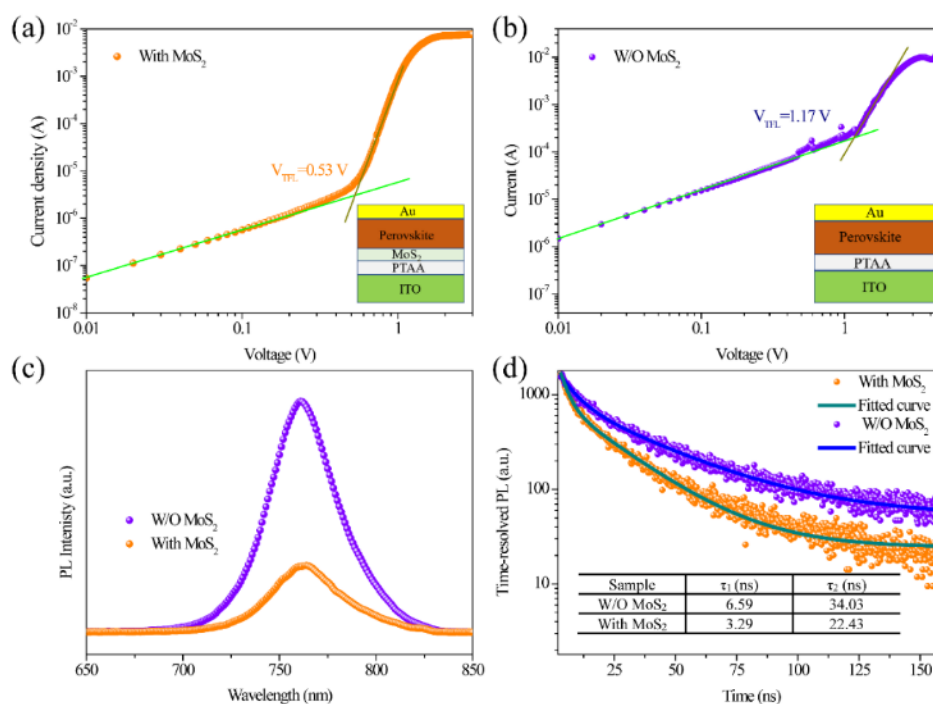
Figure 4.10. Current density-voltage characteristics of hole only devices (a) with and (b) without a MoS$_2$ interlayer. (c) Steady state photoluminescence and (d) time-resolved photoluminescence spectra of perovskite thin films deposited on PTAA with and without MoS$_2$.

To gain insight into the effect of MoS$_2$ interfacial layer on the hole transfer process between perovskite and HTM, the steady state and time-resolved photoluminescence

(PL) measurements were conducted on the perovskite films deposited on PTAA and MoS$_2$/PTAA surfaces. **Figure 4.10c** shows the steady state PL spectra of two perovskite films, in which the PL peak on MoS$_2$/PTAA is much lower than that on pure PTAA. This result suggests that the holes generated in a perovskite film could be extracted more efficiently with the help of MoS$_2$ modification, which would facilitate the charge transfer in PSCs. Furthermore, time-resolved PL spectra (**Figure 4.10d**) of the two perovskite films were characterized. The PL decay is fitted by using a biexponential equation: $Y = A_1exp(-t/\tau_1) + A_2exp(-t/\tau_2)$, yielding a fast decay (τ_1) component and a relatively slow decay (τ_2) component. The decay process within tens of nanoseconds is the result of the quenching of charge carriers by the charge transport layers. [5, 171] It can be observed that the first decay lifetime is shortened from 6.59 to 3.29 ns due to the effect of MoS$_2$ interface. The second decay lifetime is also decreased from 34.03 ns to 22.43 ns. So the introduction of MoS$_2$ induces a faster charge transfer rate from perovskite to HTM.

PSCs with an inverted structure of glass/ITO/PTAA/MoS$_2$/perovskite/PCBM/BCP/Ag shown in **Figure 4.11a** were then prepared by the antisolvent method. MoS$_2$ flakes with different sizes were modified on the PTAA layers of the devices. Ultraviolet photoelectron spectroscopy (UPS) measurements were conducted on PTAA and PTAA/MoS$_2$ films to decide their band structure as shown in **Figure 4.12**. According to the UPS results, the highest occupied molecular orbital (HOMO) level of PTAA is -5.01 eV and the valence band maximum (VBM) of MoS$_2$ flakes is -5.16 eV. According to the absorption spectrum of the MoS$_2$ flakes, the bandgap is about 1.7eV and thus the conduction band minimum (CBM) is -3.46 eV. The band structure of the device is presented in **Figure 4.12b**, in which other energy levels are taken from literature. [128] Notably, a cascade band structure is formed in the PTAA/MoS$_2$/perovskite/PCBM multilayer, which is favorable for

charge transfer in the PSCs. **Figure 4.12c** shows the device statistics of PCEs of 10 control devices and 10 devices modified by MoS_2 flakes with different average sizes, including 90, 250, 500 nm. The corresponding average PCEs are 17.17 ± 0.76 %, 18.41 ± 0.37 %, 19.28 ± 0.27 % and 19.84 ± 0.42 %, respectively. So the PCEs of the devices increase with the increase of MoS_2 flake size and the biggest relatively enhancement is 15.55% (from 17.17% to 19.84%) as shown in **Figure 4.13** and **Table 4.1**.
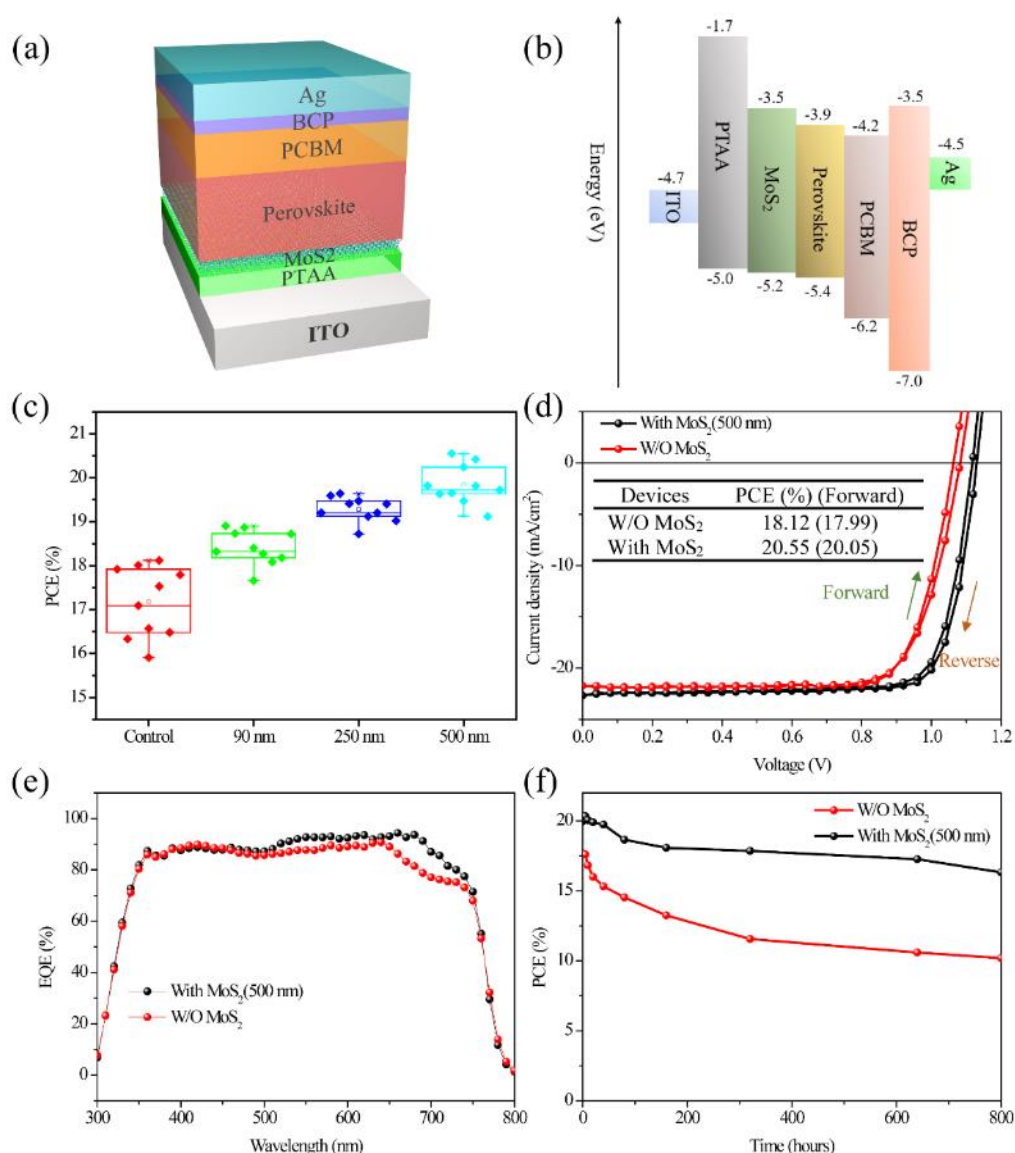
Figure 4.11. (a) Schematic diagram of an inverted planar PSC. (b) Energy band structure of the PSC with a MoS_2 interlayer. (c) The statistics of PCEs of 10 devices

for each fabrication condition. (d) J-V curves and (e) EQE curves of PSCs with and without MoS₂ modification in the device fabrication. (f) Long term stability for devices with and without MoS₂ stored in the dark ambient with a relative humidity of 30 % without encapsulation.
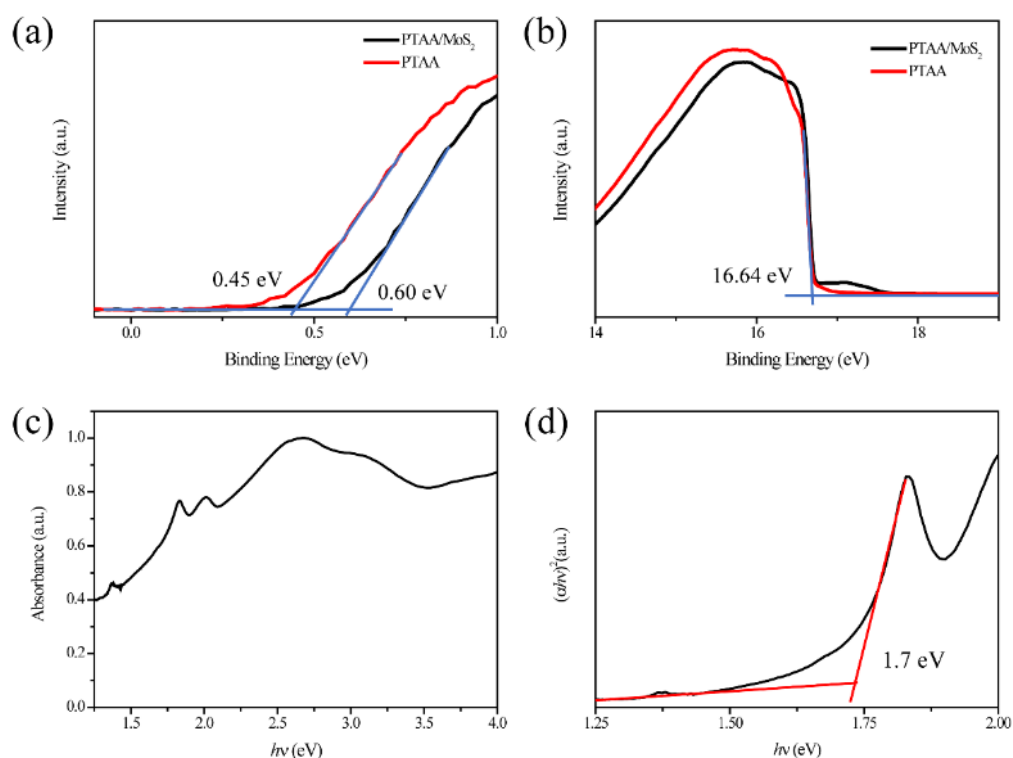
Figure 4.12. a) Near EF region and b) cutoff region of the UPS spectra of PTAA and PTAA/MoS₂ films. c) The absorbance of MoS₂ flakes solution. d) The Tauc plot of MoS₂ flakes.
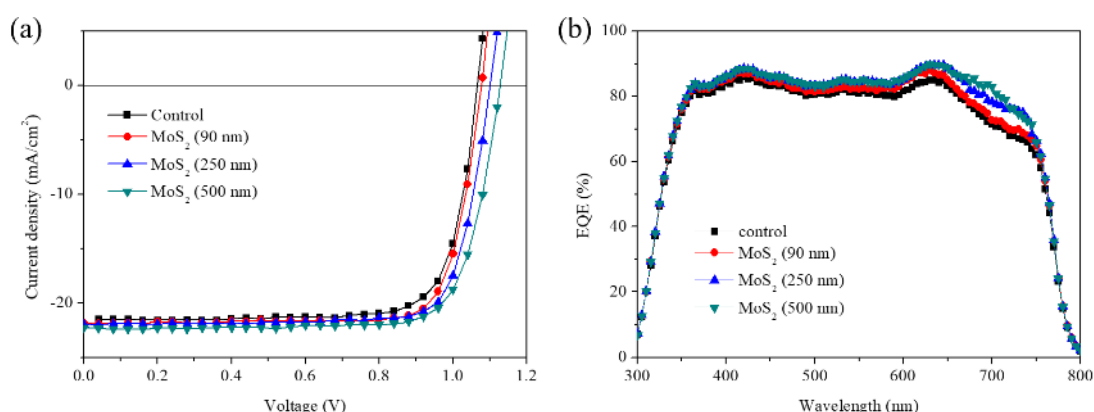
Figure 4.13. a) The J-V and b) EQE curves of PSCs without and with MoS₂ flakes of different sizes. The calculated J_{sc} of the control device and the devices based on MoS₂ flakes with sizes of 90, 250, and 500 nm are 19.73, 20.18, 20.80 and 20.90

mA/cm^2, respectively.

Table 4.1. The photovoltaic parameters of PSCs without and with MoS_2 flakes of different sizes.

Devices	V_{oc} (V)	J_{sc} (mA/cm^2)	*FF* (%)	*PCE* (%)
control	1.06	21.61	77.94	17.92
90 nm	1.08	21.85	80.19	18.87
250 nm	1.10	21.92	79.29	19.12
500 nm	1.13	22.29	78.18	19.64

Figure 4.11d shows the photocurrent density - voltage (*J-V*) curves of PSCs with and without a MoS_2 interlayer. The device without MoS_2 has a PCE of 18.12 (17.99) %, an open circuit voltage (V_{oc}) of 1.08 (1.06) V, a short-circuit current density (J_{sc}) of 21.72 (21.72) mA/cm^2 and a fill factor (FF) of 77.52 (78.14) % measured under reverse (forward) voltage scan. When MoS_2 (size: 500 nm) is introduced into the devices, the photovoltaic performance is enhanced significantly to a PCE of 20.55 (20.05) %, a V_{oc} of 1.13 (1.12 V) V, a J_{sc} of 22.66 (22.66) mA/cm^2 and a FF of 80.26 (79.00) %. This efficiency is one of the highest values for $MAPbI_3$ -based PSCs with inverted structures as shown in **Table 4.2**. The larger V_{oc} can be attributed to the higher quality perovskite layer with larger grain sizes and lower defect densities. The higher FF and J_{sc} could be resulted from the enhanced carrier transfer rate between perovskite and PTAA by the modification of MoS_2 and more efficient carrier transport in the vertical direction due to the highly oriented perovskite films. **Figure 4.11e** shows the external quantum efficiency (EQE) spectra of the devices with and without MoS_2 modification. The corresponding integrated current densities are 21.82 mA/cm^2 and 20.86 mA/cm^2, respectively, which are close to the results of *J-V* measurements.

Table 4.2. The list of inverted PSCs based on PTAA layer and $MAPbI_3$ perovskite with efficiency over 20 % reported in literatures.

Device structure	V_{oc} (V)	J_{sc} (mA/cm^2)	FF (%)	PCE (%)	Reference
ITO/PEDOT:PSS/MAPbI$_3$/C60/BCP/Ag	1.06	23.10	86.00	21.00	[172]
ITO/PTAA/MAPbI$_3$/PCBM/BCP/Ag	1.13	22.66	80.26	20.55	This work
FTO/NiO$_x$/MAPbI$_{3-x}$Cl$_x$/PC$_{61}$BM/ZrAcac/Al	-	-	-	20.50	[173]
ITO/PTAA/MAPbI$_3$/PCBM/C60/BCP/Ag	1.11	22.50	81.60	20.40	[174]
ITO/NiO$_x$/MAPbI$_3$/PCBM/BCP/Ag	-	-	-	20.20	[175]
ITO/PTAA/MAPbI$_3$/PCBM/Bphen/Al	1.114	23.52	76.80	20.11	[176]
ITO/PEDOT:PSS/MAPbI$_3$/C60/BCP/Ag	1.03	23.51	83.00	20.10	[177]

The cross-section SEM images of corresponding perovskite films exhibit that the introduction of MoS$_2$ did not increase the thickness (~400 nm) of the perovskite film as shown in **Figure 4.14**. Therefore, the improvement of J$_{sc}$ should be attributed to the improved quality of the perovskite film and more efficient carrier transfer rate. Moreover, stabilized power output (SPO) curves were recorded on the champion devices as shown in **Figure 4.15**. The PCE of the champion device with MoS$_2$ modification stabilizes at about 20.0% while the control device shows a stabilized PCE of only 17.55%. This result further confirms the positive effect of MoS$_2$ on the enhancement of PSC performance. Although MoS$_2$ has been introduced in PSCs as an interlayer previously by George et al., [178] the vdW epitaxial growth of perovskite grains on MoS$_2$ has not been observed by them presumably due to their different fabrication method of the perovskite layer (two-step deposition). More importantly, our devices show much higher PCEs than their devices due to the successful vdW epitaxial growth of the perovskite films on big MoS$_2$ flakes by our one-step antisolvent method.
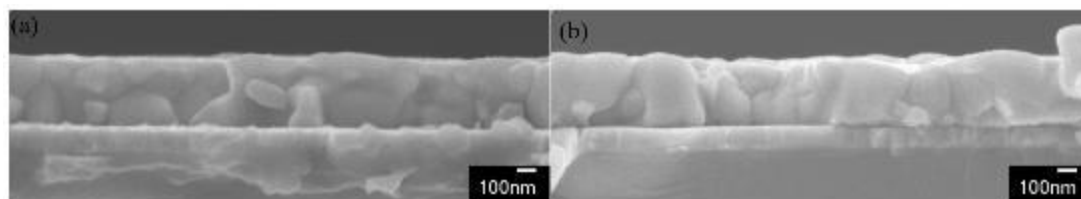
Figure 4.14. Cross-section SEM images of perovskite films grown on PTAA a) and PTAA with MoS$_2$ modification b).
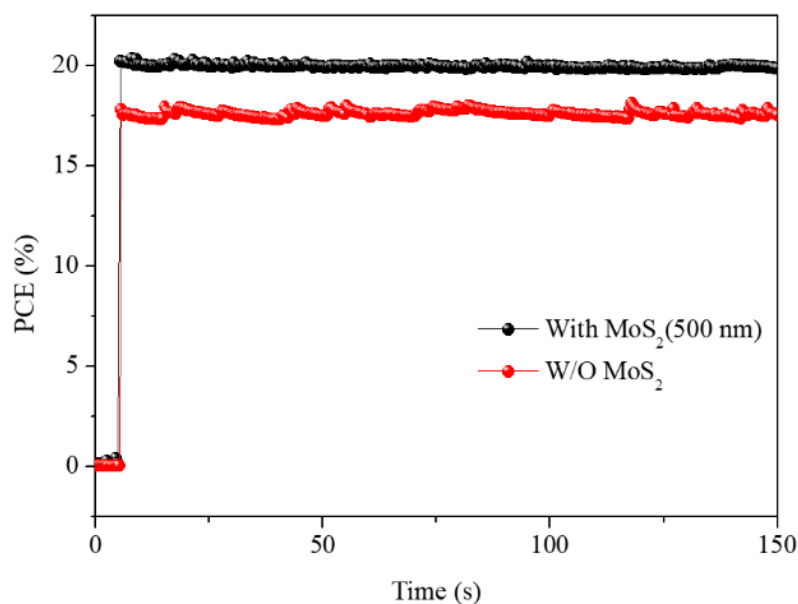
Figure 4.15. The stable power outputs for PSCs with and without MoS$_2$ modification.

The stability of PSCs is closely related to the interface properties of the devices. [179] **Figure 4.11f** shows the PCEs of the devices as functions of storage time. After 800 hours, the PCE of the control device drops for about 40 % of its initial value, while the MoS$_2$ -modified device drops only 20% relatively. Therefore, the modification of MoS$_2$ can greatly enhance the stability of the devices. To better understand the degradation mechanism, the two devices were characterized by impedance analyzer. Nyquist plots of the devices before and after the 800 hours aging tests were obtained, which can be fitted with an equivalent circuit model as shown in **Figure 4.16**.[180]
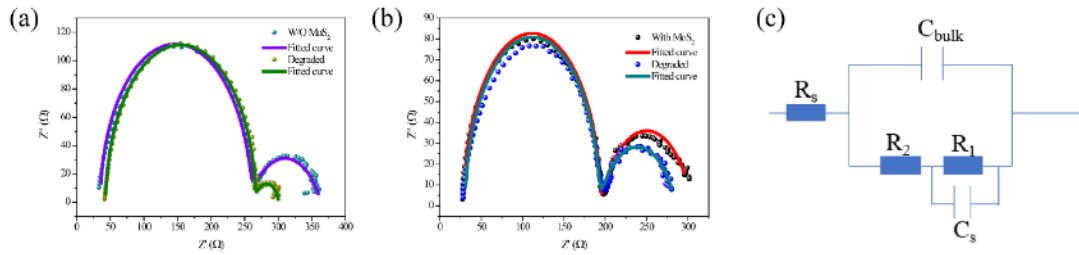
Figure 4.16. Impedance spectra of the devices a) without and b) with MoS_2 modification before and after 800 hours of aging characterized under simulated solar light (100mW/cm^2) and a bias voltage of 0.8V. c) The simplified equivalent circuit model for fitting the impedance spectra.

The semicircle in the high frequency region is assigned to be the capacitance (C_{bulk}) of the perovskite bulk. [180] Under different light intensity and bias voltage, we found that C_{bulk} has little change and is around 10^{-7} F/cm^{-2}. Assuming that $C_{bulk} = \frac{\varepsilon_0 \varepsilon_r}{L}$, the relative dielectric constant ε_r is estimated to be around 45, which is a reasonable value for the perovksite layer. So C_{bulk} is the dielectric capacitance of the perovskite layer, which is not related to carrier recombination. The semicircle in the low frequency region can be assigned to be the recombination resistance (R_1) and capacitance (C_s) at interfaces because it was reported to be directly related to the carrier recombination at the interfaces.[180] For the control device, R_1 is decreased from 121 to 32 Ω whereas R_2 is unchanged. For the MoS_2 -modified device, R_1 is slightly decreased from 112 to 93 Ω and R_2 has little change. Considering that both devices have the same PCBM/perovksite interface, the big decrease of R_1 in the control device can be attributed to the degradation of the PTAA/perovskite interface, which is presumably due to the charge accumulation inside it. By introducing a MoS_2 layer into the devices, the interface degradation can be significantly alleviated due to more efficient charge transfer across the MoS_2 layer, which is consistent with the PL results.[162] Thus, the incorporation of MoS_2 interfacial layer into the PSCs can efficiently improve the long-term stability of the PSCs.

4.3 Summary

In summary, we demonstrate the vdW epitaxial growth of MAPbI$_3$ perovskite on MoS$_2$ flakes by a one-step antisolvent method for the first time. High-quality perovskite films with large grain sizes and highly preferential orientation on MoS$_2$ interlayers have been obtained in PSCs, leading to high PCEs as well as good stability of the devices. Considering that 2D materials with different crystal structures are readily available, we can realize vdW epitaxial growth of perovskite films with different compositions by choosing suitable 2D material templates and achieve different types of PSCs with high-performance. This work paves a way for preparing epitaxial perovskite films by a convenient solution process, which will be useful in preparing not only PSCs but also other types of perovskite optoelectronic devices.

Chapter 5   Intrinsically flexible hybrid perovskites for high-performance solar cells by introducing van der Waals interaction at grain boundaries

Flexible perovskite solar cells (FPSCs) are highly desirable due to the facile mass-production and diverse wearable applications. As the light absorber, the bending stability of perovskite films under operation is critical for the photovoltaic performance. However, the polycrystalline perovskite films have a mass of defects at the grain boundaries, which serve as stress concentrators that promote propagation of cracks under bending operation, leading to degradation. Herein, we report that van der Waals interactions are introduced into the grain boundaries of $MAPbI_3$ films to release strains by incorporating 2D perovskite (PEA_2PbI_4). The applied strain under operation could be released by the recoverable sliding or rotating between interlayers of 2D perovskite. The intrinsic bendability and deformability of perovskite films are significantly improved. Besides, due to the defect passivation, the efficiencies of perovskite solar cells based on flexible and glass substrates are boosted to 19.55% and 20.97%, respectively. This work provides a new research direction to fabricate flexible perovskite solar cells with high bendability and efficiency.

5.1   Introduction

As the most promising candidate for next-generation photovoltaic technology, perovskite solar cells (PSCs) have attracted tremendous attentions from both academic and industrial fields. The highest certified power conversion efficiency

(PCE) of PSCs is boosted to 24.2 % due to the intriguing optoelectronic properties of perovskite materials, such as high light absorption coefficient, desirable bandgap and long charge diffusion length [1, 181-182]. In addition to the high efficiency, the relatively low cost of material and device fabrication enables the mass-production and commercialization of PSCs in the near future. Flexible perovskite solar cells (FPSCs) are supposed to be the foremost commercialization option due to the facile mass-production by the roll to roll printing process, which can further decrease the cost substantially [183]. Furthermore, the development of FPSCs can fulfill the highly diverse applications, such as wearable and portable electronics, unmanned systems, smart buildings and aerospace applications [3-5]. Thus, the fabrication of lightweight FPSCs with high efficiency and mechanical robustness is of great significance for the development and commercialization of perovskite photovoltaic technology. To date, many efforts are dedicated to fabricating novel FPSCs with high efficiency and superior bending durability. Various strategies are employed to improve the quality of perovskite films deposited on flexible substrates to enhance the photovoltaic performance of FPSCs, such as tailoring the precursor composition [43], optimizing transporting layers, and introduction of additives in the perovskite precursors [19, 44-45]. Wu et al. reported $FAPbI_3$ flexible solar cells with a record efficiency of 19.38% by using $FAI·PbI_2·NMP+x\%MACl$ as the precursor [46]. This efficiency is comparable with that of rigid PSCs, which suggests that the efficiency is not the limiting factor hindering the commercialization of FPSCs. Bending durability of devices is another critical property to evaluate the performance and applications of FPSCs. Most of the current works are focused on exploring flexible transparent substrates with thin thickness and highly flexible electrodes with high transmittance and conductivity, such as polyethylene terephthalate (PET), polyethylene naphthalate (PEN), polyimide (PI) and metallic foils for flexible substrates and PEDOT:PSS, Ag mesh, carbon nanotubes and graphene for electrodes, to improve the flexibility and bendability of

FPSCs [128, 184]. The lightest FPSCs based on PET substrate with thickness of 1.4 μm have a record specific weight of 23 W g^{-1}, which ravels all other photovoltaic technology including copper indium gallium selenide, cadmium telluride (CdTe), organic photovoltaics (OPVs), and commercial large area module product of nanocrystalline silicon [185-187]. This indicates the great advantage of FPSCs as flexible photovoltaic devices. The mechanical property of perovskite films as photoactive materials is equally vital for the flexibility of FPSCs. As the increasing quality of flexible substrates and electrodes, the flexibility of perovskite films comes to determine the development of FPSCs. It is prevalent that the cracks usually appear along the grain boundaries in the perovskite films to release the strains during bending operation, which leads to the severe degradation of the photovoltaic performance [188]. Thus, how to release the strains in the perovskite films becomes key point to enhance the bendability of FPSCs. So far, rare investigations are focused on enhancing the bending durability of FPSCs by intrinsically improving the mechanical property of perovskite films.

The well-known lubricating properties of van der Waals interaction enable the individual layers of two-dimensional (2D) materials to slide or rotate with respect to one another easily [189-191]. Zheng et al. demonstrated that the sliding or rotating of one graphite flake with respect to the underneath one under strain could self-retract back to the initial state after the release of the strain [192]. Many other investigations also indicate that the slippage between the neighboring layers in 2D materials is recoverable [193-194]. Therefore, the strain applied onto 2D materials could be released by the sliding or rotating of the interlayer. Recently, two-dimensional perovskites have been investigated widely due to the superior stability, especially the high tolerance to the moisture [195]. Different layers of 2D perovskite are combined by the van der Waals interaction [196], which enables 2D perovskite materials superior flexibility and

deformability [197-198]. Thus, it is very promising to introduce 2D perovskites into the grain boundaries of 3D perovskite films to release the strains which are normally relaxed by the formation of cracks along the grain boundaries in 3D perovskite films.

In this chapter, 2D perovskite PEA_2PbI_4 is introduced into grain boundaries of $MAPbI_3$ perovskite to inherently improve the bendability of perovskite films. The TEM characterization confirms that the 2D perovskites mainly distributed perpendicular to the substrate at the grain boundaries of $MAPbI_3$ films. It is observed that the 2D perovskite can reach a local ultrahigh shear strain level around 0.1 to release the strain in the perovskite films under straining. The DFT calculation demonstrates that the Young's modulus of PEA_2PbI_4 is about 40 times lower than that of $MAPbI_3$ in the out-of-plane direction due to the van der Waals interaction, which enables the van-$MAPbI_3$ films better bendability. Due to the enhanced mechanical property of perovskite films, the FPSCs based on van-$MAPbI_3$ could maintain 94 % of initial PCE after 1000 bending cycles at curvature radius of 3.0 mm. In contrast, the FPSCs base on 3D perovskite retain only 69 % of original PCE. Moreover, due to the passivation of defects at the grain boundaries by 2D perovskite, the PCE of van-$MAPbI_3$ PSC based on glass substrate is boosted to 20.97%. The FPSC based on $MAPbI_3$ demonstrates a PCE of 15.12%. The PCE of FPSCs based on van-$MAPbI_3$ is enhanced to 19.55%. Thus, it is promising and feasible by introducing 2D perovskite at the grain boundaries to enhance the mechanical property of perovskite films and the photovoltaic performance of PSCs

5.2 Devices fabrication and characterization

Materials: CH_3NH_3I was purchased from Dyesol Ltd. PbI_2, bathocuproine (BCP), dimethylformamide (DMF), Poly[bis(4-phenyl)(2,4,6-trimethylphenyl)amine]

(PTAA) and dimethyl sulfoxide (DMSO) were purchased from Sigma-Aldrich Co. LLC. Phenyl-C71-butyric acid methyl ester (PCBM) was purchased from Nano-C Ltd. PET/ITO substrates are used as purchased.

Preparation of flexible PSCs: PTAA dissolved in toluene (2.0 mg/mL) was spin-coated on the ITO/PET substrates at a spin rate of 5000 rpm for 40 s. The films were subsequently annealed on a hotplate at 100 ℃ for 10 min. The perovskite films were prepared by spin-coating the perovskite precursor solution (CH_3NH_3I: 159 mg, PbI_2: 461 mg, DMF: 600 mg, DMSO: 78 mg) at 4000 rpm for 30 s. During the spin coating process, 0.5 ml of diethyl ether was slowly dripped on the rotating substrate in 10 secs after starting. All perovskite films were annealed at 65 ℃ for 1 min and then at 100 ℃ for 10 min. Next, electron transport layers (ETLs) were prepared by spin coating a solution of PCBM in chlorobenzene (20 mg/ml) at 3000 rpm for 40 s, followed by thermal annealing at 90 ℃ for 20 min to crystalize PCBM. BCP dissolved in methanol (0.5 mg/ml) was spin-coated on the PCBM films at 4000 rpm for 30 s. Finally, devices were completed with the evaporation of Ag top electrodes through a shadow mask.

Device characterization: Scanning electron microscopy (SEM) images of perovskite thin films were obtained under a Hitachi S-4300 microscope. The absorption spectra of perovskite films were measured by using a UV-Vis spectro-photometer (UV-2550, Shimadzu, Japan). X-ray diffraction (XRD) measurement was performed using a Rigaku SmartLab X-ray Diffractometer operating at room temperature. Time-resolved photoluminescence (PL) measurements of the samples were carried out by using an Edinburgh FLSP920 fluorescence spectrophotometer. A 485-nm laser was used as an excitation light source. The current density versus voltage (J-V) characteristics of the PSCs were measured by using a Keithley 2400 source meter under the illumination of a AM 1.5 solar simulator with a light intensity of 100 mW/cm^2 (Newport 91160,

300W) and a scan rate of 30 mV/s. The light intensity was calibrated with a standard silicon solar cell. The external quantum efficiencies (EQEs) of the PSCs were measured with a standard test system, including a xenon lamp (Oriel 66,02, 300W), a Si detector (Oriel 76175_71580), a monochromator (Newport 66902) and a dual channel power meter (Newport 2931_C).

5.3   Results and discussion

TEM characterization of perovskite films with the introduction of 2D perovskite (TEM image and DFT calculation)

Figure 5.1. a) The low magnification TEM image of van-MAPbI$_3$ film deposited on carbon support film. b) HRTEM image of grain boundaries of van-MAPbI$_3$ film. The highlighted area (1) and (2) were investigated by the SAED. The SAED patterns of area (1) and (2) are illustrated in c) and d), respectively. e) Schematics of structure of van-MAPbI$_3$ film.

The TEM characterization is conducted to confirm the distribution of 2D perovskite in the MAPbI$_3$ films. The MAPbI$_3$ perovskite precursor with different amount of 2D PEA$_2$PbI$_4$ are spin-coated on carbon-coated copper grids by one-step antisolvent method for TEM investigation. **Figure 5.1a-d** show the TEM characterization image of van-MAPbI$_3$ film with 0.5 % PEA$_2$PbI$_4$ (molar ration respect to MAPbI$_3$). It can be

observed that the adjacent grains are connected tightly as shown in **Figure 5.1a**. **Figure 5.1b** shows the high-resolution TEM (HRTEM) image of grain boundaries of van-MAPbI$_3$ film. The lattice structures in grains and grain boundaries are obviously different, which suggests the different kind of perovskite materials. The selected-area electron diffraction (SAED) is employed to study the lattice structure of area (1) and (2), which are grain and grain boundary, respectively. The corresponding SAED patterns are shown in **Figure 5.1c** and **1d**, respectively. The diffraction spot marked by the red circle in area (1) can be referred to (220) plane of MAPbI$_3$ due to the matched interplane distance of 0.31 nm, which suggests that the grain is 3D MAPbI$_3$ perovskite. The diffraction spot marked by the red circle in area (2) can be indexed as (002) plane of PEA$_2$PbI$_4$ with the interplane spacing of 0.75 nm, demonstrating the material at the grain boundary is 2D PEA$_2$PbI$_4$ perovskite [199]. The TEM study on the van-MAPbI$_3$ perovskite films demonstrates that the 2D perovskites mainly locate at the grain boundaries of 3D perovskites perpendicular to the substrate as demonstrated in **Figure 5.1e**. This structure is prone to utilizing 2D layered materials to release strain by the reversible sliding or rotating between the neighboring layer. For the MAPbI$_3$ film, it can be observed that there are some holes or amorphous structure at the grain boundaries as shown in **Figure5.2a** and **b**, where a mass of defects accumulates. The microscale defects usually serve as stress concentrators that promote propagation of microcracks, leading to poor bendability [200]. The low amount of 2D perovskite prefers to locate at the grain boundaries. Along with the increasing amount, 2D perovskites would partially cover the grains as shown in **Figure 5.3**. The lattice structure of PEA$_2$PbI$_4$ on the grains could be observed clearly under the TEM. The SEM characterization shows that more flake-like grains (2D perovskite) appear on the surface of MAPbI$_3$ films with the increasing amount of PEA$_2$PbI$_4$. This is consistent with the findings in TEM characterization. This could make the van-MAPbI$_3$ films more bendable and deformable due to more van der Waals interactions in the films.
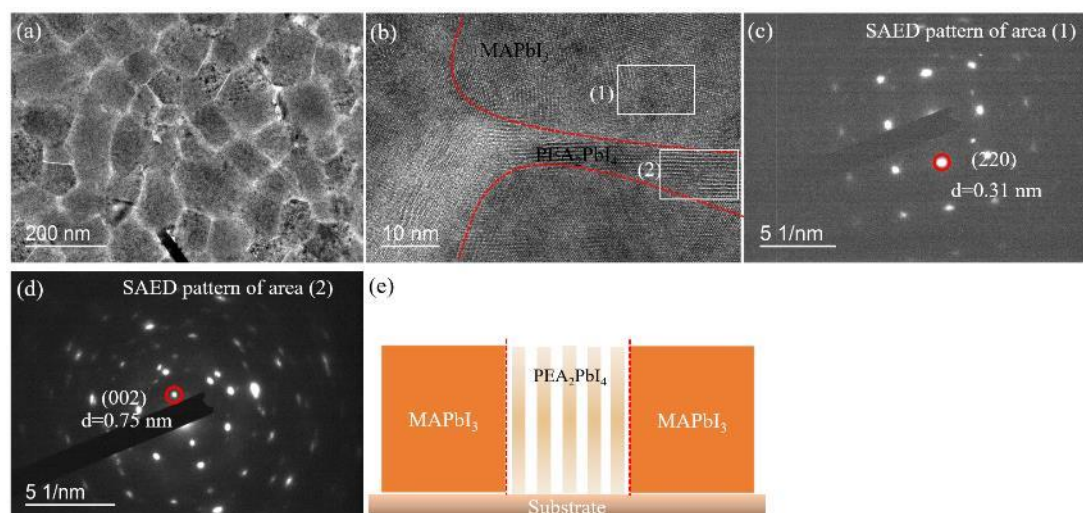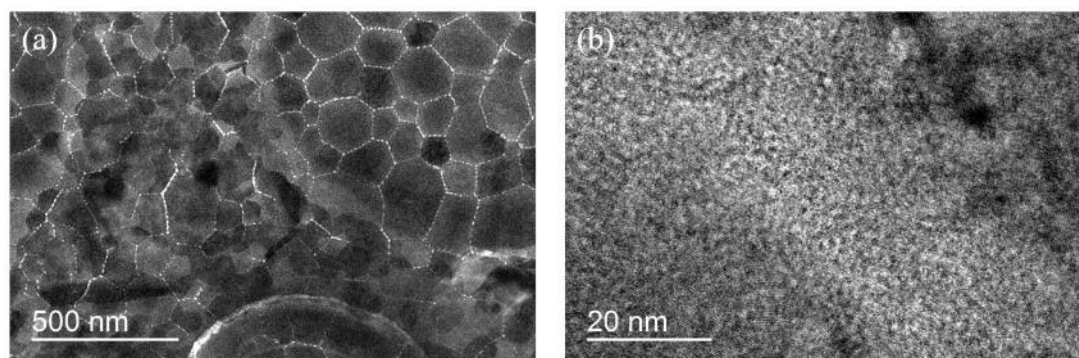
Figure 5.2. a) The low magnification TEM image of MAPbI$_3$ film deposited on carbon support film. b) HRTEM image of grain boundaries of MAPbI$_3$ film.
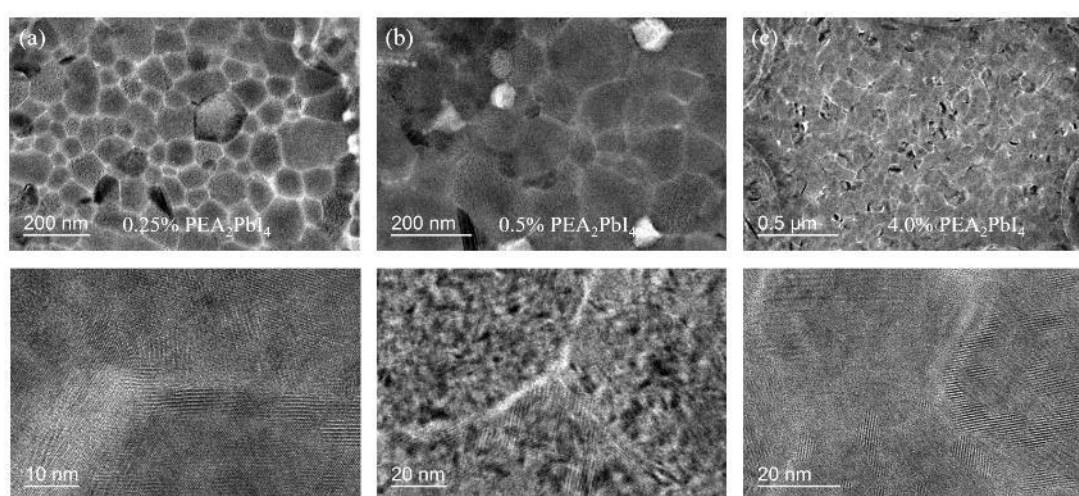
Figure 5.3. TEM images of van-MAPbI$_3$ films with 0.25% a), 0.5% b) and 4% c) PEA$_2$PbI$_4$. The under are the corresponding HRTEM images.

The theoretical calculations of the Young's modulus on 3D and 2D perovskite materials could be useful to deeply understand the mechanical properties. The lower value of Young's modulus could suggest higher deformability of the material. The DFT calculation demonstrates that the in-plane Young's modulus of PEA$_2$PbI$_4$ along a and b directions are calculated to be 18.75 GPa and 12.71 GPa, respectively as shown in **Figure 5.4**. These values are comparable to that of MAPbI$_3$ [201]. The out-of-plane Young's modulus along c direction is calculated to be 0.44 GPa shown in **Figure 5.4d**, which is substantially lower than that of 3D MAPbI$_3$ perovskite (ranging from 15 to 37 GPa) [201]. Thus, the result of theoretical calculation suggests that it can enable the

grain boundaries of $MAPbI_3$ films more deformable by introducing 2D PEA_2PbI_4 with much smaller Young's modulus along out-of-plane direction.
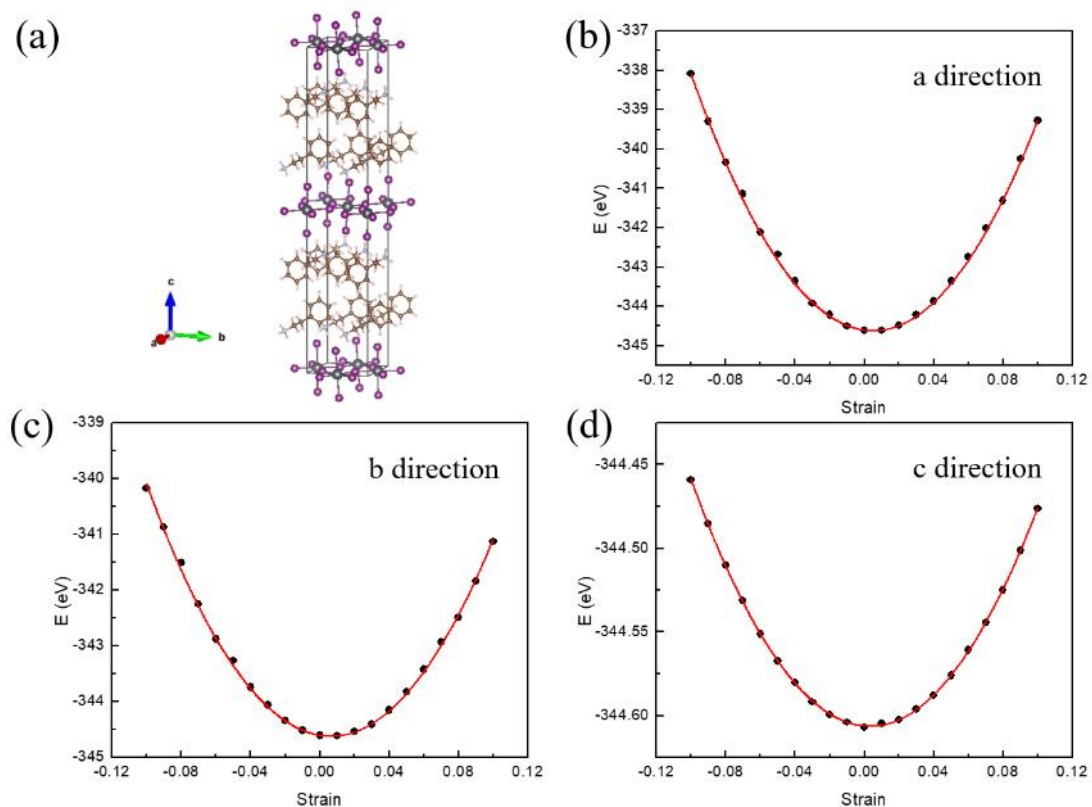
Figure 5.4. Simulation of PEA_2PbI_4 2D perovskite. a) The supercell structure used for simulation. b-c) The potential energy against strain for 2D perovskite along a, b, and c direction predicted by DFT calculations.

TEM characterization of releasing strain by 2D perovskite at the grain boundaries of MAPbI$_3$ film
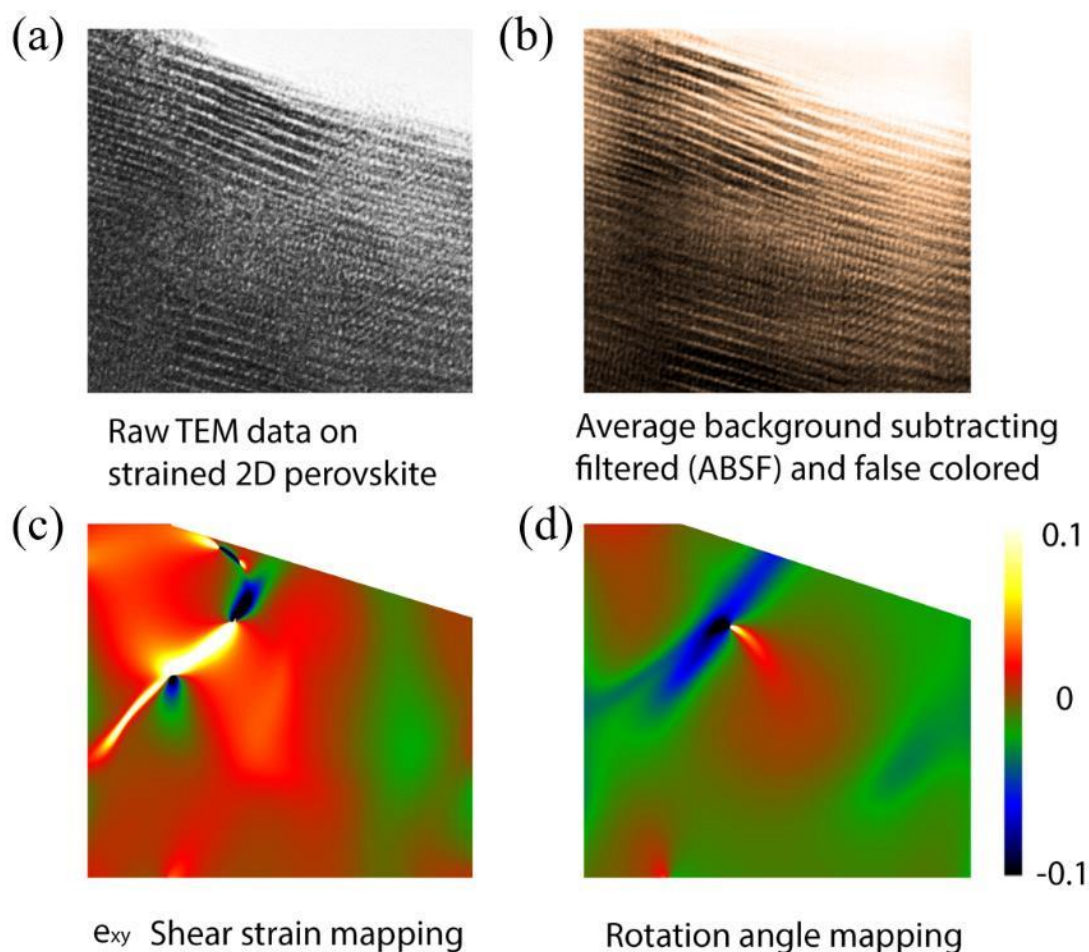
Figure 5.5. The raw a) and filtered HRTEM b) image of a local area close to the crack tip of 2D/3D composite perovskite. c-d) The remaining shear strain illustrated by geometric phase analysis.

In order to investigate how the 2D perovskites release the strain at the grain boundaries, the in-situ strain is applied onto the perovskite films via tearing the underlying carbon films by the damage of electron beams. This method is usually used to study the lattice change of nanomaterials under strain [202-203]. It has been found that the tearing of carbon film could enforce the production of cracks in the perovskite film. It can be obviously observed that the cracks are formed along the grain boundaries, which suggests that the strain in the perovskite film tends to be released by forming

cracks along the grain boundaries (see the supporting information **Figure 5.6**). Since the crack tip is the strain concentrating area, HRTEM is conducted on this area. The raw and filtered HRTEM image of a local area close to the crack tip are shown in **Figure 5.5a** and **b**. The cracking surfaces follow the grain boundaries which is mainly comprised of 2D perovskites and the crack paths are always in the basal plane. The remaining shear strain in local area close to the crack tip can be clearly seen from the geometric phase analysis (GPA) results as displayed in lower panels. The strain-concentrated zones can reach a local ultrahigh shear strain level around 0.1. The normal strain has been totally released in this zone because it is close to the crack surface. The flexible 2D perovskites located at the grain boundaries provides abundant pathways for (strain) energy release in our composite samples.
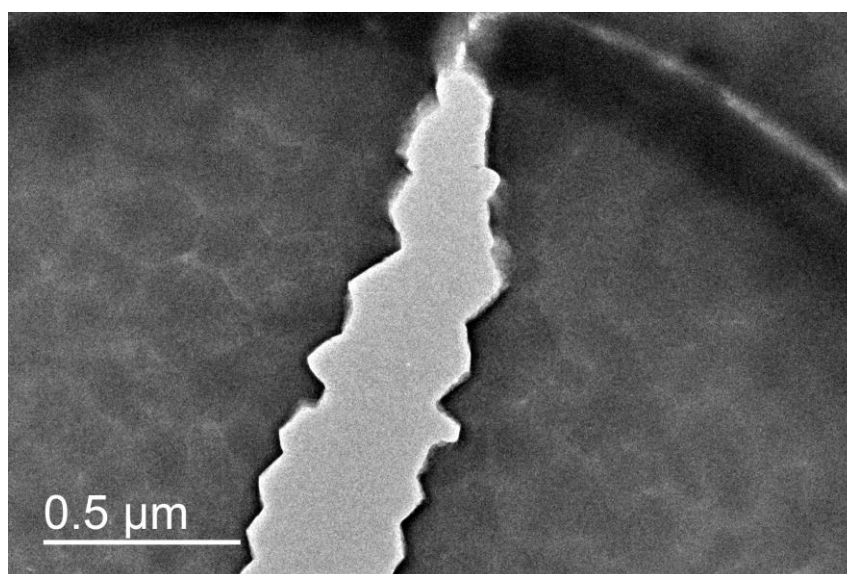
Figure 5.6. The TEM image of cracks in van-MAPbI$_3$ film split by the underlying carbon film.

Bending test of Van-perovskite film under characterization of optical microscopy and SEM
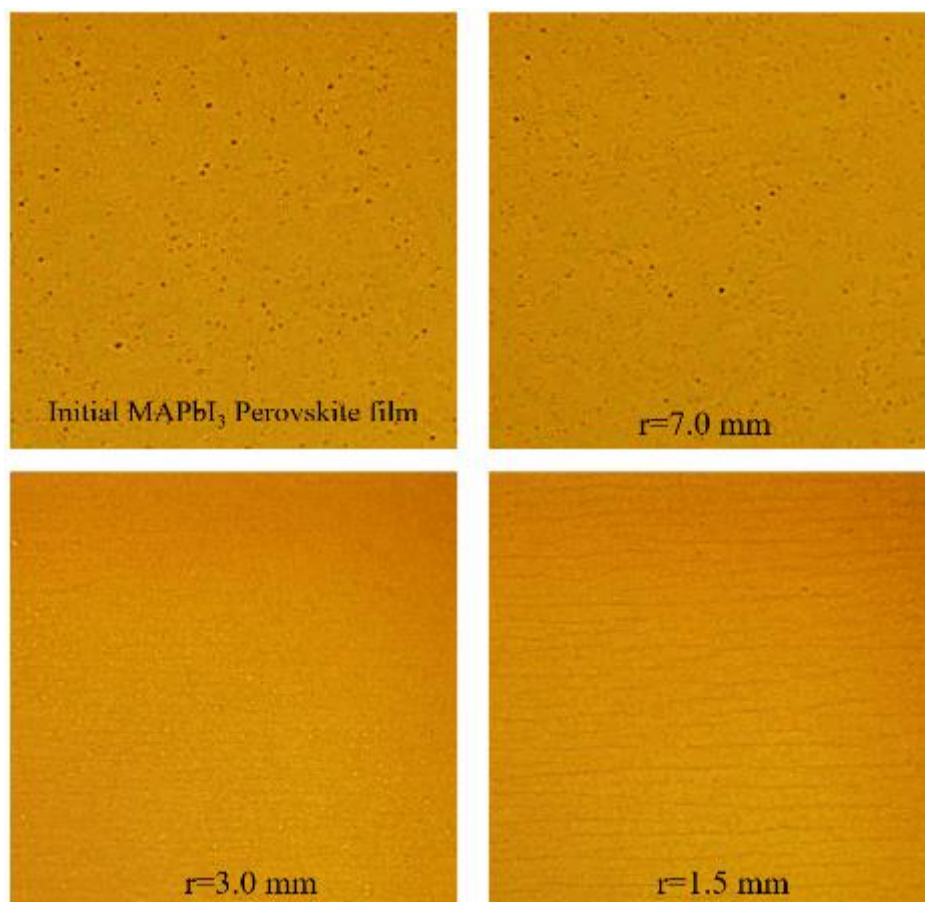
Figure 5.7. The bending evolution of MAPbI$_3$ films along different radius under optical microscope characterization.
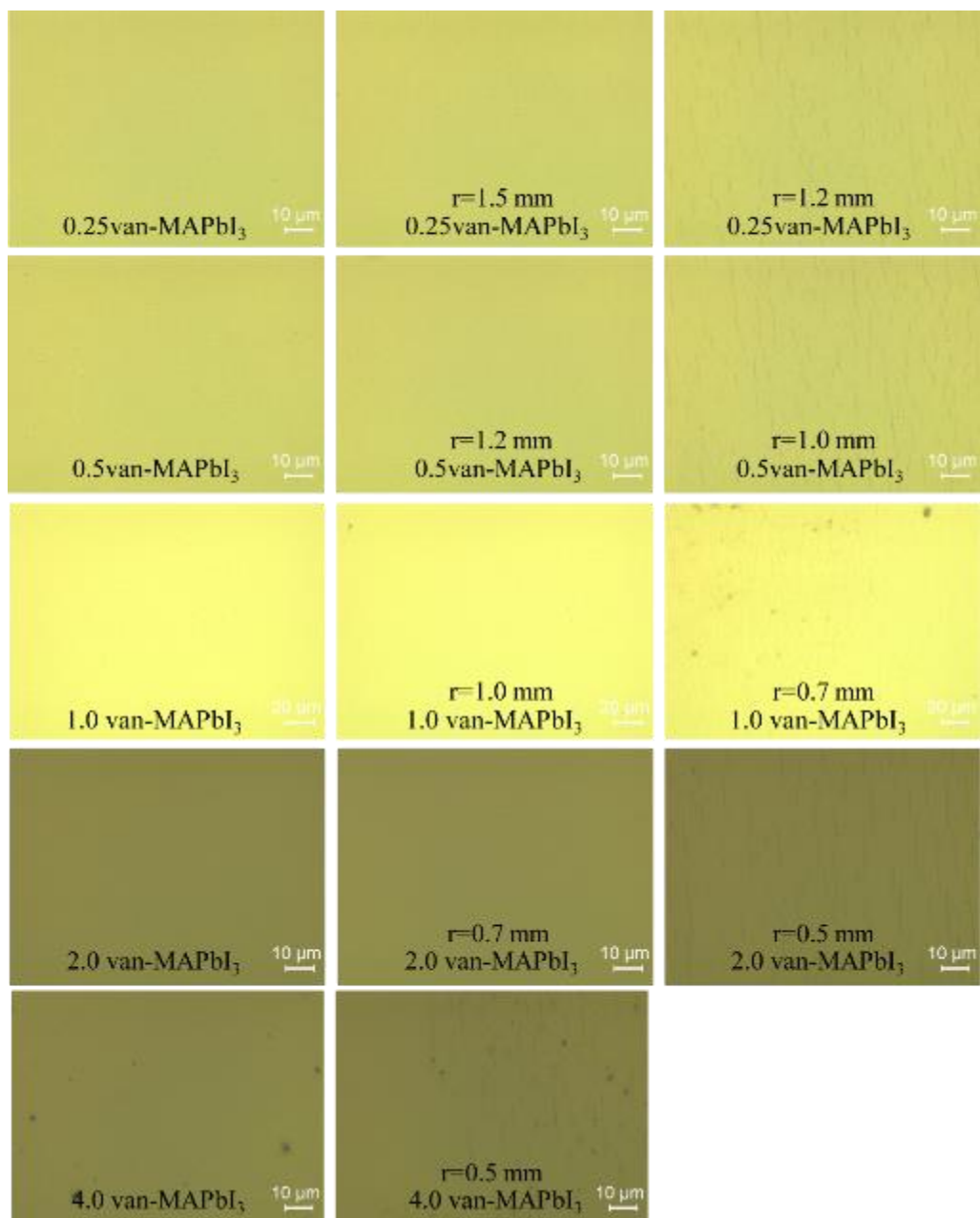
Figure 5.8. The optical images of van-MAPbI$_3$ with different amount of PEA2PbI4 under different bending radius.
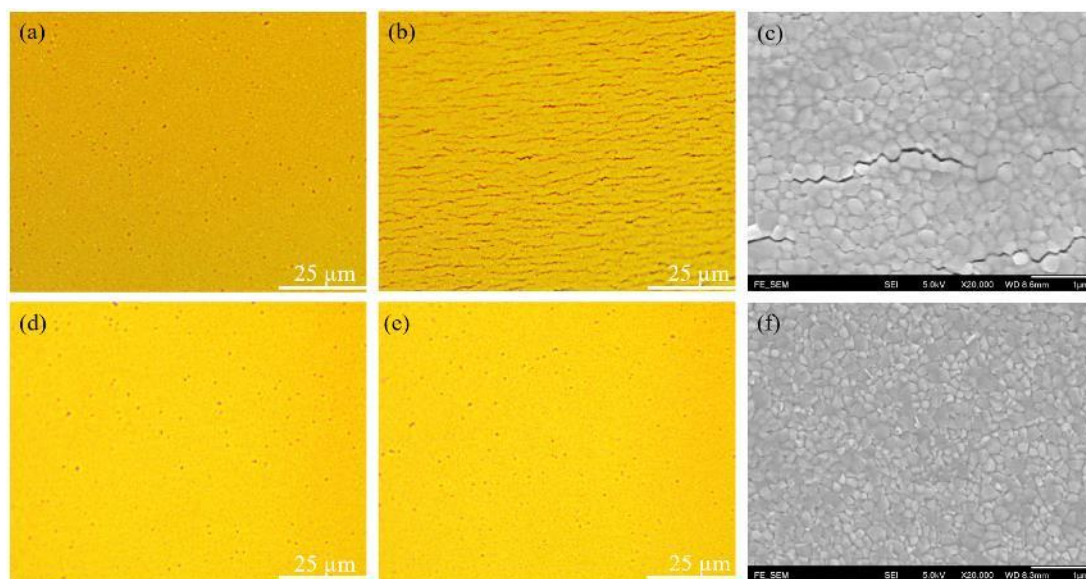
Figure 5.9. The optical photos of initial MAPbI$_3$ film a), film bended for 500 cycles under radius of 3.0 mm b) and the SEM image of same bended film c); The optical photos of initial van-MAPbI$_3$ film d), film bended for 500 cycles under radius of 3.0 nm e) and the SEM image of same bended film f).

The bending durability of perovskite films are tested by bending MAPbI$_3$ and van-MAPbI$_3$ perovskite films deposited on PET substrates with different curvature radius. The optical microscopy characterization demonstrates that cracks appear in MAPbI$_3$ films after bending at curvature radius of 3.0 mm and obvious cracks are generated after bending at radius of 1.5 mm (see the supporting information **Figure 5.7**).   For the van-MAPbI$_3$ film, with the increasing amount of PEA$_2$PbI$_4$, the critical radius decreases when cracks appear in the films (see supporting information **Figure 5.8**). This supports the assumption that the introduction of more 2D perovskite could make the perovskite films more bendable and deformable. For van-MAPbI$_3$ film with 0.5% PEA$_2$PbI$_4$, cracks begin to appear at the radius of 1.0 mm, which is much smaller than 3.0 mm for MAPbI$_3$ film. **Figure 5.9** show the optical and SEM images of MAPbI$_3$ and van-MAPbI$_3$ with 0.5% PEA$_2$PbI$_4$ films before and after bending for 500 cycles under radius of 3.0 mm. After bending for 500 cycles, many cracks appear in the films shown in **Figure 5.9b**. The SEM characterization was conducted onto the

same bended film to confirm the cracks. It can be observed that the cracks appear along the grain boundaries shown in **Figure 5.9c**. For the van-MAPbI$_3$ films, no obvious cracks are observed under the optical and SEM images. These results suggest that the intrinsic mechanical property of perovskite films is significantly improved by the introduction of 2D perovskite, which could release the strains at the grain boundaries.

Optoelectronic properties of van-perovskite films
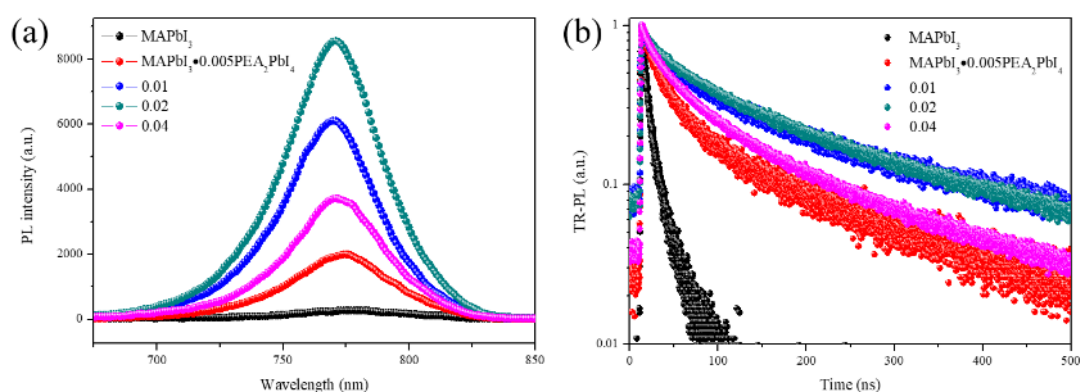
Figure 5.10. The steady a) and time resolved b) photoluminescence characterizations of MAPbI$_3$ and van-MAPbI$_3$ with different amount of PEA$_2$PbI$_4$.
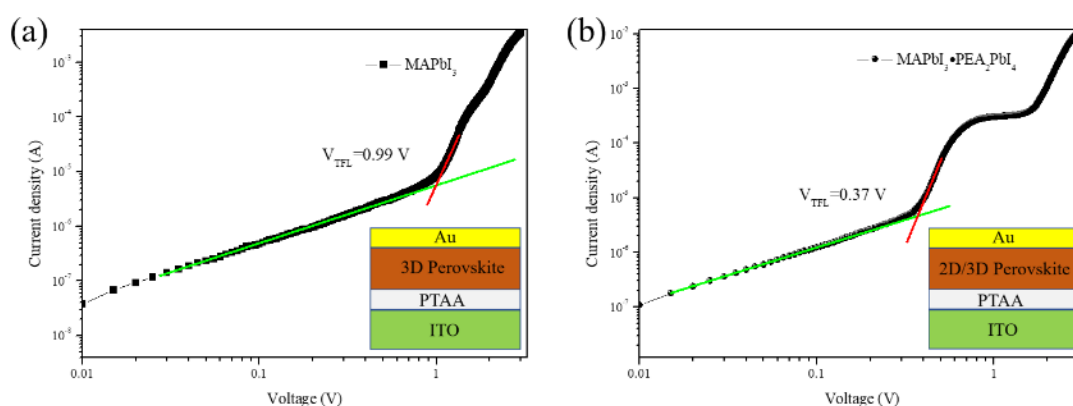
Figure 5.11. Current density-voltage characteristics of hole only devices based on MAPbI$_3$ film a) and van-MAPbI$_3$ film b).

To gain insight into the effect of 2D perovskite on the optoelectronic property of

MAPbI$_3$ film, the steady-state photoluminescence (PL) and time-resolved PL were characterized on MAPbI$_3$ and van-MAPbI$_3$ films deposited on glass substrates with different amount of PEA$_2$PbI$_4$ shown in **Figure 5.10**. As shown in **Figure 5.10a**, the PL intensity of MAPbI$_3$ film is increased by about 7 times with the incorporation of 5% PEA$_2$PbI$_4$. The PL decays shown in **Figure 5.10b** are fitted by using a biexponential equation: $Y= A_1exp(-t/\tau_1) + A_2exp(-t/\tau_2)$. The carrier dynamics derived from the transient PL decay reveals the information of carrier recombination related to defect density. The carrier lifetime of MAPbI$_3$ is significantly improved from 7.6 ns to 82.2 ns by incorporating PEA$_2$PbI$_4$. With the increasing amount of PEA$_2$PbI$_4$, the PL intensity and carrier lifetime of perovskite film increase significantly due to the passivation of defects at the grain boundaries (see the supporting information **Table 5.1**). However, too much PEA$_2$PbI$_4$ could lead to the decreasing of PL intensity and carrier lifetime because of the insulating organic cation PEA and low carrier density of 2D perovskite. The enhanced PL intensity and carrier lifetime suggest that the introduction of 2D perovskite into the grain boundaries could significantly suppress the non-radiative recombination in MAPbI$_3$ films due to the modification of amorphous grain boundaries into high crystallinity perovskite.

To quantitatively evaluate the change of defect density of PEA$_2$PbI$_4$ modified perovskite films, the devices (ITO/PTAA/Perovskite/Au) with and without PEA$_2$PbI$_4$ are fabricated. **Figure 5.11a** and **5.11b** show the J-V curves of devices without and with 0.5 % PEA$_2$PbI$_4$, respectively. The defect density could be determined by the trap-filled limit voltage (V$_{TFL}$) according to the equation [168, 204]

$$N_{defects} = 2\varepsilon\varepsilon_0 V_{TFL}/eL^2 \qquad (1)$$

Where L is the thickness of the perovskite film, ε and ε_0 are the relative dielectric constant of MAPbI$_3$ and the vacuum dielectric permittivity, respectively, and *e* is the

elementary charge. The calculated defect densities ($N_{defects}$) are 2.19×10^{16} cm^{-3} and

0.82×10^{16} cm^{-3} for MAPbI$_3$ and van-MAPbI$_3$ with 5% PEA$_2$PbI$_4$ films, respectively.

The lower defect density of van-MAPbI$_3$ film is consistent with the results of PL

characterizations.

Table 5.1. The detailed parameters of TRPL of MAPbI$_3$ and van-MAPbI$_3$ with
different amount of PEA$_2$PbI$_4$.

Type of film	τ_1 (ns)	τ_2 (ns)	τ (ns)
MAPbI$_3$·0.005PEA$_2$PbI$_4$	122.59	19.00	82.2
MAPbI$_3$·0.01PEA$_2$PbI$_4$	17.20	133.87	118.0
MAPbI$_3$·0.02PEA$_2$PbI$_4$	149.77	22.31	134.1
MAPbI$_3$·0.04PEA$_2$PbI$_4$	19.99	113.86	90.9
MAPbI$_3$	22.89	5.31	7.6

PCE and bending stability of perovskite solar cells based on van-perovskite
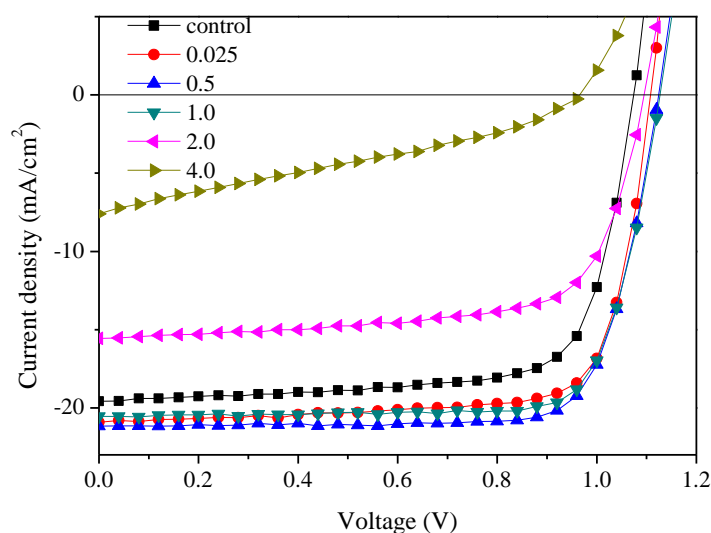
Figure 5.12. The J-V curves of FPSCs based on MAPbI$_3$ and van-MAPbI$_3$ with
different amount of PEA$_2$PbI$_4$.
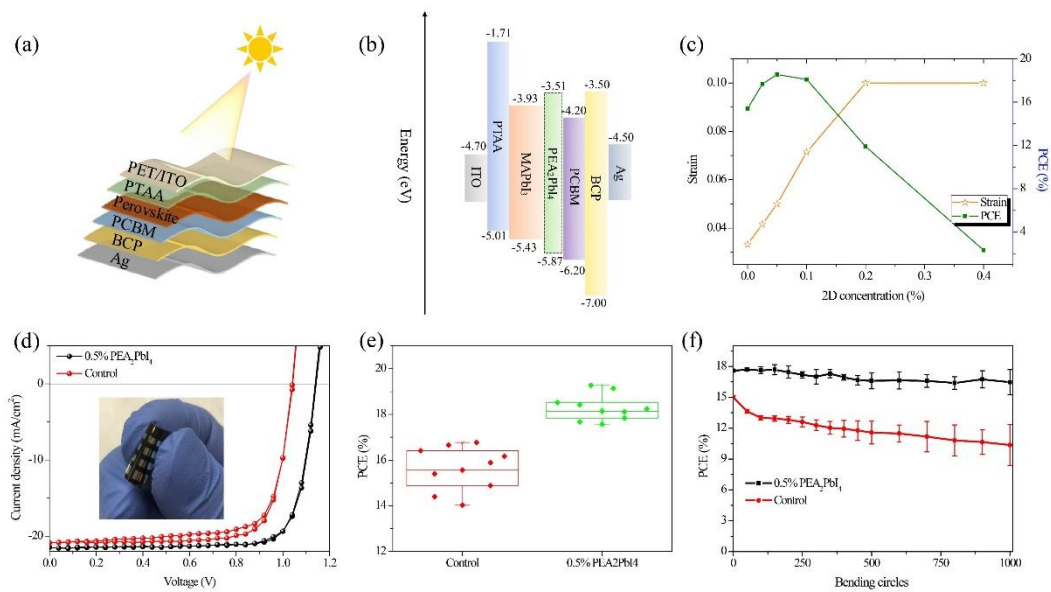
Figure 5.13 a) The structure of flexible perovskite solar cells. b) The band alignment of different layers of FPSCs. c) The evolution of bendability (critical strain) of perovskite film and PCE of FPSC upon different amount of PEA_2PbI_4. d) J-V curves of flexible devices based on $MAPbI_3$ and van-$MAPbI_3$ films. e) The PCE distribution of 10 flexible devices based on $MAPbI_3$ and van-$MAPbI_3$ films. f) PCE degradation of $MAPbI_3$ and van-$MAPbI_3$ devices upon increasing the bending cycles.

FPSCs are fabricated with the structure of PET/ITO/PTAA/perovskite/PCBM/BCP/Ag. The photovoltaic performance of FPSCs are optimized by adjusting the amount of PEA_2PbI_4 in the perovskite precursor as shown in **Figure 5.13**. The corresponding parameters are shown in **Table 5.2**. FPSCs based on van-$MAPbI_3$ with 5% PEA_2PbI_4 could achieve the best photovoltaic performance. **Figure 5.13a** shows the configuration of flexible perovskite sola cell. The band alignment of different layers in FPSCs is shown in **Figure 5.13b**. It can be observed that the level of conduction band and valence band of PEA_2PbI_4 would prevent the charge carriers (hole and electrons) aggregating at the grain boundaries, which could suppress the non-radiative recombination in the perovskite films. **Figure 5.13c** shows the evolution of bendability (critical strain) of perovskite film and PCE of

FPSC upon different amount of PEA_2PbI_4. There is a compromise between the efficiency of FPSCs and the bendability of perovskite films. **Figure 5.13d** shows the J-V curves of champion FPSCs base on $MAPbI_3$ and van-$MAPbI_3$ with 5% PEA_2PbI_4. The control FPSC could achieve the PCE of 16.77% with V_{oc} of 1.04 V, J_{sc} of 20.88 mA/cm^2, FF of 77.23%. The PCE of van-$MAPbI_3$ device can be improved to 19.56% with V_{oc} of 1.14 V, J_{sc} of 21.46 mA/cm^2, and FF of 79.95%. **Figure 5.14** shows the external quantum efficiency (EQE) spectra of the corresponding devices. The integrated current densities are 19.21 mA/cm^2 and 20.02 mA/cm^2, respectively, which are close to the results of *J-V* measurements. **Figure 5.13e** shows the PCE distribution of 10 flexible devices based on $MAPbI_3$ and van-$MAPbI_3$ films. The average PCE for control devices is 15.62±0.90%. For the van-$MAPbI_3$ devices, the average PCE is 18.29±0.54%. The best PCE of rigid PSC based on glass substrate could reach 20.97% with V_{oc} of 1.13 V, J_{sc} of 23.13 mA/cm^2, and FF of 80.23% as shown in **Figure 5.16**. It can be observed that the photovoltaic enhancement is mainly resulted from the increased V_{oc} and FF, which is due to the suppression of non-radiative recombination by the introduction of 2D perovskite. The bending stability of FPSCs base on $MAPbI_3$ and van-$MAPbI_3$ with 5% PEA_2PbI_4 are shown in **Figure 5.13f**. The PCE kept 96% after bending the van-device with curvature radius of 3.0 mm. For the control device, the PCE was only 74% of the initial value. Both of devices suffer obvious PCE reduction when bended at the curvature radius of 1.5 mm. Then we fixed the bending curvature radius at 3.0 mm to test the bending stability for multiple cycles shown in **Figure 5.13f**. After bending 1000 cycles, the FPSCs base on van-$MAPbI_3$ with 5% PEA_2PbI_4 kept about 94% of initial PCE, while the control devices retained about 69% of initial PCE. Thus, the introduction of 2D perovskite into the grain boundaries of $MAPbI_3$ could significantly improve both the PCE and bending durability of flexible perovskite solar cell.
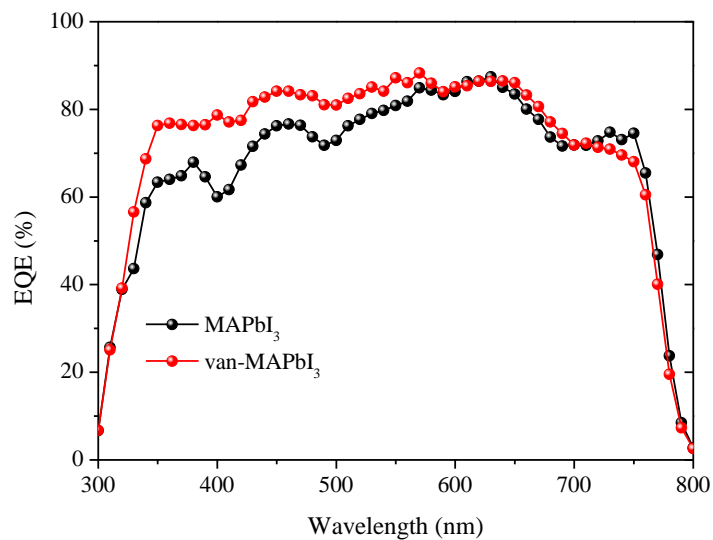
Figure 5.14. The external quantum efficiency spectra of devices based on MAPbI$_3$ and MAPbI3 with 0.5% PEA$_2$PbI$_4$.
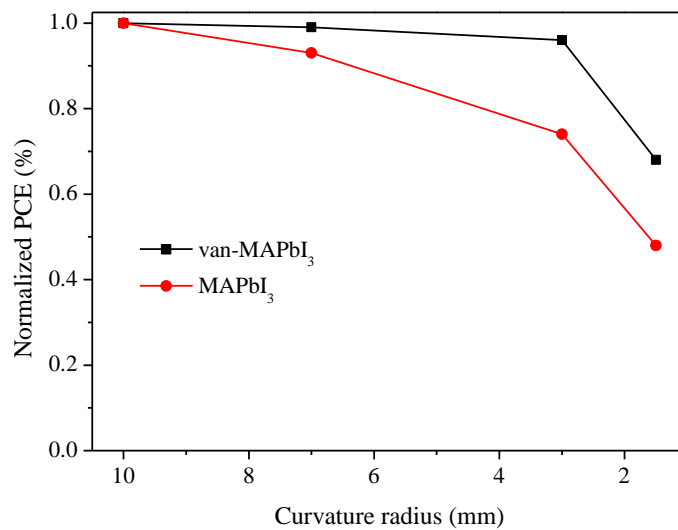
Figure 5.15. The bending stability of FPSCs base on MAPbI$_3$ and van-MAPbI$_3$ with 5% PEA$_2$PbI$_4$.
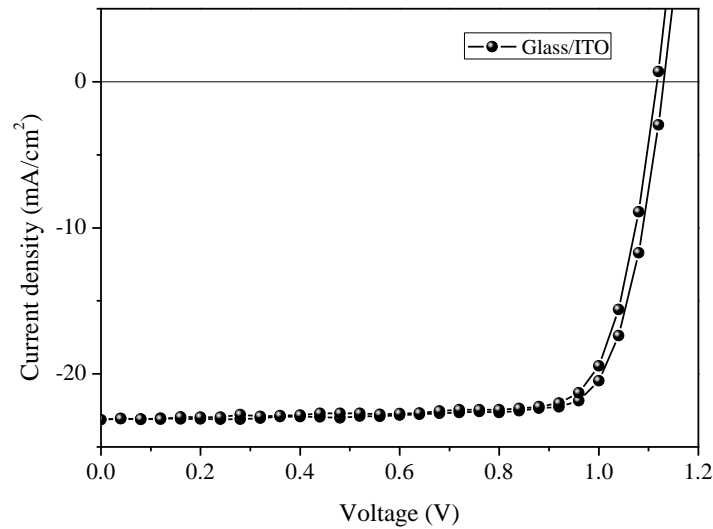
Figure 5.16. The J-V curve of van-MAPbI$_3$ with 0.5% PEA$_2$PbI$_4$ device based on glass substrate.

Table 5.2. The photovoltaic parameters of FPSCs based on different amount of PEA$_2$PbI$_4$ in the precursor.

Amount of PEA$_2$PbI$_4$	V_{oc} (V)	J_{sc} (mA/cm^2)	FF (%)	PCE (%)
0	1.07	19.57	73.54	15.40
0.25%	1.11	20.91	76.13	17.67
0.5%	1.12	21.16	78.31	18.56
1.0%	1.13	20.54	77.94	18.09
2.0%	1.09	15.56	70.22	11.91
4.0%	0.96	7.60	31.80	2.32

5.4   Summary

In summary, van der Waals interactions are introduced into the grain boundaries of MAPbI$_3$ films by incorporating 2D perovskite in the perovskite precursors. The bendability and deformability of perovskite film is significantly improved via the sliding or rotating between adjacent layers to release the strain under bending operation. FPSCs based on van-MAPbI$_3$ could maintain 94% of initial PCE after bending 1000 cycles at curvature radius of 3.0 mm, while only 69% of initial value is

remained for the control device. Besides, the 2D perovskite could passivate the defects at the grain boundaries of perovskite films, leading to the enhanced PCE to 19.55% and 20.97% for devices based on flexible and glass substrates, respectively. This work provides a new strategy to improve the intrinsic flexibility of perovskite film.

Chapter 6   Conclusions and Perspectives

6.1   Conclusions

In this thesis, we have systematically reviewed perovskite solar cells from crystal structure, optoelectronic properties, fabrication approaches, devices configurations, working mechanisms, efficiency development, and current issues. This literature review gives a clear understanding of reasons for the success of perovskite solar cells and current problems. Defects in the perovskite films hinder the further improvement of photovoltaic performance of perovskite solar cells. Two strategies are proposed to enhance the crystallinity and decrease the defects for the perovskite films. The photovoltaic performances have been significantly improved. One strategy is provided to improve the bendability of perovskite films to prepare intrinsically flexible perovskite solar cells.

Retarding the crystallization process of perovskite films is a useful strategy to prepare perovskite films with large grain size and low defect density. In our strategy, $PbAc_2$ is introduced into the perovskite precursor to control the perovskite crystallization process. The $PbAc_2$ additive serves as cross linking agent to form strong hydrogen bonding with MAI, leading to a more stable perovskite intermediate phase, and substantially retards the crystallization process of perovskite films. The grain size of perovskite films is enlarged from 250 nm to 500 nm in average. As a result, perovskite thin films with better morphology and larger grains are obtained by using this technique. Due to the high-quality perovskite films with low defect densities, the performance of PSCs is significantly improved in terms of the efficiency and stability. This work provides a novel approach for optimizing the performance of PSCs and

other perovskite optoelectronic devices prepared by solution processes.

Controlling the growth of perovskite films with preferential orientation is another useful approach to improve the photovoltaic performance of perovskite solar cells. we demonstrate the van der Waals epitaxial growth of $MAPbI_3$ perovskite on MoS_2 flakes by a one-step antisolvent method for the first time. High-quality perovskite films with large grain sizes and highly preferential orientation on MoS_2 interlayers have been obtained in PSCs, leading to high PCEs as well as good stability of the devices. The preferential growth of perovskites on MoS_2 flakes is due to the van der Waals surface of MoS_2 and the lattice parameters between MoS_2 and $MAPbI_3$ perovskite. Considering that 2D materials with different crystal structures are readily available, we can realize vdW epitaxial growth of perovskite films with different compositions by choosing suitable 2D material templates and achieve different types of PSCs with high-performance. This work paves a way for preparing epitaxial perovskite films by a convenient solution process, which will be useful in preparing not only PSCs but also other types of perovskite optoelectronic devices.

Van der Waals interactions are introduced into the grain boundaries of $MAPbI_3$ films by incorporating 2D perovskite in the perovskite precursors. The bendability and deformability of perovskite film is significantly improved via the sliding or rotating between adjacent layers to release the strain under bending operation. FPSCs based on van-$MAPbI_3$ could maintain 94% of initial PCE after bending 1000 cycles at curvature radius of 3.0 mm, while only 69% of initial value is remained for the control device. Besides, the 2D perovskite could passivate the defects at the grain boundaries of perovskite films, leading to the enhanced PCE to 19.55% and 20.97% for devices based on flexible and glass substrates, respectively. This work provides a new strategy to improve the intrinsic flexibility of perovskite film.

6.2   Perspectives

Due to the high efficiency and low cost, perovskite solar cells have great potential to be commercialized and replace the silicon solar cells in the future. In addition, since the flexible deposition of perovskite films on different substrates, like plastic substrates, lightweight or flexible PSCs can be prepared and fulfill various applications. Although PSCs have lots of advantages to be as next-generation photovoltaic technologies, some issues need to be solved before the commercialization. Among them, the long-term stability is the most important issue for the real applications of optoelectronic devices based on perovskite materials.

1.   The long-term air stability of perovskite solar cells is associated with the chemical stability of perovskite materials, ion migration, interface and metal electrode degradation, and light degradation of transporting layers. With the efforts of researchers, the stability of perovskite solar cells is improved from the initial value of several minutes to thousand hours reported in the literatures. However, the stability testing standards are different in different literatures. The nonstandard testing of stability could not demonstrate the true developing status of stability issue for perovskite solar cells, which could retard the development of PSC community. There are well-established standards [International electrotechnical commission (IEC) 61215 or 61646] in mature crystalline silicon photovoltaic technologies. It needs to further make sure if this standard can be applied to perovskite solar cells. And new standard testing protocols should be proposed, which could reasonably estimate the lifetime of perovskite solar cells.

2.   Although the record efficiency of perovskite solar cells reached 24.2% now, the device area is relatively small (about 0.1 cm^2). The devices with area of 1 cm^2 demonstrate the efficiency of about 20%. The up scaling of the device area would

sacrifice the efficiency of PSCs. However, small area devices would have limiting application value. The lower efficiency of large-area PSCs is due to the low quality of perovskite films. It is hard to prepare pinhole free and uniform perovskite films by spin-coating method. Thus, new techniques should be explored to prepare large-area perovskite films with high quality and low cost.

3.   The toxicity of raw perovskite materials is the most concerned issue for human public. The lead leakage from lead contained perovskites could contaminate the environment and damage the human health. Although tin is a promising alternative to replace lead to prepare tin-based perovskite solar cells, the easy oxidation of Sn^{2+} to Sn^{4+} would introduce many defects, which results in low efficiency. Therefore, more efforts are needed to prevent the oxidation of Sn^{2+} and prepare high quality tin-base perovskites. In addition, other elements are investigated to replace Pb to prepare perovskite films with superior optoelectronic properties. Besides, the better encapsulation of devices also could prevent the leakage of lead to the environment. And the recycle of disabled devices is equally important.

Due to the excellent properties of perovskite materials, more and more researchers would be stimulated to make efforts to solve the current problems and accelerate the commercialization. It can be expected that perovskite solar cells would largely contribute to the electricity generation for the people in the future.

References

[1]   M. A. Green, A. Ho-Baillie, H. J. Snaith, *Nat. Photonics* **2014**, 8, 506.

[2]   A. K. Jena, A. Kulkarni, T. Miyasaka, *Chem. Rev.* **2019**, 119, 3036.

[3]   M. Kaltenbrunner, G. Adam, E. D. Głowacki, M. Drack, R. Schwödiauer, L. Leonat, D. H. Apaydin, H. Groiss, M. C. Scharber, M. S. White, N. S. Sariciftci, S. Bauer, *Nat. Mater.* **2015**, 14, 1032.

[4]   Y. Wang, S. Bai, L. Cheng, N. Wang, J. Wang, F. Gao, W. Huang, *Adv. Mater.* **2016**, 28, 4532.

[5]   Y. Li, L. Meng, Y. Yang, G. Xu, Z. Hong, Q. Chen, J. You, G. Li, Y. Yang, Y. Li, *Nat. Commun.* **2016**, 7, 10214.

[6]   Y. Zhao, K. Zhu, *Chem. Soc. Rev.* **2016**, 45, 655.

[7]   N.-G. Park, *Mater. Today* **2015**, 18, 65.

[8]   T. Baikie, N. S. Barrow, Y. Fang, P. J. Keenan, P. R. Slater, R. O. Piltz, M. Gutmann, S. G. Mhaisalkar, T. J. White, *J. Mater. Chem. A* **2015**, 3, 9298.

[9]   Z. Fan, K. Sun, J. Wang, *J. Mater. Chem. A* **2015**, 3, 18809.

[10]   W.-J. Yin, T. Shi, Y. Yan, *Adv. Mater.* **2014**, 26, 4653.

[11]   E. Mosconi, A. Amat, M. K. Nazeeruddin, M. Grätzel, F. De Angelis, *J. Phys. Chem. C* **2013**, 117, 13902.

[12]   J. H. Noh, S. H. Im, J. H. Heo, T. N. Mandal, S. I. Seok, *Nano Lett.* **2013**, 13, 1764.

[13]   G. C. Xing, N. Mathews, S. Y. Sun, S. S. Lim, Y. M. Lam, M. Gratzel, S. Mhaisalkar, T. C. Sum, *Science* **2013**, 342, 344.

[14]   S. D. Stranks, G. E. Eperon, G. Grancini, C. Menelaou, M. J. P. Alcocer, T. Leijtens, L. M. Herz, A. Petrozza, H. J. Snaith, *Science* **2013**, 342, 341.

[15]   Q. Dong, Y. Fang, Y. Shao, P. Mulligan, J. Qiu, L. Cao, J. Huang, *Science* **2015**, 347, 967.

[16]   Y. Dang, Y. Liu, Y. Sun, D. Yuan, X. Liu, W. Lu, G. Liu, H. Xia, X. Tao,

Cryst. Eng. Comm **2015**, 17, 665.

[17]   Y. Liu, Z. Yang, D. Cui, X. Ren, J. Sun, X. Liu, J. Zhang, Q. Wei, H. Fan, F. Yu, X. Zhang, C. Zhao, S. Liu, *Adv. Mater.* **2015**, 27, 5176.

[18]   D. Shi, V. Adinolfi, R. Comin, M. Yuan, E. Alarousu, A. Buin, Y. Chen, S. Hoogland, A. Rothenberger, K. Katsiev, Y. Losovyj, X. Zhang, P. A. Dowben, O. F. Mohammed, E. H. Sargent, O. M. Bakr, *Science* **2015**, 347, 519.

[19]   J. Feng, X. Zhu, Z. Yang, X. Zhang, J. Niu, Z. Wang, S. Zuo, S. Priya, S. Liu, D. Yang, *Adv. Mater.* **2018**, 30, 1801418.

[20]   M. Xiao, F. Huang, W. Huang, Y. Dkhissi, Y. Zhu, J. Etheridge, A. Gray-Weale, U. Bach, Y.-B. Cheng, L. Spiccia, *Angew. Chem. In. Ed.* **2014**, 53, 9898.

[21]   N. J. Jeon, J. H. Noh, Y. C. Kim, W. S. Yang, S. Ryu, S. Il Seol, *Nat. Mater.* **2014**, 13, 897.

[22]   W. Nie, H. Tsai, R. Asadpour, J.-C. Blancon, A. J. Neukirch, G. Gupta, J. J. Crochet, M. Chhowalla, S. Tretiak, M. A. Alam, H.-L. Wang, A. D. Mohite, *Science* **2015**, 347, 522.

[23]   J. Burschka, N. Pellet, S. J. Moon, R. Humphry-Baker, P. Gao, M. K. Nazeeruddin, M. Gratzel, *Nature* **2013**, 499, 316.

[24]   Z. Xiao, C. Bi, Y. Shao, Q. Dong, Q. Wang, Y. Yuan, C. Wang, Y. Gao, J. Huang, *Energy Environ. Sci.* **2014**, 7, 2619.

[25]   M. Liu, M. B. Johnston, H. J. Snaith, *Nature* **2013**, 501, 395.

[26]   J. J. Zhao, P. Wang, Z. H. Liu, L. Y. Wei, Z. Yang, H. R. Chen, X. Q. Fang, X. L. Liu, Y. H. Mai, *Dalton Trans.* **2015**, 44, 17841.

[27]   H. Chen, F. Ye, W. Tang, J. He, M. Yin, Y. Wang, F. Xie, E. Bi, X. Yang, M. Grätzel, L. Han, *Nature* **2017**, 550, 92.

[28]   Q. Chen, H. Zhou, Z. Hong, S. Luo, H.-S. Duan, H.-H. Wang, Y. Liu, G. Li, Y. Yang, *J. Am. Chem. Soc.* **2014**, 136, 622.

[29]   A. Kojima, K. Teshima, Y. Shirai, T. Miyasaka, *J. Am. Chem. Soc.* **2009**, 131,

6050.

[30]   Y. Rong, Y. Hu, A. Mei, H. Tan, M. I. Saidaminov, S. I. Seok, M. D. McGehee, E. H. Sargent, H. Han, *Science* **2018**, 361, eaat8235.

[31]   K. A. Bush, A. F. Palmstrom, Z. J. Yu, M. Boccard, R. Cheacharoen, J. P. Mailoa, D. P. McMeekin, R. L. Z. Hoye, C. D. Bailie, T. Leijtens, I. M. Peters, M. C. Minichetti, N. Rolston, R. Prasanna, S. Sofia, D. Harwood, W. Ma, F. Moghadam, H. J. Snaith, T. Buonassisi, Z. C. Holman, S. F. Bent, M. D. McGehee, *Nat. Energy* **2017**, 2, 17009.

[32]   J. X. Zhou, Z. W. Ren, S. H. Li, Z. C. Liang, C. Surya, H. Shen, *Mater. Lett.* **2018**, 220, 82.

[33]   G. E. Eperon, T. Leijtens, K. A. Bush, R. Prasanna, T. Green, J. T.-W. Wang, D. P. McMeekin, G. Volonakis, R. L. Milot, R. May, A. Palmstrom, D. J. Slotcavage, R. A. Belisle, J. B. Patel, E. S. Parrott, R. J. Sutton, W. Ma, F. Moghadam, B. Conings, A. Babayigit, H.-G. Boyen, S. Bent, F. Giustino, L. M. Herz, M. B. Johnston, M. D. McGehee, H. J. Snaith, *Science* **2016**, 354, 861.

[34]   H.-S. Kim, C.-R. Lee, J.-H. Im, K.-B. Lee, T. Moehl, A. Marchioro, S.-J. Moon, R. Humphry-Baker, J.-H. Yum, J. E. Moser, M. Grätzel, N. G. Park, *Sci. Rep.* **2012**, 2, 591.

[35]   M. M. Lee, J. Teuscher, T. Miyasaka, T. N. Murakami, H. J. Snaith, *Science* **2012**, 338, 643.

[36]   J. H. Heo, S. H. Im, J. H. Noh, T. N. Mandal, C.-S. Lim, J. A. Chang, Y. H. Lee, H.-J. Kim, A. Sarkar, M. K. Nazeeruddin, M. Grätzel, S. I. Seok, *Nat. Photonics* **2013**, 7, 486.

[37]   H. Zhou, Q. Chen, G. Li, S. Luo, T. Song, H.-S. Duan, Z. Hong, J. You, Y. Liu, Y. Yang, *Science* **2014**, 345, 542.

[38]   N. J. Jeon, J. H. Noh, W. S. Yang, Y. C. Kim, S. Ryu, J. Seo, S. I. Seok, *Nature* **2015**, 517, 476.

[39]   W. S. Yang, J. H. Noh, N. J. Jeon, Y. C. Kim, S. Ryu, J. Seo, S. I. Seok, *Science* **2015**, 348, 1234.

[40]   M. Saliba, T. Matsui, J.-Y. Seo, K. Domanski, J.-P. Correa-Baena, M. K. Nazeeruddin, S. M. Zakeeruddin, W. Tress, A. Abate, A. Hagfeldt, M. Grätzel, *Energy Environ. Sci.* **2016**, 9, 1989.

[41]   W. S. Yang, B. W. Park, E. H. Jung, N. J. Jeon, Y. C. Kim, D. U. Lee, S. S. Shin, J. Seo, E. K. Kim, J. H. Noh, S. I. Seok, *Science* **2017**, 356, 1376.

[42]   Q. Jiang, Y. Zhao, X. Zhang, X. Yang, Y. Chen, Z. Chu, Q. Ye, X. Li, Z. Yin, J. You, *Nat. Photonics* **2019**, 13, 460.

[43]   C. Bi, B. Chen, H. Wei, S. DeLuca, J. Huang, *Adv. Mater.* **2017**, 29, 1605900.

[44]   M. Li, Y.-G. Yang, Z.-K. Wang, T. Kang, Q. Wang, S.-H. Turren-Cruz, X.-Y. Gao, C.-S. Hsu, L.-S. Liao, A. Abate, *Adv. Mater.* **2019**, 31, 1901519.

[45]   C. Liu, L. Zhang, X. Zhou, J. Gao, W. Chen, X. Wang, B. Xu, *Adv. Funct. Mater.* **2019**, 0, 1807604.

[46]   C. Wu, D. Wang, Y. Zhang, F. Gu, G. Liu, N. Zhu, W. Luo, D. Han, X. Guo, B. Qu, S. Wang, Z. Bian, Z. Chen, L. Xiao, *Adv. Func. Mater.* 0, 1902974.

[47]   M. H. Kumar, N. Yantara, S. Dharani, M. Graetzel, S. Mhaisalkar, P. P. Boix, N. Mathews, *Chem. Commun.* **2013**, 49, 11089.

[48]   P. Docampo, J. M. Ball, M. Darwich, G. E. Eperon, H. J. Snaith, *Nat. Commun.* **2013**, 4, 2761.

[49]   D. Liu, T. L. Kelly, *Nat. Photonics* **2014**, 8, 133.

[50]   S. S. Shin, W. S. Yang, J. H. Noh, J. H. Suk, N. J. Jeon, J. H. Park, J. S. Kim, W. M. Seong, S. I. Seok, *Nat. Commun.* **2015**, 6, 7410.

[51]   D. Yang, R. Yang, X. Ren, X. Zhu, Z. Yang, C. Li, S. Liu, *Adv. Mater.* **2016**, 28, 5206.

[52]   J. Yoon, H. Sung, G. Lee, W. Cho, N. Ahn, H. S. Jung, M. Choi, *Energy Environ. Sci.* **2017**, 10, 337.

[53]   S. Wang, Y. Jiang, Emilio J. Juarez-Perez, Luis K. Ono, Y. Qi, *Nat. Energy*

2016, 2, 16195.

[54]   G. Niu, X. Guo, L. Wang, *J. Mater. Chem. A* **2015**, 3, 8970.

[55]   N. Aristidou, I. Sanchez-Molina, T. Chotchuangchutchaval, M. Brown, L. Martinez, T. Rath, S. A. Haque, *Angew. Chem. Int. Ed.* **2015**, 54, 8208.

[56]   J. Schneider, M. Matsuoka, M. Takeuchi, J. Zhang, Y. Horiuchi, M. Anpo, D. W. Bahnemann, *Chem. Rev.* **2014**, 114, 9919.

[57]   S. Ito, S. Tanaka, K. Manabe, H. Nishino, *J. Phys. Chem. C* **2014**, 118, 16995.

[58]   S. S. Shin, E. J. Yeom, W. S. Yang, S. Hur, M. G. Kim, J. Im, J. Seo, J. H. Noh, S. I. Seok, *Science* **2017**, 356, 167.

[59]   W. Li, W. Zhang, S. V. Reenen, R. J. Sutton, J. Fan, A. A. Haghighirad, M. B. Johnston, L. Wang, H. J. Snaith, *Energy Environ. Sci.* **2016**, 9, 490.

[60]   Y. Kato, L. K. Ono, M. V. Lee, S. Wang, S. R. Raga, Y. Qi, *Adv. Mater. Interfaces* **2015**, 2, 1500195.

[61]   H. Back, G. Kim, J. Kim, J. Kong, T. K. Kim, H. Kang, H. Kim, J. Lee, S. Lee, K. Lee, *Energy Environ. Sci.* **2016**, 9, 1258.

[62]   J. You, L. Meng, T.-B. Song, T.-F. Guo, Y. Yang, W.-H. Chang, Z. Hong, H. Chen, H. Zhou, Q. Chen, Y. Liu, N. De Marco, Y. Yang, *Nat. Nanotechnol.* **2015**, 11, 75.

[63]   N. Arora, M. I. Dar, A. Hinderhofer, N. Pellet, F. Schreiber, S. M. Zakeeruddin, M. Grätzel, *Science* **2017**, 358, 768.

[64]   E. Jokar, Z. Y. Huang, S. Narra, C. Y. Wang, V. Kattoor, C. C. Chung, E. W. G. Diau, *Adv. Energy Mater.* **2018**, 8, 1701640.

[65]   W. Tress, N. Marinova, T. Moehl, S. M. Zakeeruddin, M. K. Nazeeruddin, M. Gratzel, *Energy Environ. Sci.* **2015**, 8, 995.

[66]   S. Meloni, T. Moehl, W. Tress, M. Franckevičius, M. Saliba, Y. H. Lee, P. Gao, M. K. Nazeeruddin, S. M. Zakeeruddin, U. Rothlisberger, M. Graetzel, *Nat. Commun.* **2016**, 7, 10334.

[67]   Y. Shao, Z. Xiao, C. Bi, Y. Yuan, J. Huang, *Nat. Commun.* **2014**, 5, 5784.

[68]   R. Wang, J. Wang, S. Tan, Y. Duan, Z.-K. Wang, Y. Yang, *Trends in Chem.* **2019**, 1, 368.

[69]   E. Jokar, C.-H. Chien, C.-M. Tsai, A. Fathi, E. W.-G. Diau, *Adv. Mater.* **2019**, 31, 1804835.

[70]   F. Wang, X. Jiang, H. Chen, Y. Shang, H. Liu, J. Wei, W. Zhou, H. He, W. Liu, Z. Ning, *Joule* **2018**, 2, 2732.

[71]   Q. Tai, X. Guo, G. Tang, P. You, T.-W. Ng, D. Shen, J. Cao, C.-K. Liu, N. Wang, Y. Zhu, C.-S. Lee, F. Yan, *Angew. Chem. Int. Ed.* **2019**, 58, 806.

[72]   J. Lee, M. Malekshahi Byranvand, G. Kang, S. Y. Son, S. Song, G.-W. Kim, T. Park, *J. Am. Chem. Soc.* **2017**, 139, 12175.

[73]   S. D. Stranks, H. J. Snaith, *Nat. Nanotechnol.* **2015**, 10, 391.

[74]   M. A. Green, A. Ho-Baillie, H. J. Snaith, *Nat. Photonics* **2014**, 8, 506.

[75]   Y. X. Zhao, K. Zhu, *Chem. Soc. Rev.* **2016**, 45, 655.

[76]   N.-G. Park, M. Grätzel, T. Miyasaka, K. Zhu, K. Emery, *Nat. Energy* **2016**, 1, 16152.

[77]   A. Kojima, K. Teshima, Y. Shirai, T. Miyasaka, *J. Am. Chem. Soc.* **2009**, 131, 6050.

[78]   H. S. Kim, C. R. Lee, J. H. Im, K. B. Lee, T. Moehl, A. Marchioro, S. J. Moon, R. Humphry-Baker, J. H. Yum, J. E. Moser, M. Gratzel, N. G. Park, *Sci Rep-Uk* **2012**, 2.

[79]   W. S. Yang, B.-W. Park, E. H. Jung, N. J. Jeon, Y. C. Kim, D. U. Lee, S. S. Shin, J. Seo, E. K. Kim, J. H. Noh, S. I. Seok, *Science* **2017**, 356, 1376.

[80]   L. Meng, J. You, T.-F. Guo, Y. Yang, *Acc. Chem. Res.* **2016**, 49, 155.

[81]   W. S. Yang, J. H. Noh, N. J. Jeon, Y. C. Kim, S. Ryu, J. Seo, S. I. Seok, *Science* **2015**, 348, 1234.

[82]   D. Bi, C. Yi, J. Luo, J.-D. Décoppet, F. Zhang, Shaik M. Zakeeruddin, X. Li, A. Hagfeldt, M. Grätzel, *Nat. Energy* **2016**, 1, 16142.

[83]   D.-Y. Son, J.-W. Lee, Y. J. Choi, I.-H. Jang, S. Lee, P. J. Yoo, H. Shin, N. Ahn, M. Choi, D. Kim, N.-G. Park, *Nat. Energy* **2016**, 1, 16081.

[84]   H. Tan, A. Jain, O. Voznyy, X. Lan, F. P. García de Arquer, J. Z. Fan, R. Quintero-Bermudez, M. Yuan, B. Zhang, Y. Zhao, F. Fan, P. Li, L. N. Quan, Y. Zhao, Z.-H. Lu, Z. Yang, S. Hoogland, E. H. Sargent, *Science* **2017**, 355, 722.

[85]   W. J. Ke, C. X. Xiao, C. L. Wang, B. Saparov, H. S. Duan, D. W. Zhao, Z. W. Xiao, P. Schulz, S. P. Harvey, W. Q. Liao, W. W. Meng, Y. Yu, A. J. Cimaroli, C. S. Jiang, K. Zhu, M. Al-Jassim, G. J. Fang, D. B. Mitzi, Y. F. Yan, *Adv. Mater.* **2016**, 28, 5214.

[86]   H. Zhou, Q. Chen, G. Li, S. Luo, T.-b. Song, H.-S. Duan, Z. Hong, J. You, Y. Liu, Y. Yang, *Science* **2014**, 345, 542.

[87]   Q. Jiang, L. Zhang, H. Wang, X. Yang, J. Meng, H. Liu, Z. Yin, J. Wu, X. Zhang, J. You, **2016**, 2, 16177.

[88]   Y. H. Shao, Z. G. Xiao, C. Bi, Y. B. Yuan, J. S. Huang, *Nat. Commun.* **2014**, 5, 5784.

[89]   J. Xu, A. Buin, A. H. Ip, W. Li, O. Voznyy, R. Comin, M. Yuan, S. Jeon, Z. Ning, J. J. McDowell, P. Kanjanaboos, J.-P. Sun, X. Lan, L. N. Quan, D. H. Kim, I. G. Hill, P. Maksymovych, E. H. Sargent, *Nat. Commun.* **2015**, 6, 7081.

[90]   L. Li, Y. H. Chen, Z. H. Liu, Q. Chen, X. D. Wang, H. P. Zhou, *Adv. Mater.* **2016**, 28, 9862.

[91]   M. Saliba, T. Matsui, K. Domanski, J. Y. Seo, A. Ummadisingu, S. M. Zakeeruddin, J. P. Correa-Baena, W. R. Tress, A. Abate, A. Hagfeldt, M. Gratzel, *Science* **2016**, 354, 206.

[92]   T. Leijtens, G. E. Eperon, A. J. Barker, G. Grancini, W. Zhang, J. M. Ball, A. R. S. Kandada, H. J. Snaith, A. Petrozza, *Energy Environ. Sci.* **2016**, 9, 3472.

[93]   M. Hadadian, J. P. Correa-Baena, E. K. Goharshadi, A. Ummadisingu, J. Y. Seo, J. S. Luo, S. Gholipour, S. M. Zakeeruddin, M. Saliba, A. Abate, M.

Gratzel, A. Hagfeldt, *Adv. Mater.* **2016**, 28, 8681.

[94]   Q. Wang, B. Chen, Y. Liu, Y. Deng, Y. Bai, Q. Dong, J. Huang, *Energy Environ. Sci.* **2017**, 10, 516.

[95]   N. Ahn, K. Kwak, M. S. Jang, H. Yoon, B. Y. Lee, J.-K. Lee, P. V. Pikhitsa, J. Byun, M. Choi, *Nat. Commun.* **2016**, 7, 13422.

[96]   Z. G. Xiao, Q. F. Dong, C. Bi, Y. C. Shao, Y. B. Yuan, J. S. Huang, *Adv. Mater.* **2014**, 26, 6503.

[97]   W. Y. Nie, H. H. Tsai, R. Asadpour, J. C. Blancon, A. J. Neukirch, G. Gupta, J. J. Crochet, M. Chhowalla, S. Tretiak, M. A. Alam, H. L. Wang, A. D. Mohite, *Science* **2015**, 347, 522.

[98]   X. Li, D. Q. Bi, C. Y. Yi, J. D. Decoppet, J. S. Luo, S. M. Zakeeruddin, A. Hagfeldt, M. Gratzel, *Science* **2016**, 353, 58.

[99]   M. J. Yang, T. Y. Zhang, P. Schulz, Z. Li, G. Li, D. H. Kim, N. J. Guo, J. J. Berry, K. Zhu, Y. X. Zhao, *Nat. Commun.* **2016**, 7, 12305.

[100] J. T. W. Wang, Z. P. Wang, S. Pathak, W. Zhang, D. W. deQuilettes, F. Wisnivesky-Rocca-Rivarola, J. Huang, P. K. Nayak, J. B. Patel, H. A. M. Yusof, Y. Vaynzof, R. Zhu, I. Ramirez, J. Zhang, C. Ducati, C. Grovenor, M. B. Johnston, D. S. Ginger, R. J. Nicholas, H. J. Snaith, *Energy Environ. Sci.* **2016**, 9, 2892.

[101] C. G. Wu, C. H. Chiang, Z. L. Tseng, M. K. Nazeeruddin, A. Hagfeldt, M. Gratzel, *Energy Environ. Sci.* **2015**, 8, 2725.

[102] W. Zhang, M. Saliba, D. T. Moore, S. K. Pathak, M. T. Hörantner, T. Stergiopoulos, S. D. Stranks, G. E. Eperon, J. A. Alexander-Webber, A. Abate, A. Sadhanala, S. Yao, Y. Chen, R. H. Friend, L. A. Estroff, U. Wiesner, H. J. Snaith, *Nat. Commun.* **2015**, 6, 6142.

[103] D. Forgács, M. Sessolo, H. J. Bolink, *J. Mater. Chem. A* **2015**, 3, 14121.

[104] C. Li, Q. Guo, W. Qiao, Q. Chen, S. Ma, X. Pan, F. Wang, J. Yao, C. Zhang, M. Xiao, S. Dai, Z. a. Tan, *Org. Electron.* **2016**, 33, 194.

[105] D. Luo, L. Zhao, J. Wu, Q. Hu, Y. Zhang, Z. Xu, Y. Liu, T. Liu, K. Chen, W. Yang, W. Zhang, R. Zhu, Q. Gong, *Adv. Mater.* **2017**, 29, 1604758.

[106] J. Qing, H.-T. Chandran, Y.-H. Cheng, X.-K. Liu, H.-W. Li, S.-W. Tsang, M.-F. Lo, C.-S. Lee, *ACS Appl. Mater. Interfaces* **2015**, 7, 23110.

[107] W. Qiu, T. Merckx, M. Jaysankar, C. Masse de la Huerta, L. Rakocevic, W. Zhang, U. W. Paetzold, R. Gehlhaar, L. Froyen, J. Poortmans, D. Cheyns, H. J. Snaith, P. Heremans, *Energy Environ. Sci.* **2016**, 9, 484.

[108] Y. Shao, Y. Yuan, J. Huang, *Nat. Energy* **2016**, 1, 15001.

[109] Y. C. Kim, N. J. Jeon, J. H. Noh, W. S. Yang, J. Seo, J. S. Yun, A. Ho-Baillie, S. Huang, M. A. Green, J. Seidel, T. K. Ahn, S. I. Seok, *Adv. Energy Mater.* **2016**, 6, 1502104.

[110] C. Roldán-Carmona, P. Gratia, I. Zimmermann, G. Grancini, P. Gao, M. Graetzel, M. K. Nazeeruddin, *Energy Environ. Science* **2015**, 8, 3550.

[111] F. Hao, C. C. Stoumpos, Z. Liu, R. P. H. Chang, M. G. Kanatzidis, *J. Am. Chem. Soc.* **2014**, 136, 16411.

[112] N. J. Jeon, J. H. Noh, Y. C. Kim, W. S. Yang, S. Ryu, S. I. Seok, *Nat. Mater.* **2014**, 13, 897.

[113] J.-Y. Seo, T. Matsui, J. Luo, J.-P. Correa-Baena, F. Giordano, M. Saliba, K. Schenk, A. Ummadisingu, K. Domanski, M. Hadadian, A. Hagfeldt, S. M. Zakeeruddin, U. Steiner, M. Grätzel, A. Abate, *Adv. Energy Mater.* **2016**, 6, 1600767.

[114] Z. Huang, X. Hu, C. Liu, L. Tan, Y. Chen, *Adv. Funct. Mater.* **2017**, 27, 1703061.

[115] A. R. Pascoe, Q. Gu, M. U. Rothmann, W. Li, Y. Zhang, A. D. Scully, X. Lin, L. Spiccia, U. Bach, Y.-B. Cheng, *Sci. China Mater.* **2017**, 60, 617.

[116] J. H. Heo, D. H. Song, S. H. Im, *Adv. Mater.* **2014**, 26, 8179.

[117] X. Li, M. Ibrahim Dar, C. Yi, J. Luo, M. Tschumi, S. M. Zakeeruddin, M. K. Nazeeruddin, H. Han, M. Grätzel, *Nat. Chem.* **2015**, 7, 703.

[118] Y. Zhao, J. Wei, H. Li, Y. Yan, W. Zhou, D. Yu, Q. Zhao, *Nat. Commun.* **2016**, 7, 10228.

[119] S. Jarmelo, I. Reva, P. R. Carey, R. Fausto, *Vibrational Spectroscopy* **2007**, 43, 395.

[120] Y. Bai, Q. Dong, Y. Shao, Y. Deng, Q. Wang, L. Shen, D. Wang, W. Wei, J. Huang, *Nat. Commun.* **2016**, 7, 12806.

[121] Z. Zhou, Z. Wang, Y. Zhou, S. Pang, D. Wang, H. Xu, Z. Liu, N. P. Padture, G. Cui, *Angew. Che. Int. Ed.* **2015**, 54, 9705.

[122] Q. Chen, H. Zhou, T.-B. Song, S. Luo, Z. Hong, H.-S. Duan, L. Dou, Y. Liu, Y. Yang, *Nano Lett.* **2014**, 14, 4158.

[123] Q. Han, S.-H. Bae, P. Sun, Y.-T. Hsieh, Y. Yang, Y. S. Rim, H. Zhao, Q. Chen, W. Shi, G. Li, Y. Yang, *Adv. Mater.* **2016**, 28, 2253.

[124] M. Samiee, S. Konduri, B. Ganapathy, R. Kottokkaran, H. A. Abbas, A. Kitahara, P. Joshi, L. Zhang, M. Noack, V. Dalal, *Appl. Phys. Lett.* **2014**, 105, 153502.

[125] A. Guerrero, G. Garcia-Belmonte, I. Mora-Sero, J. Bisquert, Y. S. Kang, T. J. Jacobsson, J.-P. Correa-Baena, A. Hagfeldt, *J. Phys. Chem. C* **2016**, 120, 8023.

[126] A. Kojima, K. Teshima, Y. Shirai, T. Miyasaka, *J. Am. Chem. Soc.* **2009**, 131, 6050.

[127] P. You, Z. K. Liu, Q. D. Tai, S. H. Liu, F. Yan, *Adv. Mater.* **2015**, 27, 3632.

[128] Z. K. Liu, P. You, C. Xie, G. Q. Tang, F. Yan, *Nano Energy* **2016**, 28, 151.

[129] Q. Tai, F. Yan, *Adv. Mater.* **2017**, 29, 1700192.

[130] Q. Tai, P. You, H. Sang, Z. Liu, C. Hu, H. L. W. Chan, F. Yan, *Nat. Commun.* **2016**, 7, 11105.

[131] Y.-H. Kim, H. Cho, J. H. Heo, T.-S. Kim, N. Myoung, C.-L. Lee, S. H. Im, T.-W. Lee, *Adv.Mater.* **2015**, 27, 1248.

[132] N. Wang, L. Cheng, R. Ge, S. Zhang, Y. Miao, W. Zou, C. Yi, Y. Sun, Y. Cao,

R. Yang, Y. Wei, Q. Guo, Y. Ke, M. Yu, Y. Jin, Y. Liu, Q. Ding, D. Di, L. Yang, G. Xing, H. Tian, C. Jin, F. Gao, R. H. Friend, J. Wang, W. Huang, *Nat. Photonics* **2016**, 10, 699.

[133] S. W. Eaton, M. Lai, N. A. Gibson, A. B. Wong, L. Dou, J. Ma, L.-W. Wang, S. R. Leone, P. Yang, *Proc. Nati. Acad. Sci.* **2016**, 113, 1993.

[134] S. A. Veldhuis, P. P. Boix, N. Yantara, M. Li, T. C. Sum, N. Mathews, S. G. Mhaisalkar, *Adv. Mate.* **2016**, 28, 6804.

[135] Chao Xie, Peng You, Zhike Liu, Li Li and Feng Yan, *Light Sci. Appl.* **2017**, 6, e17023.

[136] Y. Wang, R. Fullon, M. Acerce, C. E. Petoukhoff, J. Yang, C. Chen, S. Du, S. K. Lai, S. P. Lau, D. Voiry, D. O'Carroll, G. Gupta, A. D. Mohite, S. Zhang, H. Zhou, M. Chhowalla, *Adv. Mater.* **2017**, 29, 1603995.

[137] D.-H. Kang, S. R. Pae, J. Shim, G. Yoo, J. Jeon, J. W. Leem, J. S. Yu, S. Lee, B. Shin, J.-H. Park, *Adv. Mater.* **2016**, 28, 7799.

[138] C. Ma, Y. Shi, W. Hu, M.-H. Chiu, Z. Liu, A. Bera, F. Li, H. Wang, L.-J. Li, T. Wu, *Adv. Mater.* **2016**, 28, 3683.

[139] J. Lu, A. Carvalho, H. Liu, S. X. Lim, A. H. Castro Neto, C. H. Sow, *Angew. Chem. Int. Ed.* **2016**, 55, 11945.

[140] S. Y. Leblebici, L. Leppert, Y. Li, S. E. Reyes-Lillo, S. Wickenburg, E. Wong, J. Lee, M. Melli, D. Ziegler, D. K. Angell, D. F. Ogletree, Paul D. Ashby, F. M. Toma, J. B. Neaton, I. D. Sharp, A. Weber-Bargioni, *Nat. Energy* **2016**, 1, 16093.

[141] W. Kim, M. S. Jung, S. Lee, Y. J. Choi, J. K. Kim, S. U. Chai, W. Kim, D.-G. Choi, H. Ahn, J. H. Cho, D. Choi, H. Shin, D. Kim, J. H. Park, *Adv. Energy Mater.* **2018**, 8, 1702369.

[142] J. Yin, D. Cortecchia, A. Krishna, S. Chen, N. Mathews, A. C. Grimsdale, C. Soci, *J. Phys. Chem. Lett.* **2015**, 6, 1396.

[143] N. Ahn, D.-Y. Son, I.-H. Jang, S. M. Kang, M. Choi, N.-G. Park, *J. Am.*

Chem. Soc. **2015**, 137, 8696.

[144] W. Li, J. Fan, Y. Mai, L. Wang, *Adv. Energy Mater.* **2017**, 7, 1601433.

[145] Z. Ning, X. Gong, R. Comin, G. Walters, F. Fan, O. Voznyy, E. Yassitepe, A. Buin, S. Hoogland, E. H. Sargent, *Nature* **2015**, 523, 324.

[146] G. Tang, P. You, Q. Tai, R. Wu, F. Yan, *Sol. RRL* **2018**, 2, 1800066.

[147] C. Bi, Q. Wang, Y. Shao, Y. Yuan, Z. Xiao, J. Huang, *Nat. Commun.* **2015**, 6, 7747.

[148] K. Wojciechowski, S. D. Stranks, A. Abate, G. Sadoughi, A. Sadhanala, N. Kopidakis, G. Rumbles, C.-Z. Li, R. H. Friend, A. K. Y. Jen, H. J. Snaith, *ACS Nano* **2014**, 8, 12701.

[149] Y. Gong, J. Lin, X. Wang, G. Shi, S. Lei, Z. Lin, X. Zou, G. Ye, R. Vajtai, B. I. Yakobson, H. Terrones, M. Terrones, Beng K. Tay, J. Lou, S. T. Pantelides, Z. Liu, W. Zhou, P. M. Ajayan, *Nat. Mater.* **2014**, 13, 1135.

[150] X. Duan, C. Wang, J. C. Shaw, R. Cheng, Y. Chen, H. Li, X. Wu, Y. Tang, Q. Zhang, A. Pan, J. Jiang, R. Yu, Y. Huang, X. Duan, *Nat. Nanotechnol.* **2014**, 9, 1024.

[151] Z. Liu, S. P. Lau, F. Yan, *Chem. Soc. Rev.* **2015**, 44, 5638.

[152] A. K. Geim, I. V. Grigorieva, *Nature* **2013**, 499, 419.

[153] H. Zhang, *ACS Nano* **2015**, 9, 9451.

[154] Y. Shi, W. Zhou, A.-Y. Lu, W. Fang, Y.-H. Lee, A. L. Hsu, S. M. Kim, K. K. Kim, H. Y. Yang, L.-J. Li, J.-C. Idrobo, J. Kong, *Nano Lett.* **2012**, 12, 2784.

[155] Z. Lin, A. Yin, J. Mao, Y. Xia, N. Kempf, Q. He, Y. Wang, C.-Y. Chen, Y. Zhang, V. Ozolins, Z. Ren, Y. Huang, X. Duan, *Sci. Adv.* **2016**, 2, e1600993.

[156] X. Gao, Y. Zhu, D. Yi, J. Zhou, S. Zhang, C. Yin, F. Ding, S. Zhang, X. Yi, J. Wang, L. Tong, Y. Han, Z. Liu, J. Zhang, *Sci. Adv.* **2018**, 4, eaat6378.

[157] S. Kim, A. Konar, W.-S. Hwang, J. H. Lee, J. Lee, J. Yang, C. Jung, H. Kim, J.-B. Yoo, J.-Y. Choi, Y. W. Jin, S. Y. Lee, D. Jena, W. Choi, K. Kim, *Nat. Commun.* **2012**, 3, 1011.

[158] X. Zou, J. Wang, C.-H. Chiu, Y. Wu, X. Xiao, C. Jiang, W.-W. Wu, L. Mai, T. Chen, J. Li, J. C. Ho, L. Liao, *Adv. Mater.* **2014**, 26, 6255.

[159] M.-L. Tsai, S.-H. Su, J.-K. Chang, D.-S. Tsai, C.-H. Chen, C.-I. Wu, L.-J. Li, L.-J. Chen, J.-H. He, *ACS Nano* **2014**, 8, 8317.

[160] C. Tan, H. Zhang, *J. Am. Chem. Soc.* **2015**, 137, 12162.

[161] J. N. Coleman, M. Lotya, A. O'Neill, S. D. Bergin, P. J. King, U. Khan, K. Young, A. Gaucher, S. De, R. J. Smith, I. V. Shvets, S. K. Arora, G. Stanton, H.-Y. Kim, K. Lee, G. T. Kim, G. S. Duesberg, T. Hallam, J. J. Boland, J. J. Wang, J. F. Donegan, J. C. Grunlan, G. Moriarty, A. Shmeliov, R. J. Nicholls, J. M. Perkins, E. M. Grieveson, K. Theuwissen, D. W. McComb, P. D. Nellist, V. Nicolosi, *Science* **2011**, 331, 568.

[162] S. Lin, S. Liu, Z. Yang, Y. Li, T. W. Ng, Z. Xu, Q. Bao, J. Hao, C.-S. Lee, C. Surya, F. Yan, S. P. Lau, *Adv. Funct. Mater.* **2016**, 26, 864.

[163] S. Liu, S. Lin, P. You, C. Surya, S. P. Lau, F. Yan, *Angew. Chem. Int. Ed.* **2017**, 56, 13717.

[164] M. M. Mdleleni, T. Hyeon, K. S. Suslick, *J. Am. Chem. Soc.* **1998**, 120, 6189.

[165] Q. Wang, Y. Wen, F. Yao, Y. Huang, Z. Wang, M. Li, X. Zhan, K. Xu, F. Wang, F. Wang, J. Li, K. Liu, C. Jiang, F. Liu, J. He, *Small* **2015**, 11, 5388.

[166] M. Sytnyk, S. Yakunin, W. Schöfberger, R. T. Lechner, M. Burian, L. Ludescher, N. A. Killilea, A. YousefiAmin, D. Kriegner, J. Stangl, H. Groiss, W. Heiss, *ACS Nano* **2017**, 11, 1246.

[167] Y. Wang, Z. Chen, F. Deschler, X. Sun, T.-M. Lu, E. A. Wertz, J.-M. Hu, J. Shi, *ACS Nano* **2017**, 11, 3355.

[168] R. H. Bube, *J.Appl.Phys.* **1962**, 33, 1733.

[169] Z. Liu, J. Hu, H. Jiao, L. Li, G. Zheng, Y. Chen, Y. Huang, Q. Zhang, C. Shen, Q. Chen, H. Zhou, *Adv. Mater.* **2017**, 29, 1606774.

[170] D. Yang, X. Zhou, R. Yang, Z. Yang, W. Yu, X. Wang, C. Li, S. Liu, R. P. H. Chang, *Energy Environ. Sci.* **2016**, 9, 3071.

[171] P.-W. Liang, C.-Y. Liao, C.-C. Chueh, F. Zuo, S. T. Williams, X.-K. Xin, J. Lin, A. K.-Y. Jen, *Adv. Mater.* **2014**, 26, 3748.

[172] C.-H. Chiang, C.-G. Wu, *ACS Nano* **2018**, 12, 10355.

[173] S. Yue, K. Liu, R. Xu, M. Li, M. Azam, K. Ren, J. Liu, Y. Sun, Z. Wang, D. Cao, X. Yan, S. Qu, Y. Lei, Z. Wang, *Energy Environ. Sci.* **2017**, 10, 2570.

[174] X. Xiao, C. Bao, Y. Fang, J. Dai, B. R. Ecker, C. Wang, Y. Lin, S. Tang, Y. Liu, Y. Deng, X. Zheng, Y. Gao, X. C. Zeng, J. Huang, *Adv. Mater.* **2018**, 30, 1705176.

[175] H.-L. Hsu, H.-T. Hsiao, T.-Y. Juang, B.-H. Jiang, S.-C. Chen, R.-J. Jeng, C.-P. Chen, *Adv. Energy Mater.* 0, 1802323.

[176] F. Zhang, J. He, Y. Xiang, K. Zheng, B. Xue, S. Ye, X. Peng, Y. Hao, J. Lian, P. Zeng, J. Qu, J. Song, *Adv. Mater.* **2018**, 30, 1803244.

[177] C.-H. Chiang, M. K. Nazeeruddin, M. Grätzel, C.-G. Wu, *Energy Environ. Sci.* **2017**, 10, 808.

[178] K. George, P. Ioannis, P. Barbara, G. Amanda, P. Michael, M. Temur, N. Leyla, D. R. C. A. Esaú, K. George, S. Emmanuel, B. Francesco, K. Emmanuel, *Adv. Energy Mater.* **2018**, 8, 1702287.

[179] A. Guerrero, J. You, C. Aranda, Y. S. Kang, G. Garcia-Belmonte, H. Zhou, J. Bisquert, Y. Yang, *ACS Nano.* **2016**, 10, 218.

[180] I. Zarazua, G. Han, P. P. Boix, S. Mhaisalkar, F. Fabregat-Santiago, I. Mora-Seró, J. Bisquert, G. Garcia-Belmonte, *J. Phys. Chem. Lett.* **2016**, 7, 5105.

[181] J. Huang, Y. Yuan, Y. Shao, Y. Yan, *Nat. Rev. Mater.* **2017**, 2, 17042.

[182] L. Zuo, Z. Gu, T. Ye, W. Fu, G. Wu, H. Li, H. Chen, *J. Am. Chem. Soc.* **2015**, 137, 2674.

[183] Z. Li, T. R. Klein, D. H. Kim, M. Yang, J. J. Berry, M. F. A. M. van Hest, K. Zhu, *Nat. Rev. Mater.* **2018**, 3, 18017.

[184] F. Di Giacomo, A. Fakharuddin, R. Jose, T. M. Brown, *Energy Environ. Sci.*

2016, 9, 3007.

[185]   M. Kaltenbrnner, G. Adam, E. D. Glowacki, M. Drack, R. Schwodiauer, L. Leonat, D. H. Apaydin, H. Groiss, M. C. Scharber, *Nat. Mater.* **2015**, 14, 1032.

[186]   A. Banerjee, F. S. Liu, D. Beglau, T. Su, G. Pietka, J. Yang, S. Guha, *IEEE J. Photovolt.* **2012**, 2, 104.

[187]   A. Banerjee, T. Su, D. Beglau, G. Pietka, F. S. Liu, S. Almutawalli, J. Yang, S. Guha, *IEEE J. Photovolt.* **2012**, 2, 99.

[188]   M. M. Tavakoli, Q. Lin, S.-F. Leung, G. C. Lui, H. Lu, L. Li, B. Xiang, Z. Fan, *Nanoscale* **2016**, 8, 4276.

[189]   A. M. Popov, I. V. Lebedeva, A. A. Knizhnik, Y. E. Lozovik, B. V. Potapkin, *Phys.Rev. B* **2011**, 84, 045404.

[190]   J. Cumings, A. Zettl, *Science* **2000**, 289, 602.

[191]   C. Androulidakis, K. Zhang, M. Robertson, S. Tawfick, *2D Mater.* **2018**, 5, 032005.

[192]   Q. Zheng, B. Jiang, S. Liu, Y. Weng, L. Lu, Q. Xue, J. Zhu, Q. Jiang, S. Wang, L. Peng, *Phys. Rev. Lett.* **2008**, 100, 067205.

[193]   X. Wei, Z. Meng, L. Ruiz, W. Xia, C. Lee, J. W. Kysar, J. C. Hone, S. Keten, H. D. Espinosa, *ACS Nano* **2016**, 10, 1820.

[194]   X. Feng, S. Kwon, J. Y. Park, M. Salmeron, *ACS Nano* **2013**, 7, 1718.

[195]   H. Tsai, W. Nie, J. C. Blancon, C. C. Stoumpos, R. Asadpour, B. Harutyunyan, A. J. Neukirch, R. Verduzco, J. J. Crochet, S. Tretiak, L. Pedesseau, J. Even, M. A. Alam, G. Gupta, J. Lou, P. M. Ajayan, M. J. Bedzyk, M. G. Kanatzidis, A. D. Mohite, *Nature* **2016**, DOI: 10.1038/nature18306.

[196]   J. Wang, R. Su, J. Xing, D. Bao, C. Diederichs, S. Liu, T. C. H. Liew, Z. Chen, Q. Xiong, *ACS Nano* **2018**, 12, 8382.

[197]   R. Rafael, C.-G. Andrés, C. Emmanuele, G. Francisco, *J. Phys. Condensed*

Matter. **2015**, 27, 313201.

[198] L. T. Dou, A. B. Wong, Y. Yu, M. L. Lai, N. Kornienko, S. W. Eaton, A. Fu, C. G. Bischak, J. Ma, T. N. Ding, N. S. Ginsberg, L. W. Wang, A. P. Alivisatos, P. D. Yang, *Science* **2015**, 349, 1518.

[199] J.-W. Lee, Z. Dai, T.-H. Han, C. Choi, S.-Y. Chang, S.-J. Lee, N. De Marco, H. Zhao, P. Sun, Y. Huang, Y. Yang, *Nat. Commun.* **2018**, 9, 3021.

[200] T. C. Shyu, P. F. Damasceno, P. M. Dodd, A. Lamoureux, L. Xu, M. Shlian, M. Shtein, S. C. Glotzer, N. A. Kotov, *Nat. Mater.* **2015**, 14, 785.

[201] J. Feng, *APL Mater.* **2014**, 2, 081801.

[202] L. Wang, P. Liu, P. Guan, M. Yang, J. Sun, Y. Cheng, A. Hirata, Z. Zhang, E. Ma, M. Chen, X. Han, *Nat. Commun.* **2013**, 4, 2413.

[203] K. Zheng, C. Wang, Y.-Q. Cheng, Y. Yue, X. Han, Z. Zhang, Z. Shan, S. X. Mao, M. Ye, Y. Yin, E. Ma, *Nat. Commun.* **2010**, 1, 24.

[204] Q. Dong, Y. Fang, Y. Shao, P. Mulligan, J. Qiu, L. Cao, J. Huang, *Science* **2015**, 347, 967-970.